Hybrid Computational Algorithms for the Problem of Scattering from Grating Structures

by

Babak Alavikia

A thesis
presented to the University of Waterloo
in fulfillment of the
thesis requirement for the degree of
Doctor of Philosophy
in
Electrical and Computer Engineering

Waterloo, Ontario, Canada, 2011

Abstract

Modeling of wave scattering from grating couplers has become increasingly important due to extensive recent research interest in the problem of plasmonic resonance. Computational algorithms which are specially used to model the problem of scattering from the grating surfaces suffer from several drawbacks such as accuracy, computational efficiency, and generality. To address the challenges of the previous methods, this work presents a novel hybrid Finite Element-Boundary Integral Method (FE-BIM) solution to the problem of scattering from grating surfaces consisting of finite or infinite array of two-dimensional cavities and holes in an infinite metallic walls covered with a stratified dielectric layer.

To solve the scattering problem from finite number of cavities or holes engraved in a perfectly conducting screen (PEC), the solution region is divided into interior regions containing the cavities or holes and the region exterior to them. The finite element formulation is applied inside the interior region to derive a linear system of equations associated with nodal field values. Using two-boundary formulation, the surface integral equation employing free-space Green's function is then applied at *only* the opening of the cavities or holes to truncate the computational domain and to connect the matrix subsystem generated from each cavity or hole.

The hybrid FE-BIM method is extended to solve the scattering problem from an infinite array of cavities or holes in a PEC screen by deriving the quasi-periodic Green's function. In the scattering problem from an infinite array of cavities, the finite element formulation is first used inside a single cavity in the unit-cell. Next, the surface integral equation employing the quasi-periodic Green's function is applied at the opening of *only* a single cavity as a boundary constraint to truncate the computational domain. Effect of the infinite array of cavities is incorporated into the system of the nodal equations by the quasi-periodic Green's function.

Finally, the method based on the hybrid FE-BIM is developed to solve the scattering problem from grating surfaces covered with a stratified dielectric layer. In this method, the surface integral equation employing grounded dielectric slab Green's function is applied at the opening of the cavities or holes inside the dielectric coating to truncate the solution region efficiently. An accurate algorithm is presented to derive the grounded dielectric slab Green's function in spatial domain incorporating the effects of the surface-waves and leaky-waves excited and propagated inside the dielectric slab. Numerical examples of near and far field calculations for finite or infinite array of cavities or holes are presented to validate accuracy, versatility, and efficiency of the algorithm presented in this thesis.

Acknowledgements

I would like to express my deepest gratitude to my advisor Professor Omar M. Ramahi. I cannot thank him enough for his thoughtful guidance, generous supports, and friendly discussions which helped me to improve my academic knowledge. I believe that having discussion with him is a peerless privilege.

I am also grateful to my Doctoral committee members, Professor Lilia Krivodonova, Professor Safieddin Safavi-Naeini, and Professor Simarjeet Saini from University of Waterloo, and the External Examiner Professor David Jackson from University of Houston for serving in my examination committee and for their invaluable feedback.

I would like to acknowledge my colleagues, Leila Yuosefi, Mohammed Said Boybay, Ali Kabiri, Hussein Attia, Mohammad Bait Suwailam, Zhao Ren, Na'el Suwan, Mani Kashanianfard, Ali Albishi, Mohammad Alshareef, and Abdulaziz Alqahtani. Their friendly discussion always inspires new ideas.

I would like to thank my dear friend Dr. Eissa Nematollahi for valuable discussions that I had with him about subject of the thesis especially the mathematical insight of this dissertation.

Many thanks to the ECE staff of the University of Waterloo for providing a nice atmosphere, and their kind treatment and support.

I would like to extend my thanks to my friends Dr. Fariborz Rahimi, Rashin Salehi, and their lovely angel Deniz. Their friendship gave color to the time I spent in Waterloo.

Finally, I would like to express my deepest appreciation to my dear mother Shamsossadat, my dear father Alinaghi, my dear brother Siamak, and my dear sister Faranak for their faithful love and support. I would always be indebted to them.

This work was financially supported in part by Research in Motion (RIM), Inc., and the Natural Sciences and Engineering Research Council of Canada (NSERC) under the RIM-NSERC Industrial Research Associate Chair Program.

Dedication

To my parents for their unconditional love and support,
To my beloved wife Behnaz who gave color to my life.

Contents

List of Figures

Chapter 1

Introduction

1.1 Scattering from Grating Surfaces

Modeling of wave scattering from grating surfaces has become increasingly important due to extensive research interests in the problem of plasmonic resonance [1] and phenomenon of extraordinary transmission of light through sub-wavelength apertures [2–4]. Figure 1.1 depicts a schematic of a two-dimensional grating surface consisting of a finite array of cavities and holes engraved in a perfectly electric conducing (PEC) slab coated with conducting layers. The slab is assumed to be infinite in size. In [2–4], it was shown that extra-ordinary transmission of light, a plasmonics phenomenon that has gained significant prominence over the past decade, can be realized when gratings surrounding a sub-wavelength aperture are covered with silver or gold. The interesting feature of such noble metals is that over the optical frequency regime, the metals exhibit negative permittivity. Therefore, modeling of scattering from such grating structures will be inaccurate if the grating material was assumed perfectly conducting. To accurately model the plasmonic resonance based phenomenon, including extra-ordinary transmission of light, the gratings must be covered with a conducting coating. An accurate calculation of near and far fields scattered from the grating surfaces allows manipulation and localization of light in novel applications such as near-field microscopy [5–8], sub-wavelength lithography [9–12], developing tunable optical filters [13] and improving the efficiency of solar cell devices [14–16].

The problem of scattering from a two-dimensional single cavity or hole in a perfect electric conductor is solved by decomposing the fields inside of the cavity or hole from outside by closing the apertures with a PEC surface and introducing equivalent magnetic current over the openings. Fields on the apertures are obtained by forcing the continuity condition on the tangential components of the fields. An appropriate Green's function is required to express the fields due to equivalent magnetic current inside and outside the cav-

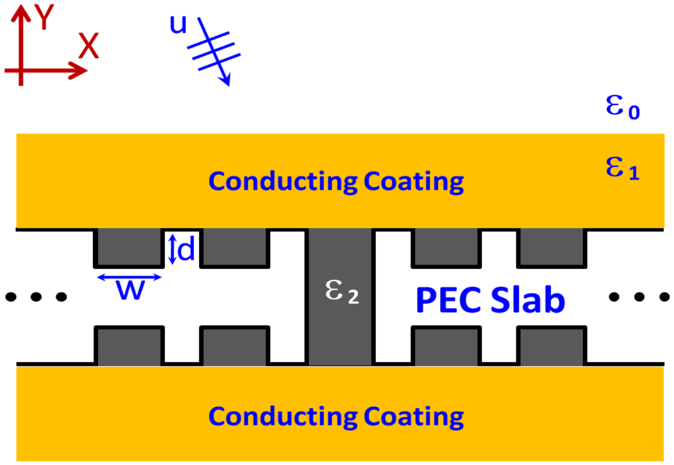

Figure 1.1: Schematic of a grating surface consisting of a finite array of cavities and holes covered with a conducting coating and engraved in an infinite-sized PEC screen.

ity or hole. The equivalent magnetic current can be found using the Method of Moments (MoM) [17, 18] or approximated by the Standard Impedance Boundary Condition (SIBC) or Generalized Impedance Boundary Condition (GIBC) [19, 20]. Although using MoM is a powerful method to calculate the magnetic current on the apertures, deriving Green's function inside the cavity limits this method to canonical shapes and only homogenous and isotropic cavity fillings. On the other hand, SIBC and GIBC are suitable for simulating infinite planar dielectric coatings and have limitation when encountering material discontinuities and cavity edges. Therefore, SIBC and GIBC are not applicable for the multiple cavity structures.

Methods based on Integral Equations (IE) are also used to solve the problem of scattering from cavities. Although these methods are applicable to general-shape cavities, their applications to cavities with infinite conducting walls involves geometry-specific approximations. Another problem arising with the IE-based methods is the resultant dense system matrix which is computationally expensive to solve. To overcome these deficiencies, hybrid methods based on the Physical Optics and Method of Moments (PO-MoM) were introduced [21]. In the PO-MoM method, the induced current, which is the solution of the PO method for the unperturbed conductor sheet, is corrected with the MoM solution.

One of the efficient methods to solve the scattering problem from PEC gratings is the modal-based method. Extensive studies based on the Mode Matching Technique (MMT) have been reported in the literature [22–31]. Typically, for a single rectangular cavity engraved in a PEC surface, the fields inside the cavity are expressed in terms of a Fourier series of the parallel-plate waveguide modes. In the space exterior to the cavity, the scattered field is expressed in Fourier terms. Matching the modes inside and outside of the cavity at the aperture determines the unknown modes' coefficients. The mode matching method is efficiently applicable to multiple cavities with arbitrary shape and spacing but it cannot be used when encountering cavities having inhomogeneous or anisotropic fillings.

Methods based on differential equations such as the Finite Element Method (FEM) and the Finite-Difference Time-Domain method (FDTD) are suitable for the problem of scattering from general-shape cavities or holes with complex fillings. In the FEM, the variational equation related to the weak form of Helmholtz's equation is discretized. The attractive feature of the finite methods is the generation of highly sparse and banded matrices which can be solved efficiently using special algorithms. In the case of scatterers with finite geometry, the unbounded region around the target is truncated using an Absorbing Boundary Condition (ABC) or Perfectly Matched Layers (PML). In the case of infinite scatterers such as a cavity or hole within an infinite ground plane, it is impossible to fully enclose the scatterer's geometry. Therefore, the behavior of the scattered field due to the infinite PEC wall outside of the computational domain boundary cannot be modeled properly. In other words, a portion of the scattered field from the PEC wall outside of solution domain which propagates into the solution region is ignored and therefore, an error is introduced to the solution. To minimize these errors, the domain truncating boundaries should be far enough from the cavity or hole to enclose a larger segment of the PEC wall in addition to the cavity or hole. However, placing the boundary of the computational domain far from the cavity leads to prohibitive increase in the computational cost, in addition to inaccuracy in the solution due to the exclusion of a large part of the scatterer.

To address the shortcomings of the generic type of FEM solutions incorporating ABCs or PMLs, the hybrid Finite Element-Boundary Integral Method (FE-BIM) using a free-space Green's function was introduced in [32–35]. In FE-BIM, the mesh region is truncated at the opening of the cavity or hole. The fields at the boundary nodes are connected to the interior nodes via the Surface Integral Equation (SIE) where the domain of integration is the aperture of the cavity or hole [34, 35]. The singularity in Green's function is the major drawback of the FE-BIM while calculating the surface integral equation.

To avoid the singularity in Green's function while using FE-BIM, the two-boundary formulation of the FE-BIM was proposed in [32] to solve quasi-static problems such as static and harmonic field distribution in a parallel-plate capacitor. In the two-boundary formulation, the local sources, inhomogeneities and anisotropies are enclosed by an imaginary contour located inside the solution region and in close vicinity of the truncation contour. The surface integral equation is used to connect the field values on the truncation boundary to the field values on the imaginary boundary as a boundary constraint. In [33], the two-boundary FE-BIM based on the scattered field formulation was used to solve the scattering problem from a single cavity engraved in an infinite PEC screen. The effect of the non-zero scattered field on the infinite PEC screen was taken into account by taking advantage of limited support of Green's function on the PEC walls. Consequently, the infinite integral domain was truncated at the region of Green's function support. The method in [33] is highly efficient in solving the scattering problem from a single cavity but in extending the method to multiple cavities the approximation used in truncating the integral domain deteriorate when the cavities are separated by a distance smaller than the support of Green's function.

One question is: how the two-boundary formulation of the FE-BIM can be extended to finite or infinite array of cavities or holes accurately? And a more important question is: how can the FE-BIM handle the problem of scattering from multiple cavities or holes with dielectric coating?

1.2 Survey of Recent Literature

Several methods were reported in the literature to solve the problem of scattering from cavities and holes. Amongst the earliest works based on the equivalence principle in [17,18], the Method of Moments (MoM) was used to calculate the equivalent magnetic current on the apertures of a hole. The MoM formulation was represented by two n-port generalized networks. These networks were connected by current sources in parallel. In [19], the equivalent magnetic current was determined using the dominant mode of a Green's function expansion in the rectangular cavity. In [20], using the same method as in [19], the analytical expression for a narrow rectangular cavity was derived.

Amongst the works based on the mode matching technique in [22], an exact formulation for the problem of scattering from a single rectangular cavity was derived. The fields inside the cavity were expressed as the sum of rectangular waveguide modes. The fields outside the cavity were expressed in terms of a Fourier integral. The cylindrical Bessel function were used to expand the Fourier integral into a convergent series form for the cases of TE and TM polarizations of incident Gaussian waves. In [23] and [24], the parallel plate waveguide modes were used inside the cavity to expand the Fourier integral of scattered field for TE and TM polarizations of the incident wave. In [25], an extension the method in [23] and [24] to a finite number of cavities with identical dimensions and spacing in an infinite PEC screen was presented for the TM case. The problem of scattering from the multiple rectangular cavities with arbitrary shape and spacing was investigated for both the TM and TE polarizations in [26]. The problem of scattering from a single rectangular slit was reported in [27, 28]. The fields inside the slit were expressed in terms of parallel-plate waveguide modes. The fields in upper half-space and lower half-space were expressed in terms of a Fourier integral as in [23]. In [29], an extension to a finite number of slits with identical dimensions and spacing in an infinite PEC screen was presented. Recently, a mode matching technique based on a Fourier representation of the field was applied to solve the problem of scattering from a general-shape cavity [30]. In [30], the stair-case approximation was used to divide the cavity into several rectangular layers. In each layer, the fields were expressed using the parallel-plate waveguide modes. Boundary conditions were applied to match the fields at the interface of the layers. The near and far fields were determined for the case of TM polarization. An extension of the method in [30] to multiple general-shape cavities was presented in [31].

Amongst the finite mathematics-based solution of problem of scattering from a single cavity or hole in an infinite PEC screen, the hybrid FE-BIM using free-space Green's function was introduced in [34, 35]. In these works, the mesh region was truncated at the opening of the cavity or hole. The BIM was applied to derive an explicit form of a boundary condition of the third kind (mixed boundary condition) at the cavity's opening [36]. Using a two-boundary formulation which was initially introduced in [32], the scattering from a single rectangular cavity, was presented in [33]. Using the scattered field formulation, which was introduced in [33], the non-zero scattered field on the PEC wall must be taken into account when computing the surface integral. Since the integral domain was infinite, the method in [33] took advantage of the limited support of Green's function to limit the integration domain.

When solving the problem of scattering from a large periodic array of identical cavities or holes, it is useful to approximate the structure as an infinite array and take advantage of the periodicity of the electromagnetic fields. Several methods were reported in the literature to solve the problem of scattering from an infinite array of cavities or holes engraved in metallic screens.

The problem of diffraction by an infinite periodic conducting grating was investigated using a hybrid Finite Element Method-Method of Moments (FEM-MoM) in [37]. Using the equivalence principle, the fields inside of the cavities or holes were decoupled from the outside region by closing the apertures with a PEC surface and introducing equivalent magnetic currents over the openings. Using Floquet's theorem, the scattered fields outside the cavities or holes are produced by the periodic equivalent magnetic current and the fields inside the single cavity or hole were calculated using FEM. Imposing field continuity as the boundary condition at the aperture of the single cavity or hole resulted in a set of equations describing the unknown equivalent magnetic current. The MoM was employed to determine the unknown magnetic current coefficients.

In [38, 39], a hybrid FEM and Floquet mode expansion of the scattered fields was used to analyze the problem of scattering from periodic structures where the FEM was applied inside the unit-cell which enclosed all inhomogeneities and the periodic boundary condition was applied on the lateral boundaries of the unit-cell. In addition, field continuity was forced on the upper and lower boundaries of the unit-cell. In this method the upper and lower boundaries must be chosen in a homogenous medium (i.e. in an upper half-space above the cavity) to achieve fast convergence, which results in a prohibitive increase of the solution domain.

An infinite array of bottle-shaped cavities was investigated in [26] using the mode matching technique. As mentioned earlier, although the mode matching technique is highly accurate and efficient, it cannot be used for cavities having inhomogeneous or anisotropic fillings.

Recently, the Method of Moments was used to solve the problem of scattering from an infinite array of rectangular cavities in an impedance screen [40]. Image theory was applied to reduce the infinite array to a single cell of one period. Due to the periodicity, the scattered fields were expanded in terms of Floquet series. Also, the fields inside the cavities were expressed in terms of the eigenfunction series of a parallel plate waveguide with impedance walls. By forcing the continuity of the fields at the aperture of the cavity, the integral equation was derived and solved using the Method of Moments. Another method using the Overlapping T-block Method (OTM) and the Floquet theorem was reported in [41]. The array was divided into the infinite T-blocks associated with each cavity. The fields inside each T-block were calculated using Green's function and the mode matching techniques. By superposing the fields in overlapping T-blocks and using the Floquet theorem, the total fields were expressed in closed form. However, this method is limited to cavities with canonical shape and homogenous fillings.

1.3 Objective of this Study

The goals of this study are:

1. **Developing** a new hybrid FE-BIM method to solve the problem of scattering from a single cavity engraved in an infinite perfect electric conducting screen.
2. **Extending** the method in 1 to multiple cavities engraved in a PEC screen.
3. **Extending** the method in 1 to solve the problem of scattering from single and multiple holes engraved in a PEC slab.
4. **Developing** an efficient method to solve the problem of scattering from a conducting surface with an infinitely periodic grating.
5. **Extending** the methods developed in 1 - 4 to solve the problem of scattering from grating surfaces with a dielectric coating.

The organization of this thesis is as follows: In chapter 2, the hybrid FE-BIM formulation of the scattering problem from a single cavity is presented. The boundary integral equation using free-space Green's function for the TM and TE cases is derived, respectively, to truncate the mesh region and modify the matrix equation. Then, the extension of the method to multiple cavities is presented. Several examples are presented and validated using methods published in the literature and available commercial packages where possible.

Chapter 3, presents a systematic study to compare the accuracy of the BIM as a global boundary condition with ABCs and PMLs as a local boundary condition in solving the scattering problem from grating surfaces. In this chapter the fundamental limitations on the use of the local boundary condition to solve the problem of scattering from an infinite structures is discussed.

In chapter 4, the formulation which was introduced in chapter 2 is extended to holes in the conducting screen. A boundary integral equation using a free-space Green's function is derived for both the upper half-space and the lower half-space of the PEC slab to truncate the mesh region at both apertures. The method is extended to multiple holes and holes with side gratings. Several examples are presented and validated using available commercial FEM solvers.

In chapter 5, a new two-boundary FE-BIM formulation employing a quasi-periodic Green's function is developed to solve the problem of scattering from an infinite periodic array of identical cavities engraved in an infinite perfect electric conductor screen. Several examples are provided to validate the method.

Chapter 6 presents a solution, using the hybrid FE-BIM introduced in chapters 2-5, to the problem of scattering from an infinite or finite array of two-dimensional cavities engraved in an infinite PEC flat screen *and* covered with a stratified dielectric coating. A boundary integral formulation employing a grounded dielectric slab Green's function is derived to truncate the solution region at the aperture of the cavities inside the dielectric coating. An accurate algorithm to derive the grounded dielectric slab Green's function in the spatial domain incorporating the effects of the surface waves and leaky waves is presented in this chapter. Several examples are provided and validated using available commercial FEM solvers.

In chapter 7, the formulation which was introduced in chapter 6 is extended to an array of holes with side gratings in a conducting screen and covered with a stratified dielectric coating. The grounded dielectric slab Green's function in the spatial domain is derived for the upper half-space and the lower half-space of the PEC slab. Finally, in chapter 8, future work and directions are provided.

Chapter 2

Scattering from Cavities in Conducting Surfaces

In this chapter, a new finite-element based method to solve the problem of scattering from multiple cavities in infinite metallic structures is developed. The method presented here is an extension of the concept introduced earlier in [33] to multiple cavities using the total field formulation. Using the two-boundary formulation which was initially introduced in [32], the unbounded region in the computational domain is divided into bounded frames containing each cavity plus a thin layer above the openings of the cavities. Each layer is limited to the width of the cavity's aperture (see Fig. 2.1). The finite-element formulation is used to obtain the solution of Helmholtz's equation inside the local frames. The surface integral equation using a half-space Green's function, which was reported in [33], for the TM and TE polarization is derived and applied at the opening of the cavity as a global boundary condition. This boundary constraint determines the behavior of nodes on the local frame boundary in terms of interior nodes. The Neumann or Dirichlet boundary condition is applied on the PEC walls of the cavities in the TE or TM case, respectively.

It is emphasized that, in this method, the formulation is based on the total field rather than the scattered field as in [33]. In the scattered field formulation, the non-zero scattered field on the PEC wall must be taken into account when computing the surface integral. Since the integral domain is infinite, in [33] an approximation was applied that took advantage of the limited support of the Green's function. If the scattered field formulation in [33] is extended to multiple cavities, the approximations used earlier deteriorate when the cavities are separated by distances smaller than the support of the Green's function. In the total field formulation, however, the surface integration is limited to the aperture of the cavities since it is zero on the PEC wall (after choosing the appropriate Green's function). Therefore, the problem of multiple cavities does not pose any particular challenge under the total field formulation.

2.1 Finite-Element Formulation of the Problem

Figure 2.1 shows a 2-D cavity having an arbitrary shape in a perfectly conductor surface and illuminated by an obliquely incident plane wave. The angle θ represents the angle of the incident wave. u^{inc}, u^{ref} and u^{s} represent the incident field, reflected field by the PEC wall, and scattered fields, respectively, along the cavity's axis. Let Γ_B represent the contour at the cavity opening, and Γ_O the top contour in close vicinity of Γ_B such that the region between Γ_B and Γ_O is devoid of field nodes. The choice Γ_O locating one layer above the Γ_B minimizes the number of field unknowns at the truncating boundary. Also let Ω_{in} denote the interior region of the cavity including the layer between Γ_B and Γ_O. Next, the solution domain Ω_{in} is discretized into triangular elements. Notice that, however, rectangular or other types of elements can be used without affecting the theoretical development presented here. The unknown total field u^t over each element is described by set of the interpolating functions given by

$$u^t = \sum_{i=1}^{m} {u_i}^t \alpha_i(x, y) \tag{2.1}$$

where m is number of nodes in each element at which the unknown field is defined, and $\alpha_i(x, y)$ is the interpolation function. In Eq. (2.1), u^t represents E_z for TM$_z$ polarization or H_z for TE$_z$ polarization. The conventional finite element formulation is used inside each element to obtain the weak form of Helmholtz's equation:

$$\boldsymbol{\nabla} \cdot \left(\frac{1}{p(x, y)} \boldsymbol{\nabla} u^t \right) + {k_0}^2 q(x, y) u^t = g. \tag{2.2}$$

In Eq. (2.2), $p(x, y)$ and $q(x, y)$ are defined as $\mu_r(x, y)$ and $\varepsilon_r(x, y)$, respectively, for the TM$_z$ polarization, or $\varepsilon_r(x, y)$ and $\mu_r(x, y)$, respectively, for the TE$_z$ polarization. k_0 is propagation constant of the wave in free space. The time harmonic factor $\exp(j\omega t)$ is assumed and suppressed throughout. By defining the residual, r^e as

$$r^e = \boldsymbol{\nabla} \cdot \left(\frac{1}{p(x, y)} \boldsymbol{\nabla} u^t \right) + k_0^2 q(x, y) u^t - g \tag{2.3}$$

and using the weighting function w_i, the weighted residual integral R_i^e is defined as

$$R_i^e = \int_{\Omega^e} w_i \left(\boldsymbol{\nabla} \cdot \left(\frac{1}{p(x, y)} \boldsymbol{\nabla} u^t \right) + {k_0}^2 q(x, y) u^t - g \right) d\Omega = 0. \tag{2.4}$$

In Eqs. (2.3), and (2.4) the superscript e denotes the element number. Using the Green's first identity, Eq. (2.4) can be rewritten as

$$R_i^e = -\int_{\Omega^e} \left(\frac{1}{p(x, y)} \boldsymbol{\nabla} w_i \cdot \boldsymbol{\nabla} u^t - {k_0}^2 q(x, y) w_i u^t + g w_i \right) d\Omega + \oint_{\Gamma^e} \frac{w_i}{p(x, y)} \boldsymbol{\nabla} u^t \cdot d\boldsymbol{\Gamma} = 0 \tag{2.5}$$

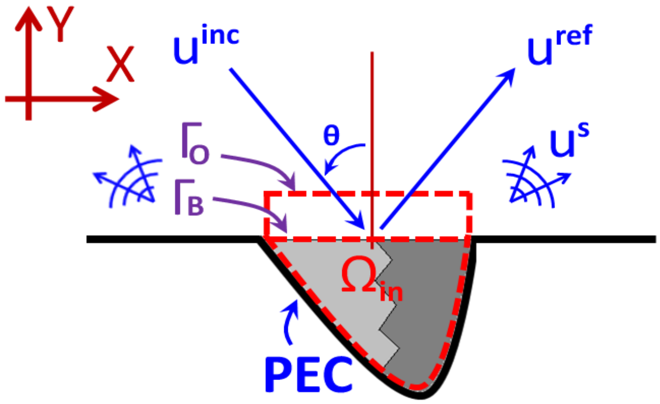

Figure 2.1: Schematic of the scattering problem from a cavity in a PEC surface. The dotted line represents bounded region which contains all sources, inhomogeneities and anisotropies.

where Γ^e is the contour along elements sides enclosing Ω^e. By choosing $w_i = \alpha_i(x, y)$, Galerkin's method, R^e can be expressed in matrix form

$$R^e = \left[M^e\right]\left[u^e\right] - \left[F^e\right] = 0 \tag{2.6}$$

where u^e represents the unknown field value at nodes in the element. The elements of $m \times m$ matrix M^e, and $m \times 1$ matrix F^e are given by

$$\begin{aligned} M^e_{ij} &= \int_{\Omega^e}\left(\frac{1}{p(x,y)}\boldsymbol{\nabla}\alpha_i(x,y)\cdot\boldsymbol{\nabla}\alpha_j(x,y) - {k_0}^2 q(x,y)\alpha_i(x,y)\alpha_j(x,y)\right)d\Omega \\ &\quad + \oint_{\Gamma^e}\frac{\alpha_i(x,y)}{p(x,y)}\boldsymbol{\nabla}\alpha_j(x,y)\cdot d\boldsymbol{\Gamma} \\ F^e_i &= -\int_{\Omega^e} g\alpha_i(x,y)d\Omega, \end{aligned} \tag{2.7}$$

respectively. By assembling all local system matrices Eq. (2.6), the global system matrix can be represented symbolically as

$$\begin{bmatrix} M_{ii} & M_{ib} & 0 \\ M_{bi} & M_{bb} & M_{bo} \\ 0 & M_{ob} & M_{oo} \end{bmatrix}\begin{bmatrix} u_i \\ u_b \\ u_o \end{bmatrix} = \begin{bmatrix} F_i \\ F_b \\ F_o \end{bmatrix} \tag{2.8}$$

where u_i, u_b and u_o represent nodal field values inside the cavity, on Γ_B, and on Γ_O, respectively. The $[F]$ matrix represents impressed sources at each node, therefore, $[F]$ is zero in this problem.

The linear system of equations in Eq. (2.8) represents the relationship between the nodal field values without any external constraint. The imposition of a specific excitation represented by the incident plane wave has to be taken into consideration through a boundary constraint that establishes a relationship between the incident field, the boundary nodes and the interior nodes. In the next section, the surface integral equation will be developed and used as a boundary constraint to express the nodal field values on Γ_O in terms of the nodal field values on Γ_B.

2.2 Surface Integral Equation for $\mathrm{TM_z}$ Polarization

The surface integral equation using the Green's function of first kind will be used to express the nodal field values on Γ_O in terms of the nodal field values on Γ_B. Let us consider the domain Ω_∞ representing the half-space above the PEC (see Fig. 2.2). In Ω_∞ and for the TM_z polarization case, the electric field vector has only a z-component satisfying Helmholtz's equation:

$$\nabla^2 E_z(\boldsymbol{\rho}) + {k_0}^2 E_z(\boldsymbol{\rho}) = j\omega\mu_r J_z(\boldsymbol{\rho}), \qquad \boldsymbol{\rho} \in \Omega_\infty \tag{2.9}$$

where $J_z(\boldsymbol{\rho})$ is an electric current inside Ω_∞. Let us introduce the Green's function $G^e(\boldsymbol{\rho}, \boldsymbol{\rho}')$ which is the solution due to an electric current filament located at $\boldsymbol{\rho}'$ and governed by Helmholtz's equation

$$\nabla^2 G^e(\boldsymbol{\rho}, \boldsymbol{\rho}') + {k_0}^2 G^e(\boldsymbol{\rho}, \boldsymbol{\rho}') = -\delta(\boldsymbol{\rho} - \boldsymbol{\rho}') \qquad \boldsymbol{\rho}, \boldsymbol{\rho}' \in \Omega_\infty. \tag{2.10}$$

$G^e(\boldsymbol{\rho}, \boldsymbol{\rho}')$ satisfies the boundary condition $G^e(\boldsymbol{\rho}, \boldsymbol{\rho}')|_{y=0} = 0$ (i.e., $G^e = 0$ on Γ) and Sommerfeld radiation condition at infinity (for an unbounded region including localized sources, the field behavior at large distances from the sources must meet a physical constraint [42]). $G^e(\boldsymbol{\rho}, \boldsymbol{\rho}')$ is easily found to be the zeroth-order Hankel function of the second kind:

$$G^e(\boldsymbol{\rho}, \boldsymbol{\rho}') = -\frac{j}{4} H_0^{(2)}(k_0 |\boldsymbol{\rho} - {\boldsymbol{\rho}'}_{\mathrm{s}}|) + \frac{j}{4} H_0^{(2)}(k_0 |\boldsymbol{\rho} - {\boldsymbol{\rho}'}_{\mathrm{i}}|) \tag{2.11}$$

where $\boldsymbol{\rho}'_{\mathrm{s}}$, and $\boldsymbol{\rho}'_{\mathrm{i}}$ represent the position of the source current, and its image, respectively. The surface integral equation (Eq. (A.6)) for the TM_z polarization, then can be written as

$$\begin{aligned} E_z(\boldsymbol{\rho}') = &- j\omega\mu_r \int_{\Omega_\infty} J_z(\boldsymbol{\rho}) G^e(\boldsymbol{\rho}, \boldsymbol{\rho}') d\Omega \\ &- \oint_{\Gamma + \Gamma_\infty} \left(E_z(\boldsymbol{\rho}) \frac{\partial G^e(\boldsymbol{\rho}, \boldsymbol{\rho}')}{\partial n} - G^e(\boldsymbol{\rho}, \boldsymbol{\rho}') \frac{\partial E_z(\boldsymbol{\rho}')}{\partial n} \right) d\Gamma. \end{aligned} \tag{2.12}$$

Since both E_z and G^e satisfy Sommerfeld radiation condition at infinity, integration over Γ_∞ (see Fig. 2.2) in the right hand side of Eq. (2.12) vanishes (see Eq. (A.7)). Notice that

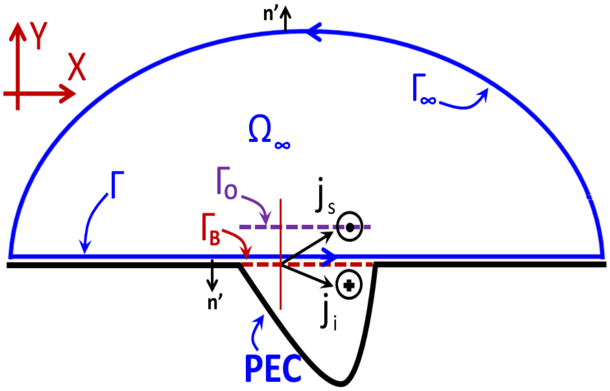

Figure 2.2: Schematic of surface integral contour in the half-space above cavity.

G^e is zero on Γ (see Eq. (2.11)). Additionally, $E_z(\boldsymbol{\rho})$ is zero over the PEC ground plane except on aperture of the cavity. Upon interchanging primed and unprimed coordinates, Eq. (2.12) can be simplified to

$$E_z(\boldsymbol{\rho}) = -j\omega\mu_r \int_{\Omega_\infty} J_z(\boldsymbol{\rho}')G^e(\boldsymbol{\rho},\boldsymbol{\rho}')d\Omega - \int_{\Gamma_B} E_z(\boldsymbol{\rho}')\frac{\partial G^e(\boldsymbol{\rho},\boldsymbol{\rho}')}{\partial n'}d\Gamma. \tag{2.13}$$

In Eq. (2.13), the first term of the right hand side represents the electric field generated by the current filament and its image in the vicinity of the PEC ground plane. These fields can be interpreted as an incident field, and a reflected field from the PEC screen, respectively. The second term in Eq. (2.13) represents the field perturbation due to the cavity . In other words, the total electric field at each point in the upper half-space is the sum of the incident field, reflected field due to the PEC surface and the scattered field due to the aperture of the cavity [36] as

$$E_z(\boldsymbol{\rho}) = E_z^{inc}(\boldsymbol{\rho}) + E_z^{ref}(\boldsymbol{\rho}) - \int_{\Gamma_B} E_z(\boldsymbol{\rho}')\frac{\partial G^e(\boldsymbol{\rho},\boldsymbol{\rho}')}{\partial n'}d\Gamma. \tag{2.14}$$

Referring to Fig. 2.1, let $\boldsymbol{\rho}$ and $\boldsymbol{\rho}'$ be designated the position of nodes on Γ_O and Γ_B, respectively. Therefore the incident and the reflected fields can be written as

$$\begin{aligned} E_z^{inc}(\boldsymbol{\rho}) &= \exp\left(-jk_0(x\sin\theta - y\cos\theta)\right) \\ E_z^{ref}(\boldsymbol{\rho}) &= -\exp\left(-jk_0(x\sin\theta + y\cos\theta)\right) \end{aligned} \tag{2.15}$$

where x and y are Cartesian components of $\boldsymbol{\rho}$. To calculate the last term in Eq. (2.14), the aperture, Γ_B, is discretized into n segments with length of $\Delta x'$. By expanding $E_z(\boldsymbol{\rho}')$ over Γ_B in terms of piecewise linear interpolating functions as

$$E_z(\boldsymbol{\rho}') = \sum_{j=1}^{n} E_{zj}(x_j', y_j') \sum_{k=1}^{2} \psi_{jk}(x_j') \tag{2.16}$$

where x' and y' are Cartesian components of $\boldsymbol{\rho}'$ and

$$\psi_{jk}(x'_j) = \begin{cases} \frac{x'_j}{\Delta x'}, & k{=}1; \\ 1 - \frac{x'_j}{\Delta x'}, & k{=}2. \end{cases} \tag{2.17}$$

Equation (2.14) can be represented in matrix notation as

$$\big[u_o\big] = \big[T\big] + \big[S\big]\,\big[u_b\big] \tag{2.18}$$

where the elements of $[u_o]$, $[u_b]$, and $[T]$ matrices represent $E_z(x,y)$, $E_z(x',y')$, and $\big(E_z^{inc}(x\,,y) + E_z^{ref}(x,y)\big)$, respectively, at each node. The elements of $[S]$ are defined as

$$S_{ij} = \int_{x'_j-\Delta x'}^{x'_j} \psi_{j1}(x'_j)\frac{\partial G^e(x_i,y,x'_j,y')}{\partial y'}dx' + \int_{x'_j}^{x'_j+\Delta x'} \psi_{j2}(x')\frac{\partial G^e(x_i,y,x'_j,y')}{\partial y'}dx' \tag{2.19}$$

where

$$\left.\frac{\partial G_e(x_i,y,x'_j,y')}{\partial y'}\right|_{y'=0} = \frac{-jk_0 y}{2\sqrt{(x_i-x'_j)^2+y^2}}H_1^{(2)}\left(k_0\sqrt{(x_i-x'_j)^2+y^2}\right). \tag{2.20}$$

Equation (2.18) represents the boundary constraint on the cavity opening which is different from [36]. Combining Eq. (2.8) and Eq. (2.18) in matrix form results in the modified system matrix

$$\begin{bmatrix} M_{ii} & M_{ib} \\ M_{bi} & M_{bb}+M_{bo}S \end{bmatrix} \begin{bmatrix} u_i \\ u_b \end{bmatrix} = \begin{bmatrix} F_i \\ F_b - M_{bo}T \end{bmatrix}. \tag{2.21}$$

Equation (2.21) represents the modified system matrix which can be solved using commonly used methods for solving linear systems.

2.3 Surface Integral Equation for $\mathrm{TE_z}$ Polarization

To derive the surface integral equation for the TE_z polarization case, the electric current filament is replaced with a magnetic current filament M_z. In Ω_∞ and for the TE_z polarization case, the magnetic field vector has only a z-component satisfying Helmholtz's equation

$$\nabla^2 H_z(\boldsymbol{\rho}) + {k_0}^2 H_z(\boldsymbol{\rho}) = j\omega\varepsilon_r M_z(\boldsymbol{\rho}), \qquad \boldsymbol{\rho} \in\ \Omega_\infty \tag{2.22}$$

where $\boldsymbol{\rho}$ and Ω_∞ have the same definition as the previous section (see Fig. 2.2). Let us introduce the Green's function of second kind $G^h(\boldsymbol{\rho},\boldsymbol{\rho}')$ which is the solution due to the magnetic current filament located at $\boldsymbol{\rho}'$ and governed by Helmholtz's equation

$$\nabla^2 G^h(\boldsymbol{\rho},\boldsymbol{\rho}') + {k_0}^2 G^h(\boldsymbol{\rho},\boldsymbol{\rho}') = -\delta(\boldsymbol{\rho}-\boldsymbol{\rho}'), \qquad \boldsymbol{\rho},\boldsymbol{\rho}' \in \Omega_\infty. \tag{2.23}$$

Since the image of the magnetic current in the vicinity of the PEC surface is in the same direction of the original current, therefore $G^h(\boldsymbol{\rho}, \boldsymbol{\rho}')|_{y=0} \neq 0$ on the ground plane. In this case, boundary condition on the PEC surface can be written as

$$\left.\frac{\partial G^h(\boldsymbol{\rho}, \boldsymbol{\rho}')}{\partial y'}\right|_{y=0} = 0. \tag{2.24}$$

In addition, $G^h(\boldsymbol{\rho}, \boldsymbol{\rho}')$ satisfies Sommerfeld radiation condition at infinity. Therefore $G^h(\boldsymbol{\rho}, \boldsymbol{\rho}')$ can be represented in terms of the zeroth-order Hankel function of the second kind as

$$G^h(\boldsymbol{\rho}, \boldsymbol{\rho}') = -\frac{j}{4} H_0^{(2)}(k_0|\boldsymbol{\rho} - \boldsymbol{\rho}'_{\mathrm{s}}|) - \frac{j}{4} H_0^{(2)}(k_0|\boldsymbol{\rho} - \boldsymbol{\rho}'_{\mathrm{i}}|). \tag{2.25}$$

The surface integral equation (Eq. (A.6)) for the TE$_z$ polarization, can be expressed as

$$\begin{aligned} H_z(\boldsymbol{\rho}') = & - j\omega\varepsilon_r \int_{\Omega_\infty} M_z(\boldsymbol{\rho}) G^h(\boldsymbol{\rho}, \boldsymbol{\rho}') d\Omega \\ & - \oint_{\Gamma+\Gamma_\infty} \left(H_z(\boldsymbol{\rho}) \frac{\partial G^h(\boldsymbol{\rho}, \boldsymbol{\rho}')}{\partial n} - G^h(\boldsymbol{\rho}, \boldsymbol{\rho}') \frac{\partial H_z(\boldsymbol{\rho})}{\partial n} \right) d\Gamma. \end{aligned} \tag{2.26}$$

Both $H_z(\boldsymbol{\rho})$ and $G^h(\boldsymbol{\rho}, \boldsymbol{\rho}')$ satisfy Sommerfeld radiation condition at infinity, therefore integration over Γ_∞ (see Fig. 2.2) in the right hand side of Eq. (2.26) vanishes (see Eq. (A.7)). Notice that $\partial H_z(\boldsymbol{\rho})/\partial n$ is zero over the PEC ground plane except on the cavity aperture and $\partial G^h(\boldsymbol{\rho}, \boldsymbol{\rho}')/\partial n$ is zero on Γ (see Eq. (2.24)). Upon interchanging primed and unprimed coordinates, Eq. (2.26) reduces to

$$H_z(\boldsymbol{\rho}) = -j\omega\varepsilon_r \int_{\Omega_\infty} M_z(\boldsymbol{\rho}') G^h(\boldsymbol{\rho}, \boldsymbol{\rho}') d\Omega + \int_{\Gamma_B} G^h(\boldsymbol{\rho}, \boldsymbol{\rho}') \frac{\partial H_z(\boldsymbol{\rho}')}{\partial n'} d\Gamma. \tag{2.27}$$

Similar to the TM$_z$ case, the first term in the right hand side of Eq. (2.27) represents the magnetic field generated by the current filament and its image in the vicinity of the PEC ground plane. These fields are interpreted as an incident and reflected fields from the PEC screen [36]. The second term in Eq. (2.27) represents field perturbation due to the cavity. Then Eq. (2.27) can be rewritten as

$$H_z(\boldsymbol{\rho}) = H_z^{inc}(\boldsymbol{\rho}) + H_z^{ref}(\boldsymbol{\rho}) + \int_{\Gamma_B} G^h(\boldsymbol{\rho}, \boldsymbol{\rho}') \frac{\partial H_z(\boldsymbol{\rho}')}{\partial n'} d\Gamma. \tag{2.28}$$

By the same definition of $\boldsymbol{\rho}$ and $\boldsymbol{\rho}'$ and assuming the coordinate system as in Fig. 2.1, the incident and reflected fields can be written as

$$\begin{aligned} H_z^{inc}(\boldsymbol{\rho}) &= \exp(-jk_0(x\sin\theta - y\cos\theta)) \\ H_z^{ref}(\boldsymbol{\rho}) &= \exp(-jk_0(x\sin\theta + y\cos\theta)). \end{aligned} \tag{2.29}$$

To calculate the last term in Eq. (2.28), the partial derivative $\partial H_z(\boldsymbol{\rho}')/\partial n'$ can be conveniently expressed as a first-order finite difference as

$$\frac{\partial H_z(\boldsymbol{\rho}')}{\partial n'} = -\frac{H_z(x = x', y) - H_z(x', y')}{y - y'} \tag{2.30}$$

(notice that the negative sign on the right hand side of Eq. (2.30) is because $\hat{n'} = -\hat{y'}$),then the aperture Γ_B, and Γ_O are discretized into n segments with length of $\Delta x'$. By expanding both $H_z(x = x', y)$ and $H_z(x', y')$ over the aperture of cavity in terms of step functions as

$$H_z = \sum_{j=1}^{n} H_{zj} \psi_j(x'_j) \tag{2.31}$$

where

$$\psi_j(x') = \begin{cases} 1, & x'_j - \frac{\Delta x'_j}{2} < x'_j < x'_j + \frac{\Delta x'_j}{2}; \\ 0, & \text{elsewhere} \end{cases} \tag{2.32}$$

the singular behavior of the fields at the edges of the cavity can be avoided [36]. By replacing the field expansions in Eq. (2.28) and defining the elements of matrix $[S]$ as

$$S_{ij} = \int_{x'_j - \Delta x'_j/2}^{x'_j + \Delta x'_j/2} \frac{G^h(x_i, y, x'_j, y') \psi_j(x'_j)}{y - y'} dx' \tag{2.33}$$

where

$$G_h(x_i, y, x'_j, y' = 0) = -\frac{j}{2} H_0^{(2)} \left(k_0 \sqrt{(x_i - x'_j)^2 + y^2} \right). \tag{2.34}$$

Equation (2.28) can be represented in the matrix form as

$$\left[u_o\right] = \left[T\right] - \left[S\right] \left\{ \left[u_o\right] - \left[u_b\right] \right\} \tag{2.35}$$

where the elements of $[u_o]$, $[u_b]$, and $[T]$ matrices represent $H_z(x, y)$, $H_z(x', y')$, and $\big(H_z^{inc}(x, y) + H_z^{ref}(x, y)\big)$, respectively, at each node. Equation (2.35) can be rearranged as

$$\left[u_o\right] = \left\{ \left[I\right] + \left[S\right] \right\}^{-1} \left[T\right] + \left\{ \left[I\right] + \left[S\right] \right\}^{-1} \left[S\right] \left[u_b\right] \tag{2.36}$$

where $[I]$ is the unity matrix. Equation (2.36) represents the boundary constraint on the cavity opening. Combining Eq. (2.8) and Eq. (2.36) in matrix form results in the modified system matrix

$$\begin{bmatrix} M_{ii} & M_{ib} \\ M_{bi} & M_{bb} + M_{bo}(I + S)^{-1} S \end{bmatrix} \begin{bmatrix} u_i \\ u_b \end{bmatrix} = \begin{bmatrix} F_i \\ F_b - M_{bo}(I + S)^{-1} T \end{bmatrix}. \tag{2.37}$$

Equation (2.37) represents the modified system matrix which can be solved using commonly used methods for solving linear systems.

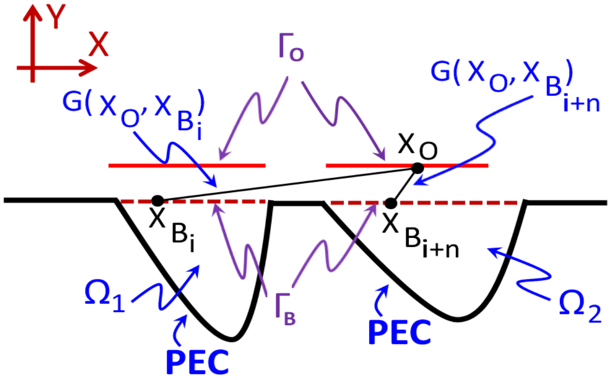

Figure 2.3: Schematic showing the extension the surface integral method to multiple cavities.

2.4 Extension to Multiple Cavities

In this section, extending the method developed above to the problem of scattering from multiple arbitrary shape cavities in a PEC surface is presented. A schematic representing the scattering problem for two cavities is shown in Fig. 2.3. Extending the finite element development in section 2.1 to two cavities, the system matrix for the domains Ω_1 and Ω_2 is generalized as

$$\begin{aligned}[M]^{(1)}[u]^{(1)} = [F]^{(1)}\\ [M]^{(2)}[u]^{(2)} = [F]^{(2)}\end{aligned} \tag{2.38}$$

where each system of equation can be represented symbolically as Eq. (2.8). Assembling the two systems using global numbering of nodes gives

$$\begin{bmatrix}[M]^{(1)} & 0\\ 0 & [M]^{(2)}\end{bmatrix}\begin{bmatrix}[u]^{(1)}\\ [u]^{(2)}\end{bmatrix} = \begin{bmatrix}[F]^{(1)}\\ [F]^{(2)}\end{bmatrix}. \tag{2.39}$$

The two system matrices arising from each of the two cavities will be coupled through the surface integral equation in the following manner. In Eq. (2.14) and Eq. (2.28), each node on Γ_O is connected via the Green's function to all the nodes on the aperture of the cavities, Γ_B, (see Fig. 2.3). In other words, the cavities are coupled to each other *only* through the surface integral equation and Green's function. In Eq. (2.14) and Eq. (2.28), the integration is performed over the apertures of all cavities. For instance, Eq. (2.14) for the TM$_z$ polarization can be represented symbolically in matrix form as

$$\begin{bmatrix}[u_o]^{(1)}\\ [u_o]^{(2)}\end{bmatrix} = \begin{bmatrix}[T]^{(1)}\\ [T]^{(2)}\end{bmatrix} + \begin{bmatrix}[S]^{(11)} & [S]^{(12)}\\ [S]^{(21)} & [S]^{(22)}\end{bmatrix}\begin{bmatrix}[u_b]^{(1)}\\ [u_b]^{(2)}\end{bmatrix} \tag{2.40}$$

where $[S]^{(ij)}$, represents connectivity between nodes on Γ_O of the i_{th} cavity $[u_o]^{(i)}$ and nodes on Γ_B of the j_{th} cavity $[u_b]^{(j)}$ via the surface integral equation (i & $j = 1, 2$). Combining

Eq. (2.40) and Eq. (2.39) in matrix form results in the modified system matrix as

$$\begin{bmatrix} [M_{ii}]^{(1)} & [M_{ib}]^{(1)} & 0 & 0 \\ [M_{bi}]^{(1)} & [M_{bb}]^{(1)} + [M_{bo}]^{(1)}[S]^{(11)} & 0 & [M_{bo}]^{(1)}[S]^{(12)} \\ 0 & 0 & [M_{ii}]^{(2)} & [M_{ib}]^{(2)} \\ 0 & [M_{bo}]^{(2)}[S]^{(21)} & [M_{bi}]^{(2)} & [M_{bb}]^{(2)} + [M_{bo}]^{(2)}[S]^{(22)} \end{bmatrix} \begin{bmatrix} [u_i]^{(1)} \\ [u_b]^{(1)} \\ [u_i]^{(2)} \\ [u_b]^{(2)} \end{bmatrix} = \begin{bmatrix} [F_i]^{(1)} \\ [F_b]^{(1)} - [M_{bo}]^{(1)}[T]^{(1)} \\ [F_i]^{(2)} \\ [F_b]^{(2)} - [M_{bo}]^{(2)}[T]^{(2)} \end{bmatrix}. \tag{2.41}$$

Integration over the apertures of all cavities results in addition of off-diagonal sub-matrices in Eq. (2.39). The resultant system matrix becomes

$$\begin{bmatrix} [M']^{(1)} & [C]^{(12)} \\ [C]^{(21)} & [M']^{(2)} \end{bmatrix} \begin{bmatrix} [u']^{(1)} \\ [u']^{(2)} \end{bmatrix} = \begin{bmatrix} [F']^{(1)} \\ [F']^{(2)} \end{bmatrix} \tag{2.42}$$

where $[C]^{(12)}$ and $[C]^{(21)}$ are matrices representing the coupling between the two cavities, and are given by

$$\begin{aligned} [C]^{(12)} &= \begin{bmatrix} 0 & 0 \\ 0 & [M_{bo}]^{(1)}[S]^{(12)} \end{bmatrix} \\ [C]^{(21)} &= \begin{bmatrix} 0 & 0 \\ 0 & [M_{bo}]^{(2)}[S]^{(21)} \end{bmatrix} \end{aligned} \tag{2.43}$$

and $[M']$ and $[F']$ are given by

$$\begin{aligned} [M']^{(1)} &= \begin{bmatrix} [M_{ii}]^{(1)} & [M_{ib}]^{(1)} \\ [M_{bi}]^{(1)} & [M_{bb}]^{(1)} + [M_{bo}]^{(1)}[S]^{(11)} \end{bmatrix} \\ [M']^{(2)} &= \begin{bmatrix} [M_{ii}]^{(2)} & [M_{ib}]^{(2)} \\ [M_{bi}]^{(2)} & [M_{bb}]^{(2)} + [M_{bo}]^{(2)}[S]^{(22)} \end{bmatrix} \\ [F']^{(1)} &= \begin{bmatrix} [F_i]^{(1)} \\ [F_b]^{(1)} - [M_{bo}]^{(1)}[T]^{(1)} \end{bmatrix} \\ [F']^{(2)} &= \begin{bmatrix} [F_i]^{(2)} \\ [F_b]^{(2)} - [M_{bo}]^{(2)}[T]^{(2)} \end{bmatrix} \end{aligned} \tag{2.44}$$

and $[u']^{(k)}$ is given by

$$[u']^{(k)} = \begin{bmatrix} [u_i]^{(k)} \\ [u_b]^{(k)} \end{bmatrix} \qquad (k = \ 1 \ \& \ 2). \tag{2.45}$$

Notice that these coupling matrices are not necessarily identical. The same procedure is applicable to the TE$_z$ polarization. Generalizing the formulation to N cavities results in the following system matrix:

$$\begin{bmatrix} [M']^{(1)} & [C]^{(12)} & \dots & [C]^{(1N)} \\ [C]^{(21)} & [M']^{(2)} & \dots & [C]^{(2N)} \\ \vdots & & \ddots & \vdots \\ [C]^{(N1)} & [C]^{(N2)} & \dots & [M']^{(N)} \end{bmatrix} \begin{bmatrix} [u']^{(1)} \\ [u']^{(2)} \\ \vdots \\ [u']^{(N)} \end{bmatrix} = \begin{bmatrix} [F']^{(1)} \\ [F']^{(2)} \\ \vdots \\ [F']^{(N)} \end{bmatrix}. \tag{2.46}$$

Once the nodal field values on Γ_O are expressed in terms of the nodal field values on Γ_B, the modified system of equations can be solved using commonly used methods for solving linear systems.

The formulation presented in this chapter is applicable to cavities present in perfectly conducting surfaces. For multiple cavities, equations (2.42) and (2.46) give a mathematical quantification of the coupling factors between the cavities. Physically, it is expected that the cavities to be coupled through surface currents existing on the segments connecting the cavities, as that is the only mechanism for energy transfer between the cavities. In the numerical solutions section below, the dependence of the surface currents on the distance between the cavities is presented.

2.5 Numerical Results

Once the system of equations, Eq. (2.21) for the TM$_z$ polarization or Eq. (2.37) for the TE$_z$ polarization, is derived, its solution (which is the field values at the aperture of the cavities) can be obtained using commonly used methods for solving linear systems. In this section, examples of cavities with different shapes, dimensions, and fillings are provided to validate the algorithm developed in this chapter.

To validate the method presented here, comparison was made to the results obtained using the mode matching technique (MMT) [30,31] or those obtained by the commercial two-dimensional finite-element simulator COMSOL [43]. While using the finite-element simulator for the comparison purpose, the absorbing boundary condition (ABC) was applied on the artificial boundary to truncate the computational domain (see Fig. 2.4). Throughout this work, these solutions is referred as (COMSOL). Without loss of generality, the magnitude of the incident electric field is assumed to be unity throughout this section. To implement the algorithm developed in this work, a nodal based finite element formulation is used. The solution domain is discretized using first-order triangle elements with a mesh density of approximately 20 nodes per λ for the TM$_z$ case. Since there is a discontinuity in the electric field at the edges of the cavities in the TE$_z$ case, a mesh density of 100 nodes

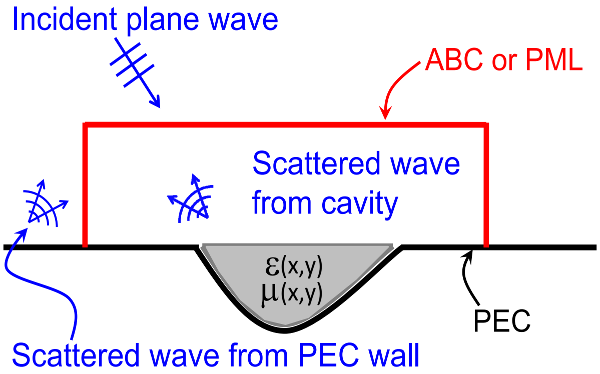

Figure 2.4: Schematic of the computational domain truncation using ABC or PML in solving the scattering problem from a cavity with arbitrary shape in an infinite PEC surface.

per λ is used. Throughout this section, the solution obtained using the method presented in this chapter is referred to as “Total Field Surface Integral Equation” (TFSIE).

2.5.1 Single Cavity Case

In the first example, a $1\lambda \times 1.5\lambda$ (width×depth) rectangular cavity is considered where λ is the wavelength in free space. Figures 2.5 shows the total electric field at the aperture of the cavity for TM_z incident plane wave, and oblique incident angle. Comparison is made to the results published in [30] using the mode matching method as well as the result obtained using COMSOL.

The results in Fig. 2.5 show strong agreement between the calculations using TFSIE and those obtained using COMSOL and the mode matching method. In the case of COMSOL, the required computational domain was approximately $60\lambda^2$ using 4094 elements. This COMSOL computational domain was needed so that solution would converge to the mode matching solution. On the other hand, the TFSIE solution space was confined to the cavity area of $1.5\lambda^2$.

In the second example, a $0.6\lambda \times 0.4\lambda$ rectangular cavity is considered. Figure 2.6 shows the total magnetic field at the aperture of the cavity for TE_z impinging wave for oblique incident angle. The comparison is made with the results obtained using COMSOL. Close agreement is observed between TFSIE results and those of COMSOL. Notice that computational domain in the case of COMSOL was $150\lambda^2$ to obtained converged results.

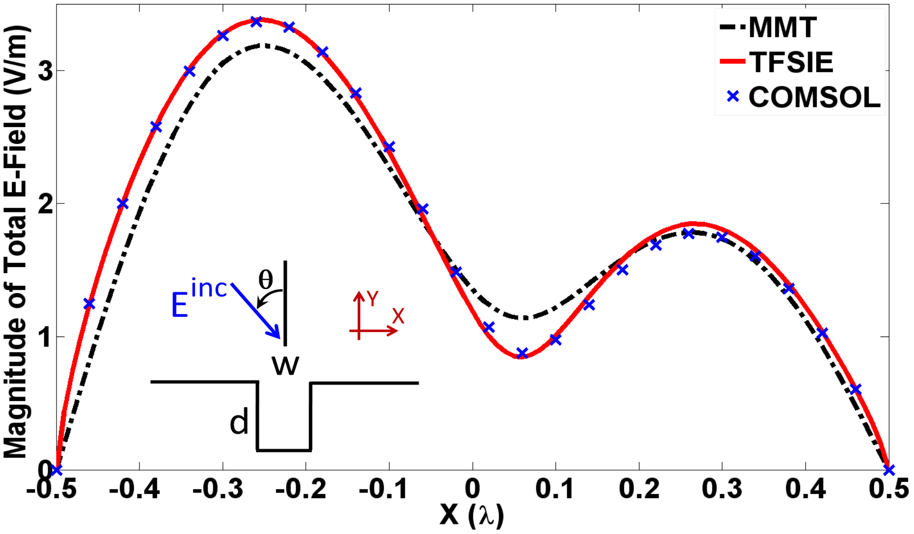

Figure 2.5: Amplitude of total E-field at the aperture of a $1\lambda \times 1.5\lambda$ air-filled rectangular cavity, TM_z case, $\theta = 45°$, calculated using the method introduced in this work (TFSIE), mode matching technique (MMT), and COMSOL.

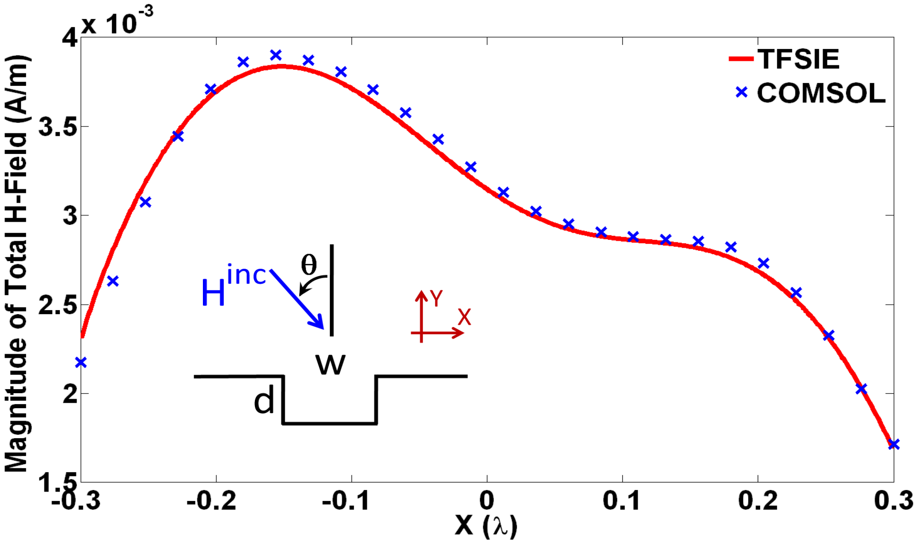

Figure 2.6: Amplitude of total H-field at the aperture of a $0.6\lambda \times 0.4\lambda$ air-filled rectangular cavity, TE_z case, $\theta = 45°$, calculated using the method introduced in this work (TFSIE), and COMSOL.

To show the versatility of the method introduced in this chapter in solving problem of scattering from cavities with arbitrary shapes and fillings, an isosceles right triangle

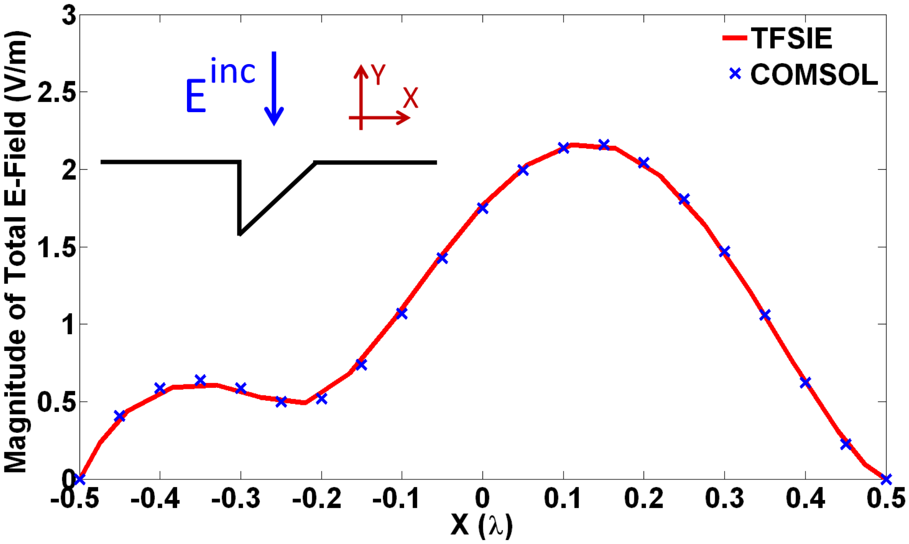

Figure 2.7: Amplitude of total E-field at the aperture of an isosceles right triangle air-filled cavity with aperture size of 1λ, TM_z case, normal incident, calculated using the method introduced in this work (TFSIE), and COMSOL.

air-filled cavity with an aperture of 1λ (Fig. 2.7) for the case of normal incidence, and a dielectric filled ($\varepsilon_r = 10$) semi-circle cavity with radius of $R = 0.4\lambda$ (Fig. 2.8) for the case of oblique incidence, are considered. Figures 2.7, and 2.8 represent total electric field at the aperture of the cavities for TM_z polarization. Strong agreement between the results calculated using TFSIE and those obtained using COMSOL is observed in both figures.

2.5.2 Multiple Cavities

As an example of multiple cavities, six identical cavities in a PEC surface are considered. The cavities are rectangular with dimension of $0.8\lambda \times 0.4\lambda$ and are separated by a distance of 0.8λ. In this example, the field solution at the opening of the cavities and the far field are presented. The far-field can be calculated using the equivalence principle. By closing the aperture by a PEC surface and introducing an equivalent magnetic current $\boldsymbol{M}(x', y')$ at the aperture, the electric field at far region can be represented as

$$\boldsymbol{E}(x, y) = -2\boldsymbol{\nabla} \times \int_{\Gamma_B} \boldsymbol{M}(x', y') G(x, y, x', y') dx' \tag{2.47}$$

where $\boldsymbol{M}(x', y') = -\hat{n} \times \boldsymbol{E}(x', y')|_{y'=0}$ and $G(x, y, x', y')$ is the free-space Green's function

$$G(x, y, x', y') = -\frac{j}{4} H_0^{(2)}(k_0 R) \tag{2.48}$$

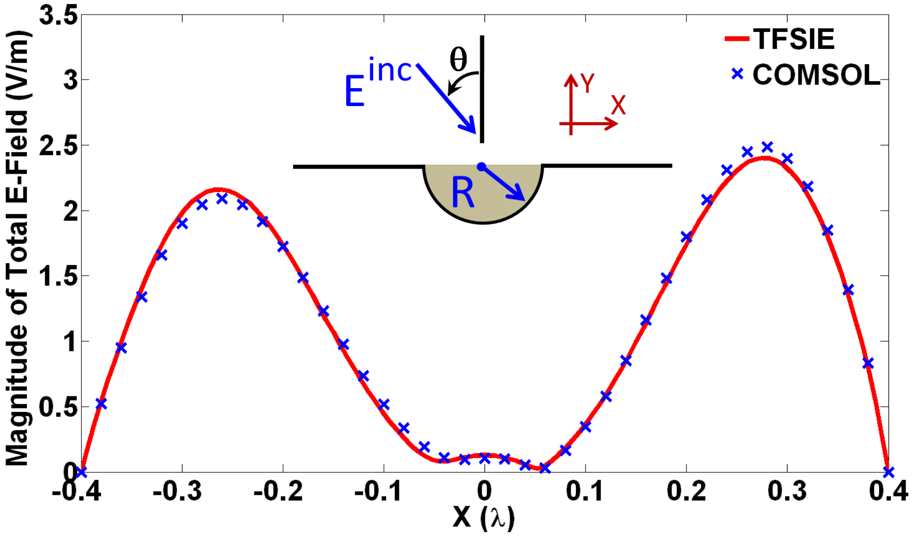

Figure 2.8: Amplitude of total E-field at the aperture of a semi-circle cavity with radius of 0.4λ, dielectric-filled ($\varepsilon_r = 10$), TM$_z$ case, $\theta = 30°$, calculated using the method introduced in this work (TFSIE) and COMSOL.

where $R = ((x-x')^2 + (y-y')^2)^{\frac{1}{2}}$. For the TM$_z$ case where the electric field has only a z-component, Eq. (2.47) can be written as

$$\boldsymbol{E}(x,y) = -\hat{z}\int_{\Gamma_B} 2E_z(x',y')|_{y'=0}\frac{\partial G}{\partial y}dx'. \tag{2.49}$$

For the TE$_z$ case where the magnetic field has only a z-component, the electric field at the aperture has two components. Therefore Eq. (2.47) can be written as

$$\boldsymbol{E}(x,y) = \frac{-2}{j\omega\varepsilon_r}\left(\hat{x}\int_{\Gamma_B}\frac{\partial H_z(x',y')}{\partial y'}|_{y'=0}\frac{\partial G}{\partial y}dx' - \hat{y}\int_{\Gamma_B}\frac{\partial H_z(x',y')}{\partial y'}|_{y'=0}\frac{\partial G}{\partial x}dx'\right). \tag{2.50}$$

Figures 2.9 and 2.10 show the total electric field at the apertures of the cavities and the far field, respectively, for the case of an oblique TM$_z$ incident plane wave. Strong agreement is observed between TFSIE and the mode matching method [31].

Figure 2.11 shows the total magnetic field at the aperture of two identical $0.4\lambda \times 0.2\lambda$ rectangular cavities separated by 0.2λ, TE$_z$ case, for oblique incidence. Strong agreement between TFSIE and COMSOL is observed aside from small deviation at the edges of the cavities due to field singularities there.

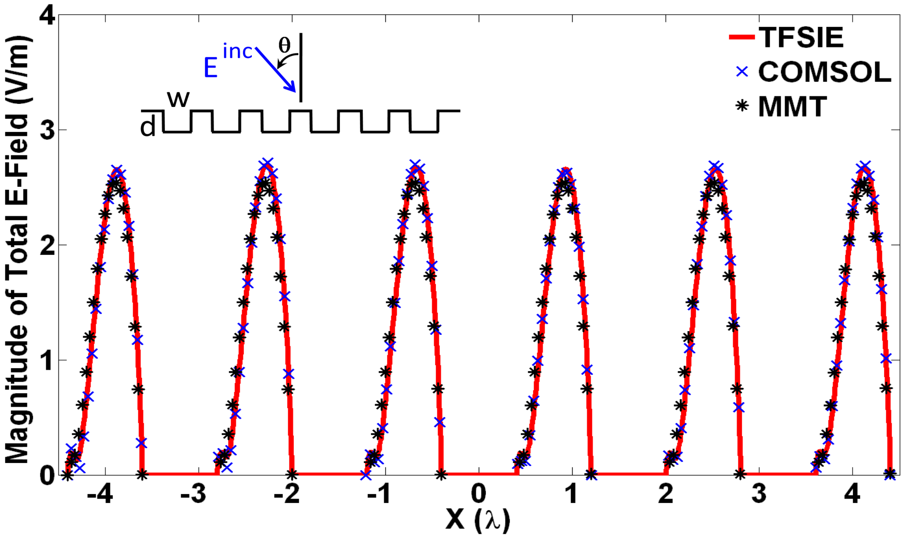

Figure 2.9: Amplitude of total E-field at the aperture of six identical $0.8\lambda \times 0.4\lambda$ air-filled rectangular cavities, TM_z case, $\theta = 30°$, calculated using the method introduced in this work (TFSIE), the mode matching technique (MMT), and COMSOL. The cavities are separated by 0.8λ.

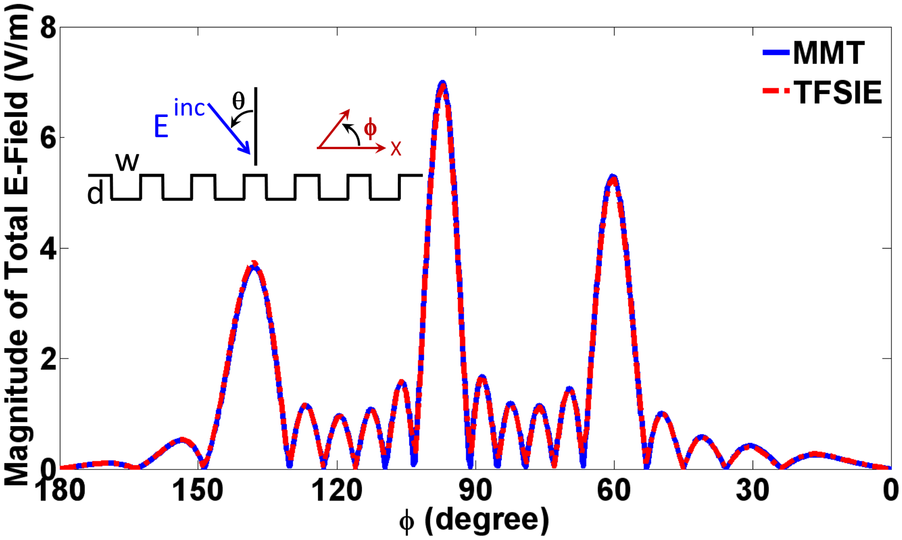

Figure 2.10: Amplitude of the far-field for six identical $0.8\lambda \times 0.4\lambda$ air-filled rectangular cavities, TM_z case, $\theta = 30°$, calculated using the method introduced in this work (TFSIE), and the mode matching technique (MMT). The cavities are separated by 0.8λ.

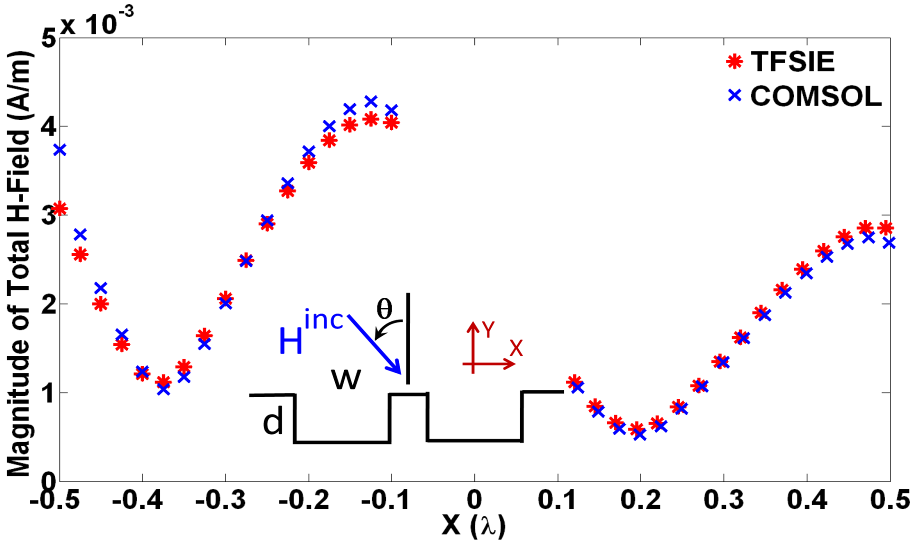

Figure 2.11: Amplitude of total H-field at the aperture of two identical $0.4\lambda \times 0.2\lambda$ air-filled rectangular cavities, TE$_z$ case, $\theta = 45°$, calculated using the method introduced in this work (TFSIE), and COMSOL. The cavities are separated by 0.2λ.

Using the coordinate system as Fig. 2.3, the surface current can be calculated as

$$\boldsymbol{J}(x) = \hat{z}\frac{1}{j\omega\mu_r}\frac{\partial E_z}{\partial y} \tag{2.51}$$

for the TM$_z$ polarization, and

$$\boldsymbol{J}(x) = \hat{y} \times \boldsymbol{H} = \hat{x}H_z \tag{2.52}$$

for the TE$_z$ polarization. In Eq. (2.51) and (2.52), E_z and H_z represent the total fields. Figures 2.12 and 2.13 show the magnitude of surface current for normal and oblique TM$_z$-polarized incident waves. It is observed that the induced current on the PEC surface increases as the cavity separation decreases. The magnitude of the incident field and the reflected field on the PEC surface are the same for both closely separated and distanced cavities. Thus, the change in surface current is due to the scattered field from the cavities. Since the scattered field affects the field distribution on the other cavities, the magnitude of the surface current can be interpreted as a coupling factor between the cavities.

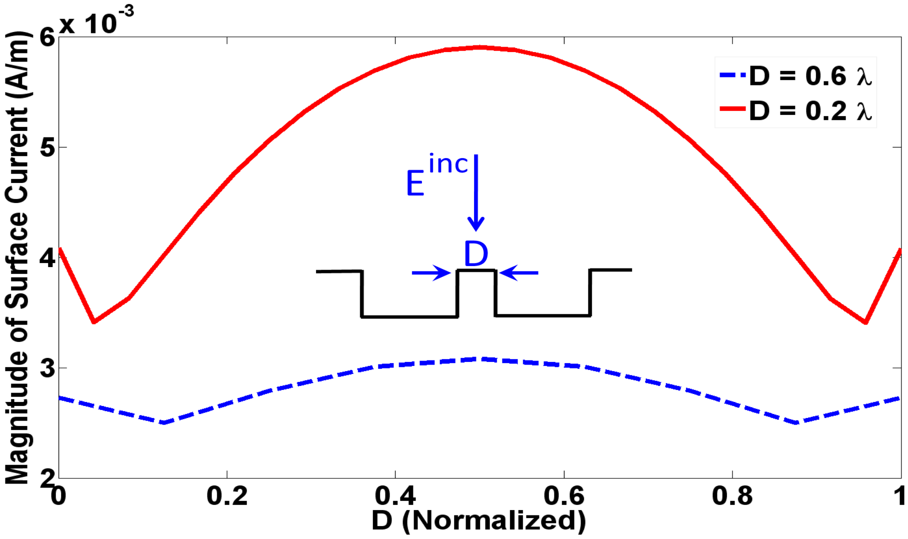

Figure 2.12: Amplitude of the surface current on a PEC surface between two $0.8\lambda \times 0.4\lambda$ air-filled rectangular cavities, TM_z case, normal incident, calculated using the method introduced in this work (TFSIE).

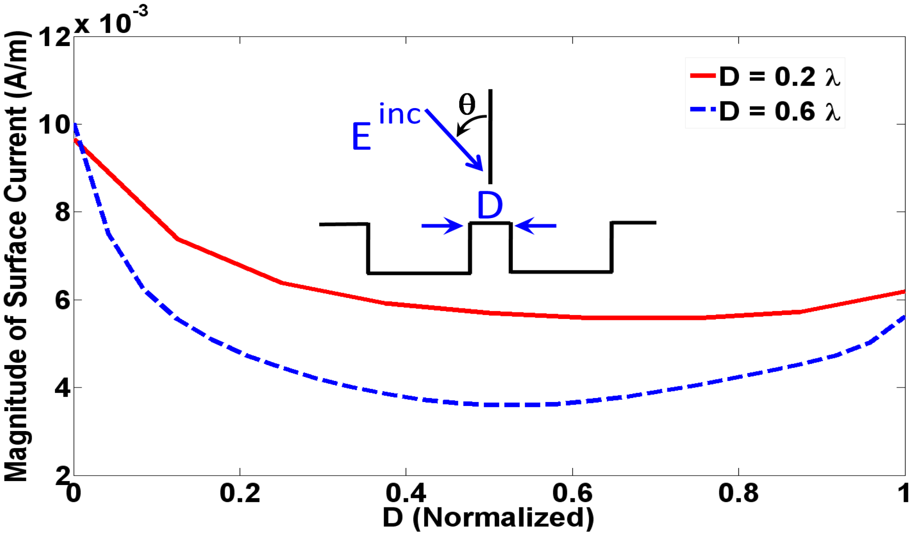

Figure 2.13: Amplitude of the surface current on a PEC surface between two $0.8\lambda \times 0.4\lambda$ air-filled rectangular cavities, TM_z case, $\theta = 45°$, calculated using the method introduced in this work (TFSIE).

Chapter 3

Fundamental Limitations on the Use of Absorbing Boundary Condition to Solve the Problem of Scattering from Gratings in Conducting Surfaces

When solving the scattering problem from a bounded target using finite mathematics, it is essential to introduce an artificial boundary to truncate the solution region surrounding the target. Appropriate boundary condition must be imposed on the artificial boundary to guarantee a well-posed and unique solution to the wave equation. In addition, the boundary condition must model the behavior of the wave at infinity. In other words, the artificial boundary must to be as transparent as possible for impinging waves from the interior region.

There are two types of boundary conditions to truncate the solution region, viz., (i) non-local or integral type; (ii) local or differential type. Non-local type of boundary conditions are analytical integral equations which accurately model the behavior of the wave at the boundaries [32]. Therefore they are exact for all range of incident angles. In addition, they can be imposed on the boundary which is very close to the scatterer body. The major drawback of these type of boundary condition is that they result in dense system matrix which spoils the sparsity of the FE system matrix. In contrast, local type of boundary conditions are partial differential equations which approximate the exact behavior of the wave at the artificial boundary [44–46].

When solving the problem of scattering from infinite grating surfaces containing multiple cavities using non-local boundary conditions, the solution region can be truncated at the opening of the cavities (see chapter 2). In chapter 2, the domain of the surface integral

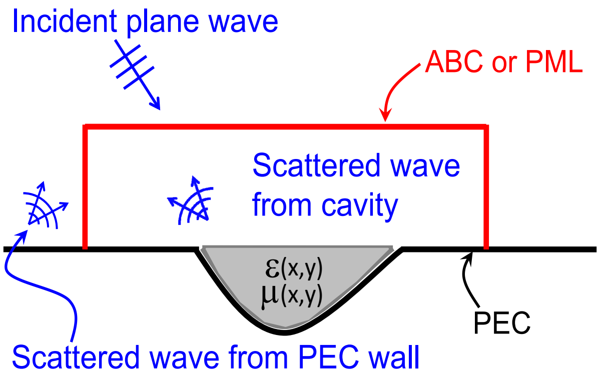

Figure 3.1: Schematic of the scattering problem from a cavity with arbitrary shape in an infinite PEC surface. An ABC or PML is used to truncate the computational domain.

equation as a boundary constraint is limited to the aperture of the cavities, and, thus, the infinitely extended perfect electric conducting (PEC) walls have no contribution in calculating the boundary condition. On the other hand, a difficulty in truncating the solution region arises when using local boundary conditions or matched layers (typically referred to in the literature as Absorbing Boundary Conditions, ABC, or Perfectly Matched Layer, PML) in solving the problem of scattering from gratings in infinite PEC screens. Since it is impossible to fully enclose the scatterer's geometry by the ABC or PML, the behavior of the scattered field due to the infinite PEC wall outside of the computational domain boundary cannot be modeled properly (see Fig. 3.1). Therefore, errors can be generated in the solution when using ABC or PML even if the truncation boundary is receded.

In this chapter the performance of commonly used ABC or PML in solving the problem of scattering from grating surface containing a single or multiple cavities engraved in an infinite PEC screen is analyzed. In particular, the author focused on the errors introduced in the solution due to grazing incident waves. Next, the dependance of this error on the location of the ABC is analyzed. The errors were calculated by comparison to the solutions obtained using an TFSIE introduced in chapter 2 and the mode matching technique reported in [25].

3.1 General Description of the Problem

As a representative example of the problem of scattering from gratings in metallic screens, the problem depicted in Fig. 3.1 which shows an electromagnetic wave impinging on a cavity engraved in an infinite metallic wall is considered. The solution region can be truncated using the ABC as a local boundary condition as it is shown in Fig. 3.1.

Because generic types of ABCs and PMLs are ineffective in absorption of evanescent waves, the introduced error due to these mesh truncation techniques is in general inversely proportional to the distance between the truncation walls and the cavity. Therefore, ABC or PML cannot be located very close to the cavity. In addition, it is impossible to fully enclose the scatterer's geometry by an ABC or PML. Therefore, the behavior of the scattered field due to the PEC surface that lies outside of the computational domain boundary cannot be modeled properly and thus any consequential physical interaction cannot be included in the solution. In fact, more explicitly, as can be shown in Fig. 3.1, a portion of the scattered field from the PEC wall which propagates into the solution region is ignored and therefore, an error is introduced to the solution. The error would most likely depend on the incident angle. By increasing the incident angle, more energy is reflected into the solution region by the PEC walls located outside of the ABC, whereas, at zero angle of incidence, the reflected energy from the surface surrounding the cavity does not enter the computational domain depicted in Fig. 3.1. Therefore this error is expected to increase as the incident angle increases. To minimize this error, the domain truncating boundaries should be located far enough from the cavity to enclose a larger segment of the PEC wall in addition to the cavity. However, placing the boundary of the computational domain far from the cavity leads to prohibitive increase in the computational cost, in addition to inaccuracy in the solution due to the exclusion of a large part of the scatterer. (The computational cost is most critical when considering cavities whose size is several wavelengths, and when loading the cavities to minimize RCS, requiring extensive optimizations). Notice also that enlarging the computational domain by including a larger segment of the PEC wall while keeping the upper boundary (the horizontal terminating boundary in Fig. 3.1) very close to the PEC wall does not reduce the errors as in such scenario the upper boundary experiences a large concentration of waves incident at oblique angles, which cannot be absorbed effectively by typical PML or ABC methods. (There are specialized ABC or PML methods that are designed to absorb waves incident at oblique angles, or even effectively absorb evanescent waves such as in [47,48], however, these truncation techniques are specialized and typically add additional computational overhead.)

3.2 Numerical Results

To study the limitations on the use of ABC or PML to truncate the computational domain for the gratings problems considered in this chapter, the highly robust and widely used full-wave simulator, HFSS [49] which employs a highly effective implementation of PML was used for comparison purposes. The author emphasizes that the purpose of the comparison is to accentuate the limitations of PML or ABC rather than the effectiveness of the simulator in general. Since the PML implementation in HFSS provides much higher accuracy than the ABC implementation in the same solver, the comparison was made to the solution obtained using PML. This solution henceforth will be referred to as HFSS-PML. However, in the first example the results obtained using ABC are showed as a benchmark. This solution is referred as HFSS-ABC. It is important to note that HFSS uses multilayer biaxial anisotropic materials in the PML implementation [50].

In the absence of analytical solutions to the problem of scattering from cavities, the solutions generated by two methods will be used for gauging the errors caused by the HFSS-PML or HFSS-ABC solutions. The first method, which was introduced in chapter 2 employs the surface integral equation to truncate the computational domain at the aperture of the cavity, and the second method employs the mode matching techniques [25]. These two solutions are considered highly accurate in the sense that the approximations used in their respective solution procedures involve discretization of the field rather than any boundary condition approximations. The solutions presented here are made over a wide range of incident angles. For the transverse magnetic incident plane wave where the electric field vector lies along the axis of the cavities, the error in the magnitude of the total electric field at the aperture of the cavity is calculated as

$$err. = \sqrt{\frac{\int (E - E_0)^2 \, d\xi}{\int E_0^2 d\xi}} \times 100\% \tag{3.1}$$

where E is the total electric field obtained using the HFSS-PML or HFSS-ABC solutions and E_0 is total electric field calculated using the surface integral equation method reported in chapter 2 referred as (TFSIE), or the mode matching technique [25], respectively. The integration domain is the aperture of the cavities.

In the first example, a $0.8\lambda \times 0.4\lambda$ $(width \times depth)$ rectangular cavity in a PEC sheet was considered where λ is the wavelength in free space. The solution region using HFSS-PML or HFSS-ABC is truncated by a rectangular mesh. The vertical distance of the truncation boundary from the PEC screen is $h = 1\lambda$ and the distance of the lateral truncation walls D from the edge of the cavity is set to be 4λ (see inset of Fig. 3.2). Figure 3.2 shows the error using the results calculated using TFSIE and the mode matching technique for incident angle range of $0° - 85°$. It is observed that by increasing the incident angle, the error increases in an almost exponential trend. This is because by increasing the incident angle, more reflected waves from the PEC screen outside of the PML or ABC which propagate into the solution region are ignored. As it is shown in Fig. 3.2, the increment trend is uniform in HFSS-PML case while it highly depends on incident angles in HFSS-ABC case for $\theta > 30°$. To validate this reason, the distance of the lateral truncation walls (i.e. D) from the cavity was changed.

Figure 3.3 shows the effect of increasing D on the error for grazing incident angle of $\theta = 85°$ By increasing the D from 4λ to 16λ, the error decreases from 37% to 8% in HFSS-PML case. Notice that to achieve 8% solution accuracy, a computational space

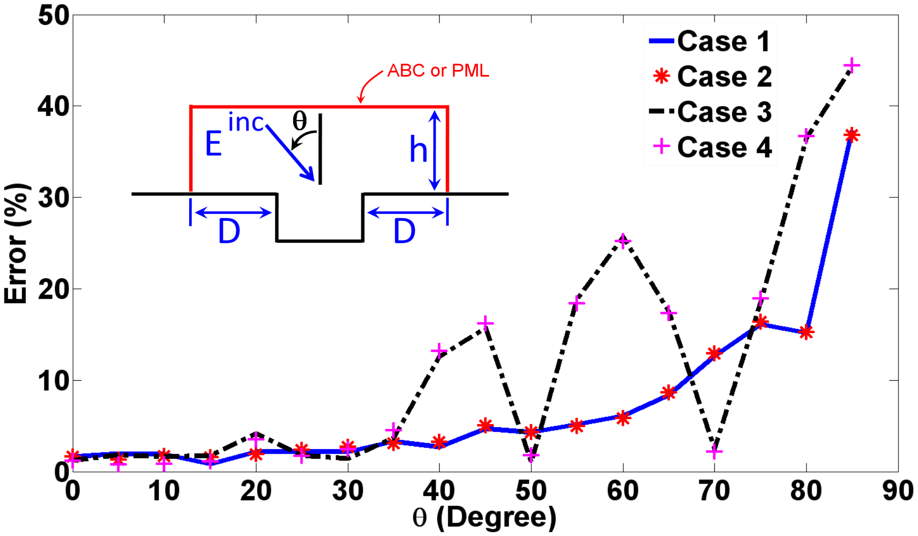

Figure 3.2: Error versus incident angle (θ) for a $0.8\lambda \times 0.4\lambda$ air-filled rectangular cavity, TM_z case, $D = 4\lambda$, $h = 1\lambda$. Error between results obtained using: Case1: HFSS-PML and TFSIE, Case2: HFSS-PML and mode matching technique, Case3: HFSS-ABC and TFSIE, Case4: HFSS-ABC and mode matching technique.

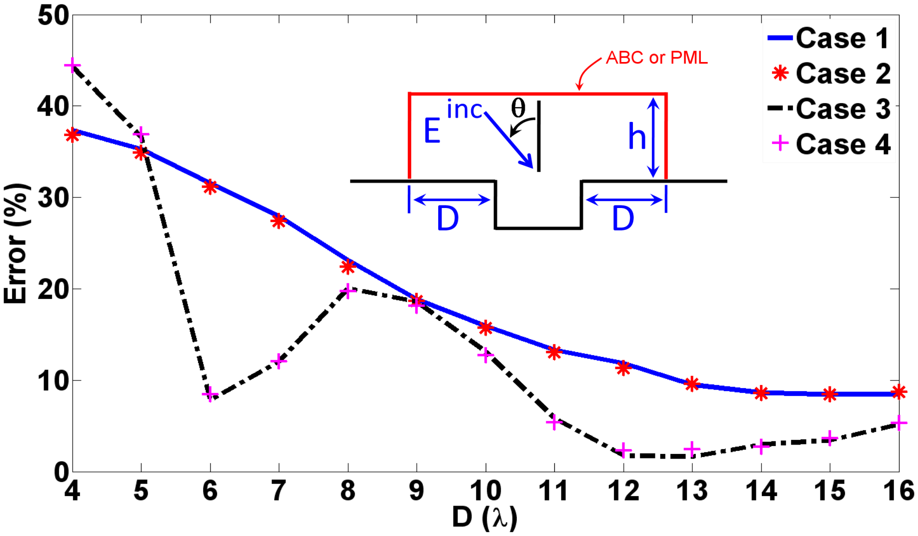

Figure 3.3: Error versus distance (D) of the lateral PML walls from a $0.8\lambda \times 0.4\lambda$ air-filled rectangular cavity, TM_z case, $\theta = 85°$, $h = 1\lambda$. Error between results obtained using: Case1: HFSS-PML and TFSIE, Case2: HFSS-PML and mode matching technique, Case3: HFSS-ABC and TFSIE, Case4: HFSS-ABC and mode matching technique.

of approximately $32\lambda^2$ would be needed when using a PML-based truncation technique; whereas, the solution space using TFSIE which is confined to the cavity's area, would require a computational domain of $0.32\lambda^2$. (It is important to emphasize here that while approximate computational areas are used to highlight the efficiency and accuracy of the methods discussed here, other aspects of different code implementations are intentionally not discussed here such as the algorithm used to solve the systems matrix, the type of bases functions used in the finite element method implementation, ...etc.)

As a second example, five identical cavities in a PEC screen are considered. The cavities are rectangular with dimension of $0.8\lambda \times 0.4\lambda$ and are separated by a distance of 0.2λ. The vertical distance of the mesh truncation wall from the PEC screen is $h = 1\lambda$ and the distance of the lateral truncation walls from the cavities is set to be $D = 4\lambda$ (see the inset of Fig. 3.4). Figure 3.4 shows the error for incident angle varying from $\theta = 0°$ to $\theta = 85°$. Figure 3.5 shows the decrease in the cavity field error from 30% to 14% when D is increased from 4λ to 16λ. Notice that despite the excessive computational domain needed when D is increased to 16λ resulting in a computational domain of $37\lambda^2$, the error in the apertures field remains above 10%.

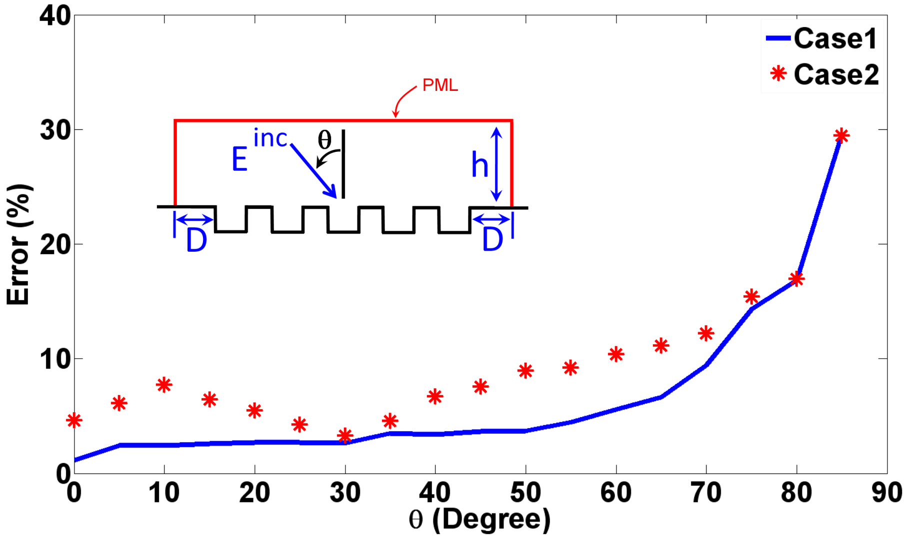

Figure 3.4: Error versus incident angle (θ) for five identical $0.8\lambda \times 0.4\lambda$ air-filled rectangular cavities, TM_z case, $D = 4\lambda$, $h = 1\lambda$. The cavities are separated by 0.2λ. Error between results obtained using: Case1: HFSS-PML and TFSIE, Case2: HFSS-PML and mode matching technique.

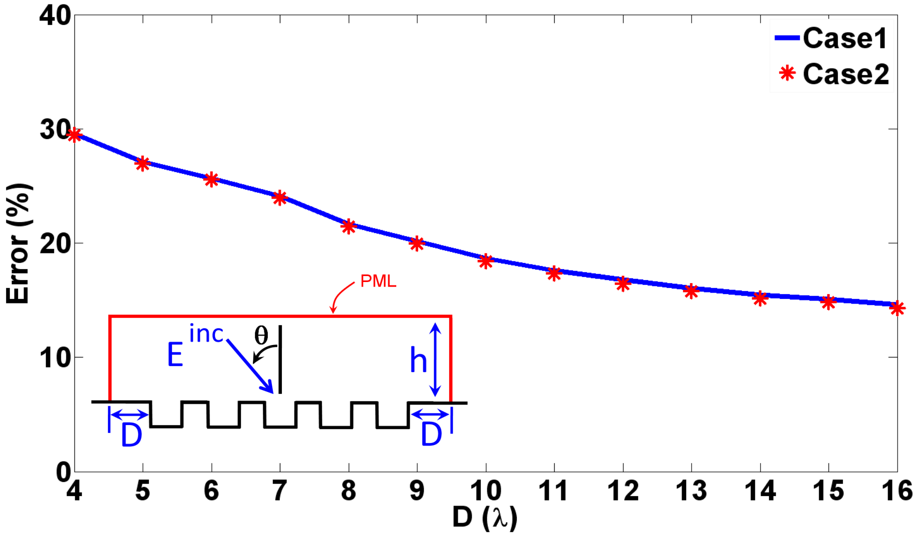

Figure 3.5: Error versus distance (D) of the lateral PML walls from the marginal cavities in an array of five identical $0.8\lambda \times 0.4\lambda$ air-filled rectangular cavities, TM_z case, $\theta = 85°$, $h = 1\lambda$. The cavities are separated by 0.2λ. Error between results obtained using: Case1: HFSS-PML and TFSIE, Case2: HFSS-PML and mode matching technique.

Chapter 4

Scattering from Holes in Conducting Screens

In this chapter, the method introduced in chapter 2 is extended to solve the problem of scattering from multiple holes in infinite metallic screens. Using the two-boundary formulation, the unbounded region in the computational domain is divided into bounded frames containing each hole plus a thin layer above the apertures of the hole in the upper half-space and lower half-space. These thin layers are limited to the width of the each hole (see Fig. 4.1). The finite-element formulation is used to obtain the solution of Helmholtz's equation inside the local frames. The surface integral equation using a half-space Green's function is applied at each opening of the holes as a global boundary condition to determine the behavior of nodes on the local frame boundary in terms of interior nodes. The Neumann or Dirichlet boundary condition is applied on the PEC walls of the holes in the TE or TM case, respectively.

In this formulation, it is shown that by appropriate modification of the Green's function, the surface integral is limited to the aperture of the holes at both the upper half-space and the lower half-space since it is zero on the PEC wall. Therefore, the extension of the method introduced in chapter 2 for cavities to the holes does not pose any particular challenge under the total field formulation. The method presented here is applicable to both TM and TE polarization cases.

4.1 Finite-Element Formulation of the Problem

Figure 4.1 shows a 2-D hole having an arbitrary shape in perfectly conductor surface and illuminated by obliquely incident plane wave. The angle θ represents the angle of the

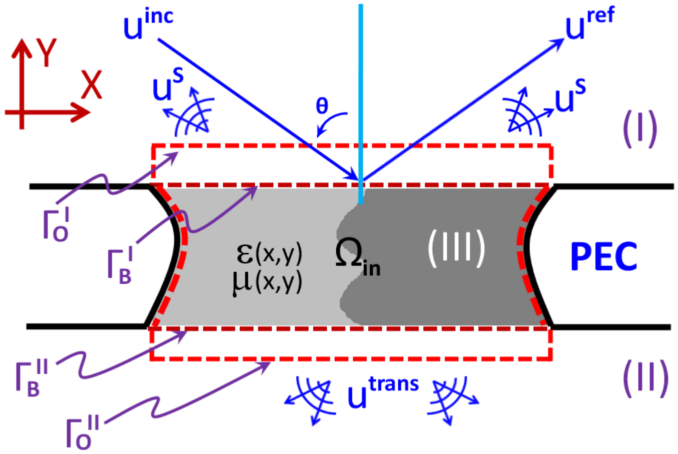

Figure 4.1: Schematic of the scattering problem from a hole in a PEC surface. The dotted line represents bounded region which contains all sources, inhomogeneities and anisotropies.

incident wave, and u^{inc}, u^{ref}, u^{s}, and u^{trans} denote the incident field, reflected field by the PEC screen, scattered field by the aperture of the hole, and transmitted fields through the hole, respectively, along the hole axis. Lets divide the problem into three regions. Region I and II denote the upper and lower half-spaces of the PEC slab. Region III represents inside the hole. Let Γ_B^I and Γ_B^{II} represent the contour at the interface of the hole openings with region I and II, respectively. Also let Γ_O^I and Γ_O^{II} as the exterior contour in close vicinity of Γ_B^I and Γ_B^{II}, respectively. Let Ω_{in} denote the interior region of the hole, region III, including the layer between Γ_B and Γ_O in the region I and II. By discretizing the solution domain Ω_{in} into triangular elements, the unknown total field u^t over each element is described by the set of interpolating functions given by Eq. (2.1). The conventional finite element formulation is used inside each element to obtain the weak form of Helmholtz's equation:

$$\boldsymbol{\nabla}\cdot\left(\frac{1}{p(x,y)}\boldsymbol{\nabla}u^t\right)+{k_0}^2q(x,y)u^t=g \tag{4.1}$$

where u^t, $p(x,y)$, $q(x,y)$, and k_0 have the same definition as in section 2.1. Also the time harmonic factor $\exp(j\omega t)$ is assumed and suppressed throughout this chapter. Following the procedure in section 2.1, the Galerkin-weighted residual integral for each element R^e can be expressed in matrix form as

$$R^e=\left[M^e\right]\left[u^e\right]-\left[F^e\right]=0 \tag{4.2}$$

where the elements of matrices M^e, and F^e are given by Eq. (2.7). By assembling all local system matrices Eq. (4.2) the global system matrix can be represented symbolically as

$$\begin{bmatrix} M_{ii} & M_{ib^I} & M_{ib^{II}} & 0 & 0 \\ M_{b^Ii} & M_{b^Ib^I} & 0 & M_{b^Io^I} & 0 \\ M_{b^{II}i} & 0 & M_{b^{II}b^{II}} & 0 & M_{b^{II}o^{II}} \\ 0 & M_{o^Ib^I} & 0 & M_{o^Io^I} & 0 \\ 0 & 0 & M_{o^{II}b^{II}} & 0 & M_{o^{II}o^{II}} \end{bmatrix} \begin{bmatrix} u_i \\ u_{b^I} \\ u_{b^{II}} \\ u_{o^I} \\ u_{o^{II}} \end{bmatrix} = \begin{bmatrix} F_i \\ F_{b^I} \\ F_{b^{II}} \\ F_{o^I} \\ F_{o^{II}} \end{bmatrix} \tag{4.3}$$

where u_i, u_{b^I}, $u_{b^{II}}$, u_{o^I}, and $u_{o^{II}}$ represent nodal field values inside the hole, on Γ_B^I, Γ_B^{II}, Γ_O^I and on Γ_O^{II}, respectively. The $[F]$ matrix represents impressed sources at each node, therefore, $[F]$ is zero in this problem.

The linear system of equations in Eq. (4.3) represents the relationship between the nodal field values without any external constraint. In next section, the surface integral equation will be developed as a boundary constraint to modify the system matrix equation of Eq. (4.3).

4.2 Surface Integral Equation for $\mathrm{TM_z}$ Polarization

In this section, the surface integral equation using the Green's function of first kind will be derived and used to express the nodal field values on Γ_O in terms of the nodal field values on Γ_B in region I and II, respectively.

4.2.1 Upper Half-Space (Region I)

Let us consider the domain Ω_∞^I representing the half-space above the PEC (see Fig. 4.2). In Ω_∞^I and for the TM_z polarization case, the electric field vector has only a z-component satisfying Helmholtz's equation:

$$\nabla^2 E_z(\boldsymbol{\rho}) + {k_0}^2 E_z(\boldsymbol{\rho}) = j\omega\mu_r J_z(\boldsymbol{\rho}), \qquad \boldsymbol{\rho} \in \Omega_\infty^I \tag{4.4}$$

where $J_z(\boldsymbol{\rho})$ is an electric current inside Ω_∞^I. Let us introduce the Green's function $G_e^I(\boldsymbol{\rho}, \boldsymbol{\rho}')$ which is the solution due to an electric current filament located at $\boldsymbol{\rho}'$ and governed by Helmholtz's equation

$$\nabla^2 G_e^I(\boldsymbol{\rho}, \boldsymbol{\rho}') + {k_0}^2 G_e^I(\boldsymbol{\rho}, \boldsymbol{\rho}') = -\delta(\boldsymbol{\rho} - \boldsymbol{\rho}') \qquad \boldsymbol{\rho}, \boldsymbol{\rho}' \in \Omega_\infty^I. \tag{4.5}$$

$G_e^I(\boldsymbol{\rho}, \boldsymbol{\rho}')$ satisfies the boundary condition $G_e^I(\boldsymbol{\rho}, \boldsymbol{\rho}')\big|_{y=0} = 0$ (i.e., $G_e^I = 0$ on Γ^I) and Sommerfeld radiation condition at infinity. $G_e^I(\boldsymbol{\rho}, \boldsymbol{\rho}')$ is easily found to be the zeroth-order

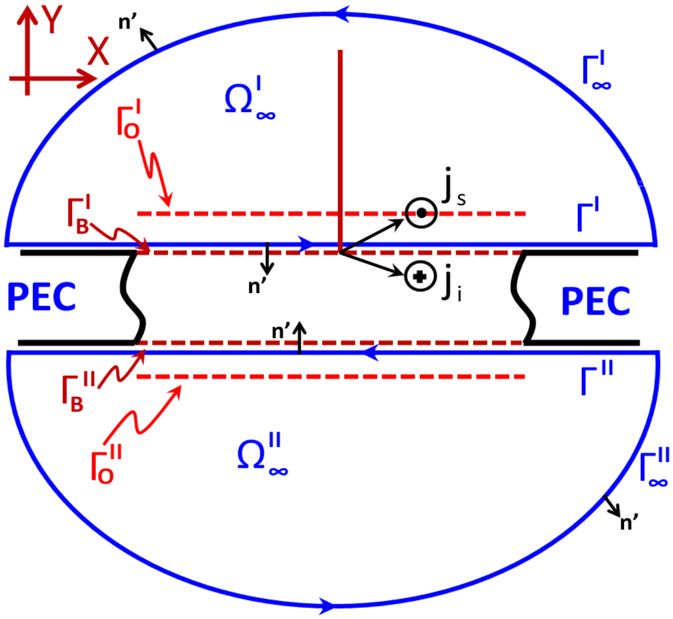

Figure 4.2: Schematic of the surface integral contour in the upper half-space and the lower half-space of a hole.

Hankel function of the second kind:

$$G_e^I(\boldsymbol{\rho}, \boldsymbol{\rho}') = -\frac{j}{4} H_0^{(2)}(k_0 |\boldsymbol{\rho} - \boldsymbol{\rho}'_{\mathrm{s}}|) + \frac{j}{4} H_0^{(2)}(k_0 |\boldsymbol{\rho} - \boldsymbol{\rho}'_{\mathrm{i}}|) \tag{4.6}$$

where $\boldsymbol{\rho}'_{\mathrm{s}}$, and $\boldsymbol{\rho}'_{\mathrm{i}}$ represent the position of the source current, and its image, respectively. The surface integral equation (Eq. (A.6)) in region I for the TM$_z$ polarization, can then be written as

$$\begin{aligned} E_z(\boldsymbol{\rho}') = & - j\omega\mu_r \int_{\Omega_\infty^I} J_z(\boldsymbol{\rho}) G_e^I(\boldsymbol{\rho}, \boldsymbol{\rho}') d\Omega^I \\ & - \oint_{\Gamma^I + \Gamma_\infty^I} \left(E_z(\boldsymbol{\rho}) \frac{\partial G_e^I(\boldsymbol{\rho}, \boldsymbol{\rho}')}{\partial n} - G_e^I(\boldsymbol{\rho}, \boldsymbol{\rho}') \frac{\partial E_z(\boldsymbol{\rho})}{\partial n} \right) d\Gamma^I \end{aligned} \tag{4.7}$$

where $\Gamma^I + \Gamma_\infty^I$ is the contour enclosing Ω_∞^I. Since both E_z and G_e^I satisfy Sommerfeld radiation condition at infinity, integration over Γ_∞^I (see Fig. 4.2) in the right hand side of Eq. (4.7) vanishes (see Eq. (A.7)). Notice that G_e^I is zero on Γ^I (see Eq. (4.6)). Additionally, $E_z(\boldsymbol{\rho})$ is zero over the PEC ground plane except on hole aperture. Upon interchanging primed and unprimed coordinates, the Eq. (4.7) can be simplified to

$$E_z(\boldsymbol{\rho}) = -j\omega\mu_r \int_{\Omega_\infty^I} J_z(\boldsymbol{\rho}') G_e^I(\boldsymbol{\rho}, \boldsymbol{\rho}') d\Omega^I - \int_{\Gamma_B^I} E_z(\boldsymbol{\rho}') \frac{\partial G_e^I(\boldsymbol{\rho}, \boldsymbol{\rho}')}{\partial n'} d\Gamma^I. \tag{4.8}$$

Equation (4.8) can be interpreted as Eq. (2.13) where the first term of the right hand side represents the incident field, and the reflected field from the PEC screen, respectively. The second term of Eq. (4.8) represents the field perturbation due to the aperture of hole. In other words, the total electric field at each point in the upper half-space is the sum of the incident field, reflected field due to the PEC surface and the scattered field due to the aperture of the hole as

$$E_z(\boldsymbol{\rho}) = E_z^{inc}(\boldsymbol{\rho}) + E_z^{ref}(\boldsymbol{\rho}) - \int_{\Gamma_B^I} E_z(\boldsymbol{\rho}') \frac{\partial G_e^I(\boldsymbol{\rho}, \boldsymbol{\rho}')}{\partial n'} d\Gamma^I. \tag{4.9}$$

Referring to Fig. 4.1, let $\boldsymbol{\rho}$ and $\boldsymbol{\rho}'$ be designated the position of nodes on Γ_O^I and Γ_B^I, respectively. Therefore the incident and the reflected fields can be written as

$$\begin{aligned} E_z^{inc}(\boldsymbol{\rho}) &= \exp\left(-jk_0(x\sin\theta - y\cos\theta)\right) \\ E_z^{ref}(\boldsymbol{\rho}) &= -\exp\left(-jk_0(x\sin\theta + y\cos\theta)\right) \end{aligned} \tag{4.10}$$

where x and y are Cartesian components of $\boldsymbol{\rho}$. To calculate the last term in Eq. (4.9), the aperture, Γ_B^I, is discretized into n segments with length of $\Delta x'$. By expanding $E_z(\boldsymbol{\rho}')$ over Γ_B^I in terms of piecewise linear interpolating functions as

$$E_z(\boldsymbol{\rho}') = \sum_{j=1}^{n} E_{zj}(x_j', y_j') \sum_{k=1}^{2} \psi_{jk}(x_j') \tag{4.11}$$

where x' and y' are cartesian components of $\boldsymbol{\rho}'$ and

$$\psi_{jk}(x_j') = \begin{cases} \frac{x_j'}{\Delta x'}, & k{=}1; \\ 1 - \frac{x_j'}{\Delta x'}, & k{=}2. \end{cases} \tag{4.12}$$

Equation (4.9) can be represented in matrix notation as

$$\left[u_{o^I}\right] = \left[T^I\right] + \left[S^I\right]\left[u_{b^I}\right] \tag{4.13}$$

where the elements of $[u_{o^I}]$, $[u_{b^I}]$, and $[T^I]$ matrices represent $E_z(x,y)$, $E_z(x',y')$, and $\left(E_z^{inc}(x,y) + E_z^{ref}(x,y)\right)$, respectively, at each node. Noting that $d\Gamma^I = dx'$ and $\hat{n'} = -\hat{y'}$, the elements of $[S^I]$ are defined as

$$S_{ij}^I = \int_{x_j'-\Delta x'}^{x_j'} \psi_{j1}(x_j') \left.\frac{\partial G_e^I(x_i, y, x_j', y')}{\partial y'}\right|_{y'=0} dx' + \int_{x_j'}^{x_j'+\Delta x'} \psi_{j2}(x_j') \left.\frac{\partial G_e^I(x_i, y, x_j', y')}{\partial y'}\right|_{y'=0} dx' \tag{4.14}$$

where

$$\left.\frac{\partial G_e^I(x_i, y, x_j', y')}{\partial y'}\right|_{y'=0} = \frac{-jk_0 y}{2\sqrt{(x_i - x_j')^2 + y^2}} H_1^{(2)}\left(k_0\sqrt{(x_i - x_j')^2 + y^2}\right). \tag{4.15}$$

Equation (4.13) represents the boundary constraint on the aperture of the hole in the region I.

4.2.2 Lower Half-Space (Region II)

Let us consider the domain Ω_∞^{II} representing the half-space below the PEC slab (see Fig. 4.2). In the source-free region Ω_∞^{II} and for the TM$_z$ polarization case, the transmitted electric field vector has only a z-component satisfying the homogenous Helmholtz's equation:

$$\nabla^2 E_z(\boldsymbol{\rho}) + {k_0}^2 E_z(\boldsymbol{\rho}) = 0, \qquad \boldsymbol{\rho} \in \Omega_\infty^{II}. \tag{4.16}$$

Let us introduce the Green's function $G_e^{II}(\boldsymbol{\rho}, \boldsymbol{\rho}')$ governed by Helmholtz's equation

$$\nabla^2 G_e^{II}(\boldsymbol{\rho}, \boldsymbol{\rho}') + {k_0}^2 G_e^{II}(\boldsymbol{\rho}, \boldsymbol{\rho}') = -\delta(\boldsymbol{\rho} - \boldsymbol{\rho}') \qquad \boldsymbol{\rho}, \boldsymbol{\rho}' \in \Omega_\infty^{II}. \tag{4.17}$$

Equation (4.17) is similar to the Eq. (4.5) but the main difference is in the location of the unit source. In Eq. (4.5) the unit source is located on Γ_o^I whereas in Eq. (4.17) unit source is assumed to be located on Γ_o^{II}. $G_e^{II}(\boldsymbol{\rho}, \boldsymbol{\rho}')$ satisfies the boundary condition $G_e^{II}(\boldsymbol{\rho}, \boldsymbol{\rho}')\big|_{y=-t_s} = 0$ where t_s is the thickness of the PEC slab (i.e., $G_e^{II} = 0$ on Γ^{II}) and Sommerfeld radiation condition at infinity. $G_e^{II}(\boldsymbol{\rho}, \boldsymbol{\rho}')$ is found to be the zeroth-order Hankel function of the second kind as Eq. (4.6). The surface integral equation (Eq. (A.6)) in the source-free region Ω_∞^{II} for the TM$_z$ polarization, can then be expressed as

$$E_z(\boldsymbol{\rho}') = -\oint_{\Gamma^{II}+\Gamma_\infty^{II}} \left(E_z(\boldsymbol{\rho}) \frac{\partial G_e^{II}(\boldsymbol{\rho}, \boldsymbol{\rho}')}{\partial n} - G_e^{II}(\boldsymbol{\rho}, \boldsymbol{\rho}') \frac{\partial E_z(\boldsymbol{\rho})}{\partial n} \right) d\Gamma^{II} \tag{4.18}$$

where $\Gamma^{II} + \Gamma_\infty^{II}$ is the contour enclosing Ω_∞^{II} in counter-clockwise direction. Since both E_z and G_e^{II} satisfy Sommerfeld radiation condition at infinity, integration over Γ_∞^{II} (see Fig. 4.2) in the right hand side of Eq. (4.18) vanishes (see Eq. (A.7)). Notice that G_e^{II} is zero on Γ^{II}. Additionally, $E_z(\boldsymbol{\rho})$ is zero over the PEC ground plane except at aperture of hole. Upon interchanging primed and unprimed coordinates, the Eq. (4.18) can be simplified to

$$E_z(\boldsymbol{\rho}) = -\int_{\Gamma_B^{II}} E_z(\boldsymbol{\rho}') \frac{\partial G_e^{II}(\boldsymbol{\rho}, \boldsymbol{\rho}')}{\partial n'} d\Gamma^{II}. \tag{4.19}$$

Equation (4.19), represents the transmitted field from the aperture of the hole into the region II. To calculate Eq. (4.19), the aperture, Γ_B^{II}, is discretized into n segments with length of $\Delta x'$ in the same manner as the upper half-space. Also, $E_z(\boldsymbol{\rho}')$ is expanded over Γ_B^{II} in terms of piecewise linear interpolating functions as Eq. (4.11) where the interpolating function is defined as Eq. (4.12). Also, it is noticeable that the normal vector $\hat{n'}$ is in direction of $\hat{y'}$. Therefore, Eq. (4.19) can be represented in matrix notation as

$$\left[u_{o^{II}}\right] = -\left[S^{II}\right]\left[u_{b^{II}}\right] \tag{4.20}$$

where the elements of $[u_{o^{II}}]$ matrix represent $E_z(\boldsymbol{\rho})$ at each node. The elements of $[S^{II}]$ are defined as

$$
\begin{aligned}
S_{ij}^{II} = &\int_{x'_j-\Delta x'}^{x'_j} \psi_{j1}(x'_j)\, \left.\frac{\partial G_e^{II}(x_i, y, x'_j, y')}{\partial y'}\right|_{y'=-t_s} dx' + \\
&\int_{x'_j}^{x'_j+\Delta x'} \psi_{j2}(x'_j)\, \left.\frac{\partial G_e^{II}(x_i, y, x'_j, y')}{\partial y'}\right|_{y'=-t_s} dx'
\end{aligned}
\tag{4.21}
$$

where

$$
\left.\frac{\partial G_e^{II}(x_i, y, x'_j, y')}{\partial y'}\right|_{y'=-t_s} = \frac{-jk_0(y+t_s)}{2\sqrt{(x_i-x'_j)^2+(y+t_s)^2}} H_1^{(2)}\left(k_0\sqrt{(x_i-x'_j)^2+(y+t_s)^2}\right). \tag{4.22}
$$

Equation (4.20) represents the boundary constraint on the aperture of the hole in the region II.

4.2.3 Modified Finite-Element System Matrix for TM$_\mathrm{z}$ Polarization

Equations (4.13) and (4.20) represent the boundary constraint on the hole opening. Combining these equations and Eq. (4.3) in matrix form results in

$$
\begin{bmatrix} M_{ii} & M_{ib^I} & M_{ib^{II}} \\ M_{b^Ii} & M_{b^Ib^I} + M_{b^Io^I}S^I & 0 \\ M_{b^{II}i} & 0 & M_{b^{II}b^{II}} - M_{b^{II}o^{II}}S^{II} \end{bmatrix} \begin{bmatrix} u_i \\ u_{b^I} \\ u_{b^{II}} \end{bmatrix} = \begin{bmatrix} F_i \\ F_{b^I} - M_{b^Io^I}T^I \\ F_{b^{II}} \end{bmatrix}. \tag{4.23}
$$

Equation (4.23) represents the modified system matrix which can be solved using commonly used methods for solving linear systems.

4.3 Surface Integral Equation for TE$_\mathrm{z}$ Polarization

In this section, the surface integral equation in region I and II using Green's function of second kind for the TE$_z$ polarization will be derived.

4.3.1 Upper Half-Space (Region I)

To derive the surface integral equation for the TE$_z$ polarization case, the electric current filament is replaced with a magnetic current filament M_z. In Ω_∞^I and for the TE$_z$ polarization case, the magnetic field vector has only a z-component satisfying Helmholtz's equation

$$\nabla^2 H_z(\boldsymbol{\rho}) + {k_0}^2 H_z(\boldsymbol{\rho}) = j\omega\varepsilon_r M_z(\boldsymbol{\rho}), \qquad \boldsymbol{\rho} \in \ \Omega_\infty^I \tag{4.24}$$

where $\boldsymbol{\rho}$ and Ω_∞^I have the same definition as the section 4.2.1 (see Fig. 4.2). Let us introduce the Green's function $G_h^I(\boldsymbol{\rho}, \boldsymbol{\rho}')$ which is the solution due to the magnetic current filament located at $\boldsymbol{\rho}'$ and governed by Helmholtz's equation

$$\nabla^2 G_h^I(\boldsymbol{\rho}, \boldsymbol{\rho}') + {k_0}^2 G_h^I(\boldsymbol{\rho}, \boldsymbol{\rho}') = -\delta(\boldsymbol{\rho} - \boldsymbol{\rho}'), \qquad \boldsymbol{\rho}, \boldsymbol{\rho}' \in \Omega_\infty^I. \tag{4.25}$$

Since the image of the magnetic current in the vicinity of the PEC surface is in the same direction of the original current, therefore $G_h^I(\boldsymbol{\rho}, \boldsymbol{\rho}')|_{y=0} \neq 0$ on the ground plane. In this case, boundary condition on the PEC surface can be represented by

$$\left.\frac{\partial G_h^I(\boldsymbol{\rho}, \boldsymbol{\rho}')}{\partial y'}\right|_{y=0} = 0. \tag{4.26}$$

In addition, $G_h^I(\boldsymbol{\rho}, \boldsymbol{\rho}')$ satisfies Sommerfeld radiation condition at infinity. Therefore $G_h^I(\boldsymbol{\rho}, \boldsymbol{\rho}')$ can be represented in terms of the zeroth-order Hankel function of the second kind as

$$G_h^I(\boldsymbol{\rho}, \boldsymbol{\rho}') = -\frac{j}{4} H_0^{(2)}(k_0|\boldsymbol{\rho} - \boldsymbol{\rho}'_{\mathrm{s}}|) - \frac{j}{4} H_0^{(2)}(k_0|\boldsymbol{\rho} - \boldsymbol{\rho}'_{\mathrm{i}}|) \tag{4.27}$$

where $\boldsymbol{\rho}'_{\mathrm{s}}$, and $\boldsymbol{\rho}'_{\mathrm{i}}$ represent the position of the source current, and its image, respectively. The surface integral equation (Eq. (A.6)) in region I for the TE$_z$ polarization, then can be written as

$$\begin{aligned} H_z(\boldsymbol{\rho}') = &- j\omega\varepsilon_r \int_{\Omega_\infty^I} M_z(\boldsymbol{\rho}) G_h^I(\boldsymbol{\rho}, \boldsymbol{\rho}') d\Omega^I \\ &- \oint_{\Gamma^I + \Gamma_\infty^I} \left(H_z(\boldsymbol{\rho}) \frac{\partial G_h^I(\boldsymbol{\rho}, \boldsymbol{\rho}')}{\partial n} - G_h^I(\boldsymbol{\rho}, \boldsymbol{\rho}') \frac{\partial H_z(\boldsymbol{\rho})}{\partial n} \right) d\Gamma^I. \end{aligned} \tag{4.28}$$

Both $H_z(\boldsymbol{\rho})$ and $G_h^I(\boldsymbol{\rho}, \boldsymbol{\rho}')$ satisfy Sommerfeld radiation condition at infinity, therefore integration over Γ_∞^I (see Fig. 4.2) in the right hand side of Eq. (4.28) vanishes (see Eq. (A.7)). Notice that $\partial H_z(\boldsymbol{\rho})/\partial n$ is zero over the PEC ground plane except on the aperture of hole and $\partial G_h^I(\boldsymbol{\rho}, \boldsymbol{\rho}')/\partial n$ is zero on the Γ^I (see Eq. (4.26)). Upon interchanging primed and unprimed coordinates, the Eq. (4.28) reduces to

$$H_z(\boldsymbol{\rho}) = -j\omega\varepsilon_r \int_{\Omega_\infty^I} M_z(\boldsymbol{\rho}') G_h^I(\boldsymbol{\rho}, \boldsymbol{\rho}') d\Omega^I + \int_{\Gamma_B^I} G_h^I(\boldsymbol{\rho}, \boldsymbol{\rho}') \frac{\partial H_z(\boldsymbol{\rho}')}{\partial n'} d\Gamma^I. \tag{4.29}$$

Similar to the TM$_z$ case, the first term in the right hand side of Eq. (4.29) represents the magnetic field generated by the magnetic current filament and its image in the vicinity of the PEC ground plane. These fields can be interpreted as an incident field and a reflected field from the PEC screen. The second term in Eq. (4.29) represents field perturbation due to the aperture of the hole. Then Eq. (4.29) can be rewritten as

$$H_z(\boldsymbol{\rho}) = H_z^{inc}(\boldsymbol{\rho}) + H_z^{ref}(\boldsymbol{\rho}) + \int_{\Gamma_B^I} G_h^I(\boldsymbol{\rho}, \boldsymbol{\rho}') \frac{\partial H_z(\boldsymbol{\rho}')}{\partial n'} d\Gamma^I. \tag{4.30}$$

By the same definition of $\boldsymbol{\rho}$ and $\boldsymbol{\rho}'$ as in section 4.2.1, and assuming the coordinate system as in Fig. 4.1, the incident and reflected waves can be written as

$$\begin{aligned} H_z^{inc}(\boldsymbol{\rho}) &= \exp(-jk_0(x\sin\theta - y\cos\theta)) \\ H_z^{ref}(\boldsymbol{\rho}) &= \exp(-jk_0(x\sin\theta + y\cos\theta)). \end{aligned} \tag{4.31}$$

To calculate the last term in Eq. (4.30), the partial derivative $\partial H_z(\boldsymbol{\rho}')/\partial n'$ can be expressed as a first-order finite difference as

$$\frac{\partial H_z(\boldsymbol{\rho}')}{\partial n'} = -\frac{H_z(x = x', y) - H_z(x', y')}{y - y'} \tag{4.32}$$

(notice that the negative sign on the right hand side of Eq. (4.32) is because $\hat{n'} = -\hat{y'}$),then the aperture Γ_B^I, and Γ_O^I are discretized into n segments with length of $\Delta x'$. By expanding both $H_z(x = x', y)$ and $H_z(x', y')$ over the aperture of the hole in terms of step functions as

$$H_z = \sum_{j=1}^{n} H_{zj}\psi_j(x'_j) \tag{4.33}$$

where

$$\psi_j(x'_j) = \begin{cases} 1, & x'_j - \frac{\Delta x'_j}{2} < x'_j < x'_j + \frac{\Delta x'_j}{2}; \\ 0, & \text{elsewhere.} \end{cases} \tag{4.34}$$

the singular behavior of the fields at the edges of the hole can be avoided. By replacing the field expansions in Eq. (4.30) and defining the elements of matrix $[S^I]$ as

$$S_{ij}^I = \int_{x'_j - \Delta x'_j/2}^{x'_j + \Delta x'_j/2} \frac{G_h^I(x_i, y, x'_j, y' = 0)\psi_j(x'_j)}{y - y'} dx' \tag{4.35}$$

where

$$G_h^I(x_i, y, x'_j, y' = 0) = -\frac{j}{2} H_0^{(2)}\left(k_0\sqrt{(x_i - x'_j)^2 + y^2}\right). \tag{4.36}$$

Equation (4.30) can be represented in the matrix form as

$$\left[u_{o^I}\right] = \left[T^I\right] - \left[S^I\right]\left\{\left[u_{o^I}\right] - \left[u_{b^I}\right]\right\}. \tag{4.37}$$

In Eq. (4.37), the elements of $[u_{o^I}]$, $[u_{b^I}]$, and $[T^I]$ matrices represent $H_z(x, y)$, $H_z(x', y')$, and $\left(H_z^{inc}(x, y) + H_z^{ref}(x, y)\right)$, respectively, at each node. Equation (4.37) can be rearranged as

$$\left[u_{o^I}\right] = \left\{\left[I\right] + \left[S^I\right]\right\}^{-1}\left[T^I\right] + \left\{\left[I\right] + \left[S^I\right]\right\}^{-1}\left[S^I\right]\left[u_{b^I}\right] \tag{4.38}$$

where $[I]$ is the unity matrix. Equation (4.38) represents the boundary constraint on the hole opening into the region I.

4.3.2 Lower Half-Space (Region II)

Let us consider the domain Ω_∞^{II} representing the half-space below the PEC slab (see Fig. 4.2). In the source-free region Ω_∞^{II} and for the TE$_z$ polarization case, the transmitted magnetic field vector has only a z-component satisfying the homogenous Helmholtz's equation:

$$\nabla^2 H_z(\boldsymbol{\rho}) + {k_0}^2 H_z(\boldsymbol{\rho}) = 0, \qquad \boldsymbol{\rho} \in \Omega_\infty^{II}. \tag{4.39}$$

Let us introduce the Green's function $G_h^{II}(\boldsymbol{\rho}, \boldsymbol{\rho}')$ governed by Helmholtz's equation

$$\nabla^2 G_h^{II}(\boldsymbol{\rho}, \boldsymbol{\rho}') + {k_0}^2 G_h^{II}(\boldsymbol{\rho}, \boldsymbol{\rho}') = -\delta(\boldsymbol{\rho} - \boldsymbol{\rho}') \qquad \boldsymbol{\rho}, \boldsymbol{\rho}' \in \Omega_\infty^{II}. \tag{4.40}$$

Equation (4.40) differs from Eq. (4.25) in the location of the unit source. In Eq. (4.25) the unit source is located on Γ_o^I whereas in Eq. (4.40) unit source is assumed to be located on Γ_o^{II}. $G_h^{II}(\boldsymbol{\rho}, \boldsymbol{\rho}')$ satisfies Sommerfeld radiation condition at infinity and the boundary condition as

$$\left.\frac{\partial G_h^{II}(\boldsymbol{\rho}, \boldsymbol{\rho}')}{\partial y'}\right|_{y=-t_s} = 0 \tag{4.41}$$

where t_s is the thickness of the PEC slab. $G_h^{II}(\boldsymbol{\rho}, \boldsymbol{\rho}')$ is found to be the zeroth-order Hankel function of the second kind as Eq. (4.27). The surface integral equation (Eq. (A.6)) in region II for the TE$_z$ polarization, then can be written as

$$H_z(\boldsymbol{\rho}') = -\oint_{\Gamma^{II}+\Gamma_\infty^{II}} \left(H_z(\boldsymbol{\rho}) \frac{\partial G_h^{II}(\boldsymbol{\rho}, \boldsymbol{\rho}')}{\partial n} - G_h^{II}(\boldsymbol{\rho}, \boldsymbol{\rho}') \frac{\partial H_z(\boldsymbol{\rho})}{\partial n} \right) d\Gamma^{II} \tag{4.42}$$

where $\Gamma^{II} + \Gamma_\infty^{II}$ is the contour enclosing Ω_∞^{II} in counter-clockwise direction. Since both H_z and G_h^{II} satisfy Sommerfeld radiation condition at infinity, integration over Γ_∞^{II} (see Fig. 4.2) in the right hand side of Eq. (4.42) vanishes (see Eq. (A.7)). Notice that $\partial G_h^{II}(\boldsymbol{\rho}, \boldsymbol{\rho}')/\partial n$ is zero on Γ^{II}. Additionally, $\partial H_z(\boldsymbol{\rho})/\partial n$ is zero over the PEC ground plane except on the aperture of the hole. Upon interchanging primed and unprimed coordinates, Eq. (4.42) can be simplified to

$$H_z(\boldsymbol{\rho}) = \int_{\Gamma_B^{II}} G_h^{II}(\boldsymbol{\rho}, \boldsymbol{\rho}') \frac{\partial H_z(\boldsymbol{\rho}')}{\partial n'} d\Gamma^{II}. \tag{4.43}$$

Equation (4.43) represents the transmitted field from the aperture of the hole into the region II. Upon using (x', y') and (x, y) as Cartesian components of $\boldsymbol{\rho}'$ and $\boldsymbol{\rho}$, respectively, and expressing the partial derivative as a first-order finite difference, Eq. (4.43) can be written as

$$H_z(\boldsymbol{\rho}) = \int_{\Gamma_B^{II}} G_h^{II}(\boldsymbol{\rho}, \boldsymbol{\rho}') \left(\frac{H_z(x = x', y) - H_z(x', y')}{y - y'} \right) dx'. \tag{4.44}$$

To calculate the integral in Eq. (4.44), the aperture Γ_B^{II} and Γ_O^{II} are discretized into n segments with length of $\Delta x'$. Both $H_z(x = x', y)$ and $H_z(x', y')$ are expanded as Eq. (4.33) over the hole aperture in terms of step functions as Eq. (4.34). By replacing the field expansions in Eq. (4.44) and defining of elements of matrix $[S^{II}]$ as

$$S_{ij}^{II} = \int_{x_j' - \Delta x_j'/2}^{x_j' + \Delta x_j'/2} \frac{G_h^{II}(x_i, y, x_j', y' = -t_s)\psi_j(x_j')}{y - y'} dx' \tag{4.45}$$

where

$$G_h^{II}(x_i, y, x_j', y' = -t_s) = -\frac{j}{2} H_0^{(2)} \left(k_0 \sqrt{(x_i - x_j')^2 + (y + t_s)^2} \right) \tag{4.46}$$

Eq. (4.44) can be represented in the matrix form as

$$\left[u_{o^{II}}\right] = \left[S^{II}\right] \left\{ \left[u_{o^{II}}\right] - \left[u_{b^{II}}\right] \right\}. \tag{4.47}$$

In Eq. (4.47), the elements of $[u_{o^{II}}]$, and $[u_{b^{II}}]$ matrices represent $H_z(x, y)$ and $H_z(x', y')$, respectively, at each node. Equation (4.47) can be rearranged as

$$\left[u_{o^{II}}\right] = -\left\{ \left[I\right] - \left[S^{II}\right] \right\}^{-1} \left[S^{II}\right] \left[u_{b^{II}}\right]. \tag{4.48}$$

Equation (4.48) represents the boundary constraint on the hole opening into the region II.

4.3.3 Modified Finite-Element System Matrix for TE$_z$ Polarization

Equations (4.38) and (4.48) represent the boundary constraints on the hole openings. Combining these equations and Eq. (4.3) in matrix form results in

$$\begin{bmatrix} M_{ii} & M_{ib^I} & M_{ib^{II}} \\ M_{b^I i} & M_{b^I b^I} + M_{b^I o^I}(I + S^I)^{-1} S^I & 0 \\ M_{b^{II} i} & 0 & -M_{b^{II} o^{II}}(I - S^{II})^{-1} S^{II} \end{bmatrix} \begin{bmatrix} u_i \\ u_{b^I} \\ u_{b^{II}} \end{bmatrix} = \begin{bmatrix} F_i \\ F_{b^I} - M_{b^I o^I}(I + S^I)^{-1} T^I \\ F_{b^{II}} \end{bmatrix}. \tag{4.49}$$

Equation (4.49) represents the modified system matrix which can be solved using commonly used methods for solving linear systems.

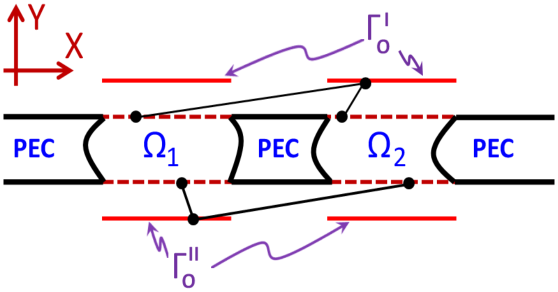

Figure 4.3: Schematic showing the extension of the surface integral method to multiple holes.

4.4 Extension to Multiple Holes with Side Grating

In this section, the method developed above is extended to the problem of scattering from multiple holes in a PEC surface. A schematic representing the scattering problem for two holes is shown in Fig. 4.3. The region inside the holes are labeled as Ω_1 and Ω_2. Extending the finite element development in section 4.1 to two holes, the system matrix for the domains Ω_1 and Ω_2 is generalized as

$$\begin{aligned}[M]^{(1)}[u]^{(1)} &= [F]^{(1)} \\ [M]^{(2)}[u]^{(2)} &= [F]^{(2)}\end{aligned} \tag{4.50}$$

where each system of equation can be represented symbolically as Eq. (4.3). Assembling the two systems using global numbering of nodes gives

$$\begin{bmatrix}[M]^{(1)} & 0 \\ 0 & [M]^{(2)}\end{bmatrix}\begin{bmatrix}[u]^{(1)} \\ [u]^{(2)}\end{bmatrix} = \begin{bmatrix}[F]^{(1)} \\ [F]^{(2)}\end{bmatrix}. \tag{4.51}$$

The two system matrices arising from each of the two holes will be coupled through the surface integral equation in the following manner. In region I, each node on Γ_O^I is connected via the Green's function to all the nodes on the aperture of the two holes, Γ_B^I, via Eq. (4.9) and Eq. (4.30) for the TM$_z$ and TE$_z$ polarization, respectively (see Fig. 4.3). Also, in region II, each node on Γ_O^{II} is connected via the Green's function to all the nodes on the aperture of the two holes, Γ_B^{II}, via Eq. (4.19) and Eq. (4.43) for the TM$_z$ and TE$_z$ polarization, respectively. In other words, the holes are coupled to each other *only* through the surface integral equation and Green's function in each region. In the set of equations (4.9) and (4.30), or the set of equations (4.19) and (4.43), the integration is performed over the apertures of all holes in region I or region II, respectively. For instance, Eq. (4.13) and Eq. (4.20) for the TM$_z$ polarization can be represented symbolically in matrix form as

$$\begin{bmatrix}[u_{o^I}]^{(1)} \\ [u_{o^I}]^{(2)}\end{bmatrix} = \begin{bmatrix}[T^I]^{(1)} \\ [T^I]^{(2)}\end{bmatrix} + \begin{bmatrix}[S^I]^{(11)} & [S^I]^{(12)} \\ [S^I]^{(21)} & [S^I]^{(22)}\end{bmatrix}\begin{bmatrix}[u_{b^I}]^{(1)} \\ [u_{b^I}]^{(2)}\end{bmatrix} \tag{4.52}$$

and

$$\begin{bmatrix}[u_{o^{II}}]^{(1)}\\ [u_{o^{II}}]^{(2)}\end{bmatrix} = -\begin{bmatrix}[S^{II}]^{(11)} & [S^{II}]^{(12)}\\ [S^{II}]^{(21)} & [S^{II}]^{(22)}\end{bmatrix}\begin{bmatrix}[u_{b^{II}}]^{(1)}\\ [u_{b^{II}}]^{(2)}\end{bmatrix}, \tag{4.53}$$

respectively, where $[S]^{(ij)}$, represents connectivity between nodes on Γ_O of the i_{th} hole $[u_o]^{(i)}$ and nodes on Γ_B of the j_{th} hole $[u_b]^{(j)}$ via the surface integral equation (i & $j = 1, 2$) in both region I and II. Combining Eq. (4.51), Eq. (4.52) and Eq. (4.53) in matrix form results in the modified system matrix as

$$\begin{bmatrix}[M']^{(1)} & [C]^{(12)}\\ [C]^{(21)} & [M']^{(2)}\end{bmatrix}\begin{bmatrix}[u']^{(1)}\\ [u']^{(2)}\end{bmatrix} = \begin{bmatrix}[F']^{(1)}\\ [F']^{(2)}\end{bmatrix} \tag{4.54}$$

where $[C]^{(12)}$ and $[C]^{(21)}$ are matrices representing the coupling between the two holes, and are given by

$$\begin{aligned}[C]^{(12)} &= \begin{bmatrix}0 & 0 & 0\\ 0 & [M_{b^Io^I}]^{(1)}[S^I]^{(12)} & 0\\ 0 & 0 & -[M_{b^{II}o^{II}}]^{(1)}[S^{II}]^{(12)}\end{bmatrix}\\ [C]^{(21)} &= \begin{bmatrix}0 & 0 & 0\\ 0 & [M_{b^Io^I}]^{(2)}[S^I]^{(21)} & 0\\ 0 & 0 & -[M_{b^{II}o^{II}}]^{(2)}[S^{II}]^{(21)}\end{bmatrix}\end{aligned} \tag{4.55}$$

and $[M']$ and $[F']$ are given by

$$\begin{aligned}[M']^{(1)} &= \begin{bmatrix}[M_{ii}]^{(1)} & [M_{ib^I}]^{(1)} & [M_{ib^{II}}]^{(1)}\\ [M_{b^Ii}]^{(1)} & [M_{b^Ib^I}]^{(1)} + [M_{b^Io^I}]^{(1)}[S^I]^{(11)} & 0\\ [M_{b^{II}i}]^{(1)} & 0 & [M_{b^{II}b^{II}}]^{(1)} - [M_{b^{II}o^{II}}]^{(1)}[S^{II}]^{(11)}\end{bmatrix}\\ [M']^{(2)} &= \begin{bmatrix}[M_{ii}]^{(2)} & [M_{ib^I}]^{(2)} & [M_{ib^{II}}]^{(2)}\\ [M_{b^Ii}]^{(2)} & [M_{b^Ib^I}]^{(2)} + [M_{b^Io^I}]^{(2)}[S^I]^{(22)} & 0\\ [M_{b^{II}i}]^{(2)} & 0 & [M_{b^{II}b^{II}}]^{(2)} - [M_{b^{II}o^{II}}]^{(2)}[S^{II}]^{(22)}\end{bmatrix}\\ [F']^{(1)} &= \begin{bmatrix}[F_i]^{(1)}\\ [F_{b^I}]^{(1)} - [M_{b^Io^I}]^{(1)}[T^I]^{(1)}\\ [F_{b^{II}}]^{(1)}\end{bmatrix}\\ [F']^{(2)} &= \begin{bmatrix}[F_i]^{(2)}\\ [F_{b^I}]^{(2)} - [M_{b^Io^I}]^{(2)}[T^I]^{(2)}\\ [F_{b^{II}}]^{(2)}\end{bmatrix}\end{aligned} \tag{4.56}$$

and $[u']^{(k)}$ is given by

$$[u']^{(k)} = \begin{bmatrix}[u_i]^{(k)}\\ [u_{b^I}]^{(k)}\\ [u_{b^{II}}]^{(k)}\end{bmatrix} \qquad (k = 1 \;\&\; 2) \tag{4.57}$$

Notice that these coupling matrices are not necessarily identical. The same procedure is applicable to the TE$_z$ polarization. Generalizing the formulation to N holes results in the following system matrix:

$$\begin{bmatrix} [M']^{(1)} & [C]^{(12)} & \dots & [C]^{(1N)} \\ [C]^{(21)} & [M']^{(2)} & \dots & [C]^{(2N)} \\ \vdots & & \ddots & \vdots \\ [C]^{(N1)} & [C]^{(N2)} & \dots & [M']^{(N)} \end{bmatrix} \begin{bmatrix} [u']^{(1)} \\ [u']^{(2)} \\ \vdots \\ [u']^{(N)} \end{bmatrix} = \begin{bmatrix} [F']^{(1)} \\ [F']^{(2)} \\ \vdots \\ [F']^{(N)} \end{bmatrix}. \tag{4.58}$$

Once the nodal field values on Γ_O are expressed in terms of the nodal field values on Γ_B at each region, the modified system of equations can be solved using commonly used methods for solving linear systems.

The formulation presented in this chapter is applicable to holes with side cavities present in perfectly conducting surfaces. For multiple holes and cavities, Eq. (4.58) gives a mathematical quantification of the coupling factors between the holes and cavities. Physically, it is expected that the holes and cavities to be coupled through surface currents existing on the segments connecting the holes and cavities, as that is the only mechanism for energy transfer between them. This mechanism is discussed in section 2.5.2.

4.5 Numerical Results

Once the system of equations, Eq. (4.23) for the TM$_z$ polarization or Eq. (4.49) for the TE$_z$ polarization, is derived, its solution (which gives the field values at the apertures of the holes) can be obtained using commonly used methods for solving linear systems. In this section, examples of single and multiple holes with side gratings with different dimensions and fillings are provided to validate the algorithm developed in this chapter.

To validate the method presented here, comparison was made to the results obtained by commercial two-dimensional finite-element simulator COMSOL [43]. While using finite-element simulator for the comparison purpose, the absorbing boundary condition (ABC) was applied on the artificial boundary to truncate the computational domain (see Fig. 4.4). Throughout this work, these solutions is referred as (COMSOL). Without loss of generality, the magnitude of the incident electric field is assumed to be unity throughout this work. To implement the algorithm developed in this chapter, a nodal based finite element formulation is used. the solution domain is discretized using first-order triangle elements with a mesh density of approximately 20 nodes per λ for the TM$_z$ case. Since there is a discontinuity in the electric field at the edges of the holes or cavities as the side gratings in the TE$_z$ case, mesh density of 100 nodes per λ is used. Throughout this work, the solution obtained using the method presented in this chapter is referred to as "Total Field Surface Integral Equation" (TFSIE).

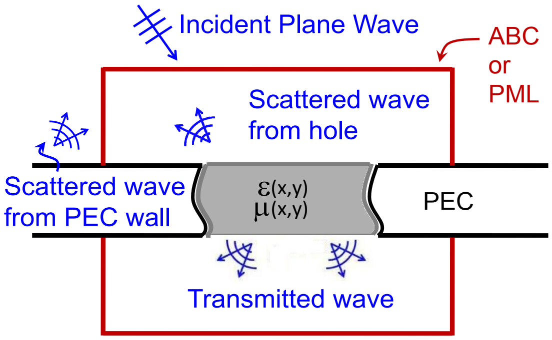

Figure 4.4: Schematic of the computational domain truncation using ABC or PML in solving the scattering problem from a hole with arbitrary shape in an infinite PEC surface.

4.5.1 Single Hole Case

In the first example, a $0.8\lambda \times 0.5\lambda$ (width×depth) rectangular hole is considered where λ is the wavelength in free space. Figures 4.5 and 4.6 show the total electric field for the TM_z polarization and total magnetic fields for the TE_z polarization of incident plane waves, at the both apertures of the hole, for an oblique incident angle. The results in Fig. 4.5 and Fig. 4.6 show strong agreement between the calculations using TFSIE and those obtained

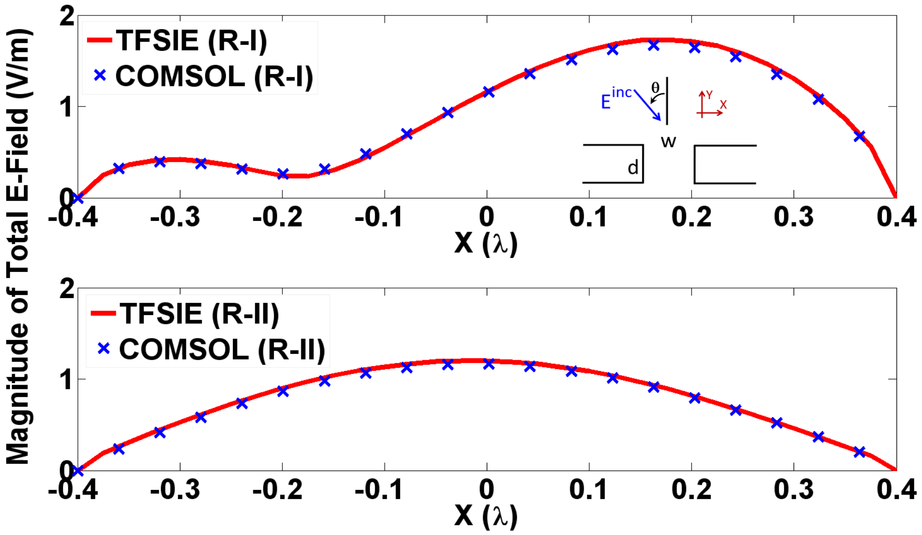

Figure 4.5: Amplitude of total E-field at the hole openings into the region I (R-I) and the region II (R-II) for a $0.8\lambda \times 0.5\lambda$ air-filled rectangular hole, TM_z case, $\theta = 30°$, calculated using the method introduced in this work (TFSIE), and COMSOL.

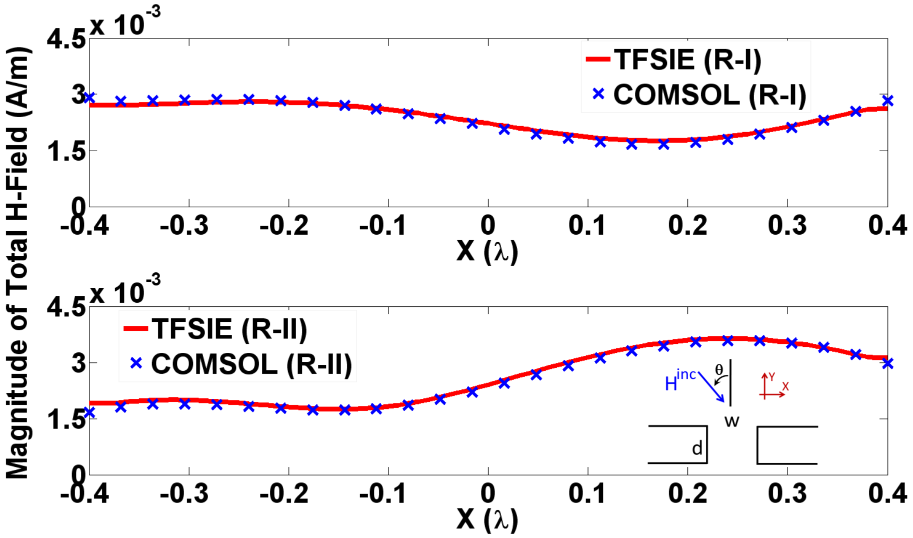

Figure 4.6: Amplitude of total H-field at the hole openings into the region I (R-I) and the region II (R-II) for a $0.8\lambda \times 0.5\lambda$ air-filled rectangular hole, TE$_z$ case, $\theta = 30°$, calculated using the method introduced in this work (TFSIE), and COMSOL.

using COMSOL.

As the next example of a single hole case, a $0.7\lambda \times 0.35\lambda$ rectangular hole shown in Fig. 4.7 is considered. The hole is filled with silicon having a relative permittivity of $\epsilon_r = 11.9$ and including a $0.42\lambda \times 0.07\lambda$ PEC strip positioned at the geometric center of the hole. Good agreement is observed between the results calculated using TFSIE and those obtained by COMSOL. This numerical example shows the versatility of the TFSIE to solve the problem of scattering from the holes with complex structures and fillings.

4.5.2 Multiple Holes

Five identical $0.4\lambda \times 0.2\lambda$ rectangular holes separated by 0.4λ are considered as an example of scattering problem from multiple holes. Figures 4.8 and 4.9 show the total electric field for the TM$_z$ polarization and total magnetic field for the TE$_z$ polarization, respectively, at the aperture of the five holes, for oblique incidence. Close agreement between TFSIE and COMSOL is observed.

In Fig. 4.10 and Fig. 4.11 the total electric, and magnetic fields in the far region in the lower half-space (region II) for an array of five holes are presented, respectively. The far-field can be calculated using the equivalence principle. By closing the apertures by a PEC surface and introducing an equivalent magnetic current $\boldsymbol{M}(x', y')$ at the aperture into

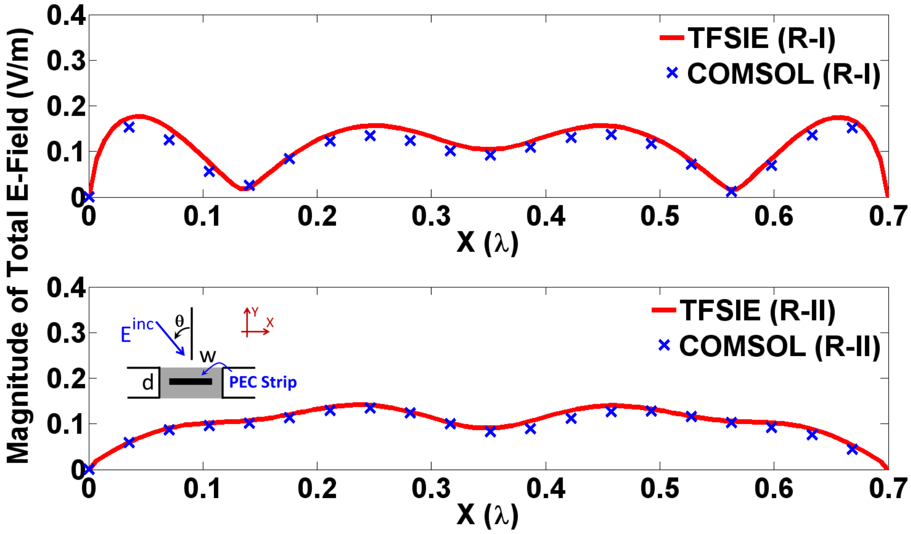

Figure 4.7: Amplitude of total E-field at the hole openings into the region I (R-I) and the region II (R-II) for a $0.7\lambda \times 0.35\lambda$ silicon-filled ($\varepsilon_r = 11.9$) rectangular hole, TM$_z$ case, $\theta = 30°$, calculated using the method introduced in this work (TFSIE), and COMSOL. The $0.42\lambda \times 0.07\lambda$ PEC strip is positioned at the geometric center of the hole.

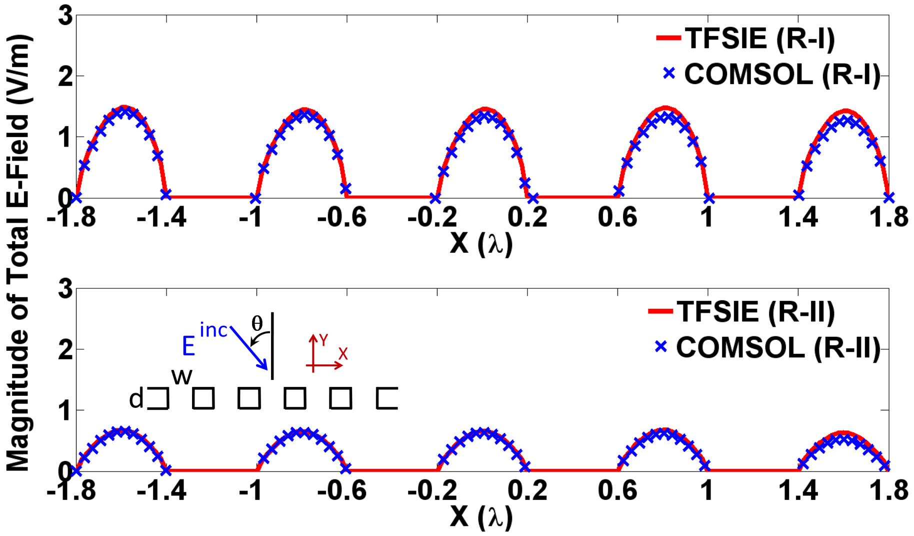

Figure 4.8: Amplitude of total E-field at the holes openings into the region I (R-I) and the region II (R-II) for five identical $0.4\lambda \times 0.2\lambda$ air-filled rectangular holes, TM$_z$ case, $\theta = 30°$, calculated using the method introduced in this work (TFSIE), and COMSOL. The holes are separated by 0.4λ.

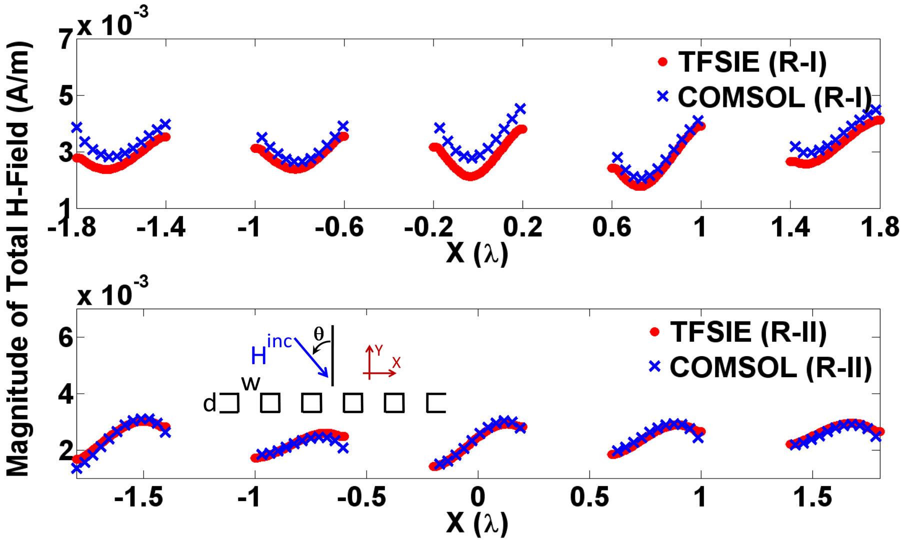

Figure 4.9: Amplitude of total H-field at the holes openings into the region I (R-I) and the region II (R-II) for five identical $0.4\lambda \times 0.2\lambda$ air-filled rectangular holes, TE$_z$ case, $\theta = 30°$, calculated using the method introduced in this work (TFSIE), and COMSOL. The holes are separated by 0.4λ.

the region II, the transmitted electric field in the far region can be represented as

$$\boldsymbol{E}(x,y) = -2\boldsymbol{\nabla} \times \int_{\Gamma_B^{II}} \boldsymbol{M}(x',y')G(x,y,x',y')dx' \tag{4.59}$$

where $\boldsymbol{M}(x',y') = -\hat{n} \times \boldsymbol{E}(x',y')|_{y'=-t_s}$ and $G(x,y,x',y')$ is the free-space Green's function

$$G(x,y,x',y') = -\frac{j}{4}H_0^{(2)}(k_0R) \tag{4.60}$$

where $R = ((x-x')^2 + (y+t_s)^2)^{\frac{1}{2}}$. For the TM$_z$ case where the electric field has only a z-component, Eq. (4.59) can be written as

$$\boldsymbol{E}(x,y) = -\hat{z}\int_{\Gamma_B^{II}} 2E_z(x',y')|_{y'=-t_s}\frac{\partial G}{\partial y}dx'. \tag{4.61}$$

For the TE$_z$ case where the magnetic field has only a z-component, the electric field at the aperture has two components. Therefore Eq. (4.59) can be written as

$$\boldsymbol{E}(x,y) = \frac{-2}{j\omega\varepsilon_r}\left(\hat{x}\int_{\Gamma_B^{II}} \frac{\partial H_z(x',y')}{\partial y'}|_{y'=-t_s}\frac{\partial G}{\partial y}dx' - \hat{y}\int_{\Gamma_B^{II}} \frac{\partial H_z(x',y')}{\partial y'}|_{y'=-t_s}\frac{\partial G}{\partial x}dx'\right). \tag{4.62}$$

Figure 4.10 shows far electric field for TM$_z$-polarized normal incident and Fig. 4.11 shows far magnetic field and TE$_z$-polarized oblique incident.

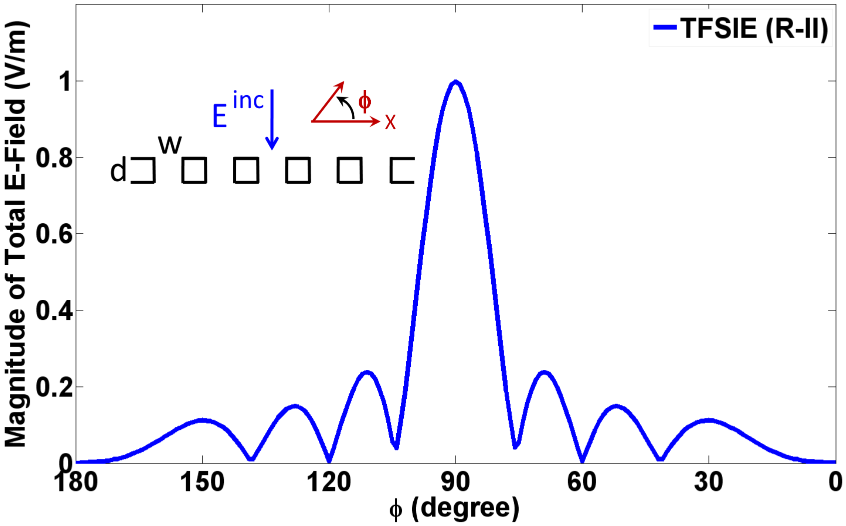

Figure 4.10: Amplitude of total E-field in the far region II (R-II) for five identical $0.4\lambda \times 0.2\lambda$ air-filled rectangular holes, TM_z case, normal incident, calculated using the method introduced in this work (TFSIE). The holes are separated by 0.4λ.

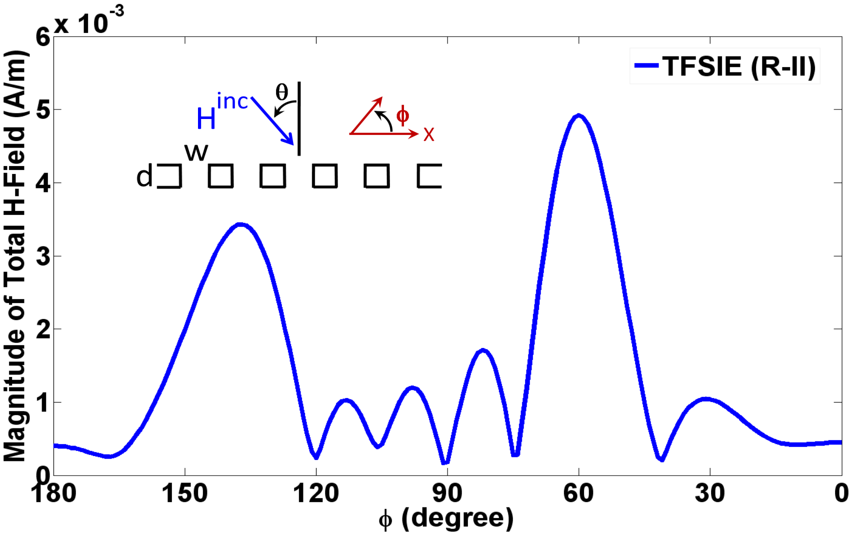

Figure 4.11: Amplitude of total H-field in the far region II (R-II) for five identical $0.4\lambda \times 0.2\lambda$ air-filled rectangular holes, TE_z case, $\theta = 30°$, calculated using the method introduced in this work (TFSIE). The holes are separated by 0.4λ.

4.5.3 Single Hole with Side Grating

In this section, a single $0.5\lambda \times 0.8\lambda$ rectangular hole and three $0.5\lambda \times 0.3\lambda$ cavities as a side grating in the PEC slab is considered (see inset of Fig. 4.12). The hole and cavities are separated by 0.5λ. Both sides of the PEC slab have an identical grating. The analysis of this structure is very important due to study of the extraordinary transmission of light.

Figure 4.12 shows the total electric field at the apertures of the hole and side cavities for oblique incident plane waves. Close agreement between TFSIE and COMSOL is observed despite a deviation between the results calculated using TFSIE and those obtained by COMSOL for the farthest cavities from the hole in the region II. The cavities in region II are coupled to the incident wave in region I via the guided waves passing through the hole. Therefore, by increasing the distance between the cavities and the hole, the field amplitude at the aperture of the cavities is expected to decrease. However, Fig. 4.12 shows that in the case of COMSOL by increasing the distance between the cavities and the hole, the field amplitude at the aperture of the cavities increases. This increment in field amplitude is due to the non-physical reflections from the truncating boundary while using the ABC in the case of COMSOL. On the other hand, the results calculated using TFSIE clearly show decrement of the field amplitude as the distance between the cavities and the hole increases. Figure 4.13 shows the calculated field values in logarithmic scale in region II

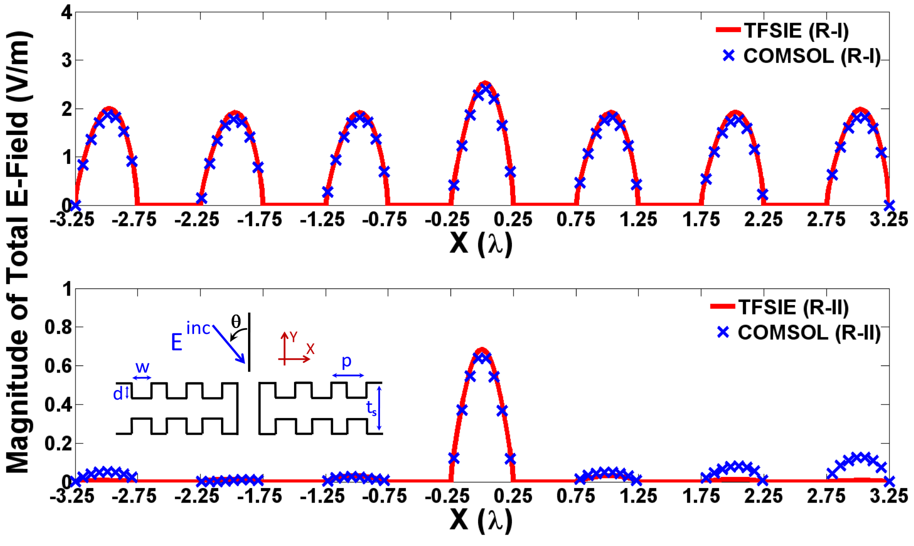

Figure 4.12: Amplitude of total E-field at the openings into the region I (R-I) and the region II (R-II) for a single $0.5\lambda \times 0.8\lambda$ hole with three identical $0.5\lambda \times 0.3\lambda$ air-filled rectangular side cavities, TM$_z$ case, $\theta = 30°$, calculated using the method introduced in this work (TFSIE), and COMSOL. The hole and the cavities are separated by 0.5λ.

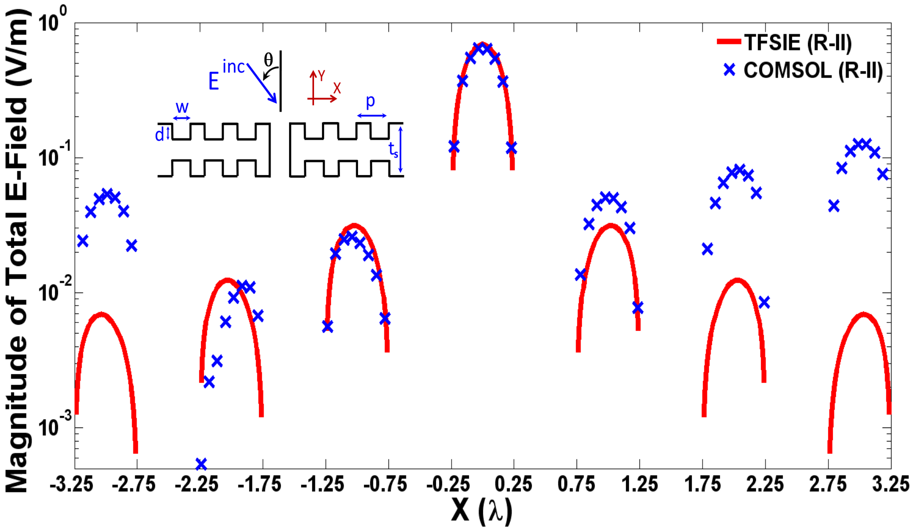

Figure 4.13: Amplitude of total E-field in region II (R-II) of Fig. 4.12 in logarithmic scale, calculated using the method introduced in this work (TFSIE), and COMSOL.

of Fig. 4.12. In case of COMSOL, the required computational domain was approximately $159\lambda^2$ while the TFSIE solution domain was confined to the hole and cavities area of $2.2\lambda^2$. This efficiency in computational resources leads to further studies of plasmonic resonance due to grating surfaces.

Figure 4.14 shows the total magnetic field at the apertures of the hole and side cavities for an oblique incident plane waves. For the TE_z polarization, the same deviation in region II between results calculated TFSIE and those obtained using COMSOL is observed. The cavities in region II are coupled to the incident wave in region I via the guided waves passing through the hole. These guided waves are excited by interaction of incident field with grating surface in region I which in turn excite the surface current on the PEC segments in region II. Since the surface currents or in other words, evanescent waves can not be modeled properly by an ABC or PML is placed close to the aperture [51], it is necessary to choose an ABC or PML far enough from the aperture in the commercial solver to achieve accurate results. In contrast, the surface integral equation can model the evanescent waves as well as propagation waves.

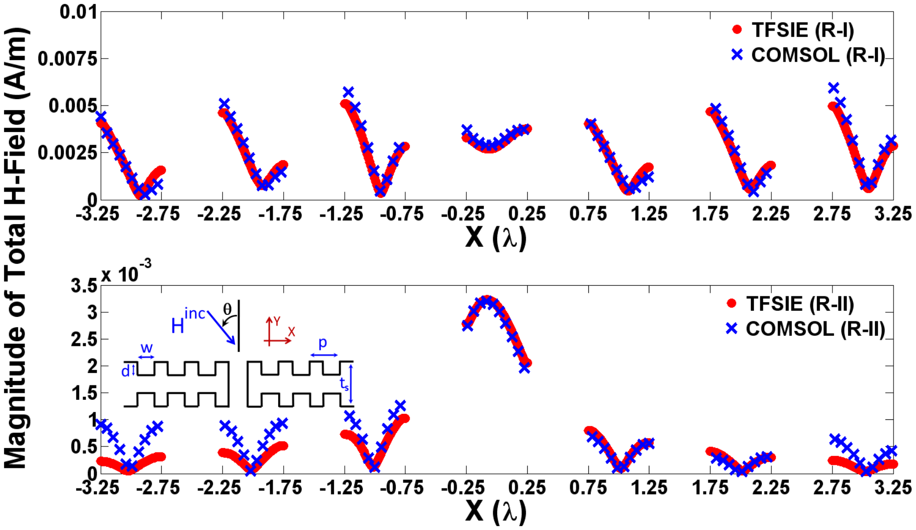

Figure 4.14: Amplitude of total H-field at the openings into the region I (R-I) and the region II (R-II) for a single $0.5\lambda \times 0.8\lambda$ hole with three identical $0.5\lambda \times 0.3\lambda$ air-filled rectangular side cavities, TE$_z$ case, $\theta = 30°$, calculated using the method introduced in this work (TFSIE), and COMSOL. The hole and the cavities are separated by 0.5λ.

Chapter 5

Scattering from an Infinite Periodic Array of Cavities in a Conducting Screens

In this chapter, a new algorithm is developed to solve the problem of scattering from an infinite periodic array of identical cavities engraved in an infinite perfect electric conductor screen. Using the two-boundary formulation which was used in previous chapters, the solution domain is confined to *only* one cavity which is divided into interior and exterior regions. The finite-element formulation is applied inside the interior regions to obtain the solution of Helmholtz's equation. The surface integral equation using the half-space Green's function, is applied at the openings of all cavities as a global boundary condition. Taking advantage of the field's periodicity at the apertures of the cavities, the half-space Green's function is replaced by the quasi-periodic Green's function, thus limiting the surface integral equation to the aperture of *only* one cavity. The Neumann or Dirichlet boundary condition is applied on the PEC walls of the cavity for the TE or TM polarization, respectively. The advantage of this method is that no periodic boundary condition, which would require a constrained mesh scheme, is used in this formulation. Also, it is emphasized that in the method presented here, the surface integral equation using the quasi-periodic Green's function is used to derive a linear system of equation as a constraint which connects the field values on the boundary to the field values on the apertures of the single cavity in the array by considering the coupling between all cavities. The attractive feature of two-boundary formulation combined with quasi-periodic Green's function is that no singularities in Green's function arises while applying the surface integral as a boundary constraint.

5.1 Finite-Element Formulation of the Problem

Figure 5.1 shows a 2-D perfectly conducting screen containing infinite periodic identical cavities illuminated by an obliquely incident plane wave. The periodicity and width of the aperture of the cavities are denoted by P and W, respectively. u^{inc}, and u^{s} denote the incident field, and scattered field from the aperture of the cavities, respectively, along the axis of the cavities. The infinite periodic array of cavities can be divided into unit-cells. The width of each unit-cell equals the periodicity of the array. The unit-cells are indexed by m where $m = -\infty \cdots, -1, 0, 1, \cdots \infty$.

Figure 5.2 shows three successive unit-cells as part of an infinite array of cavities. For a cavity in each unit-cell (i.e., the m^{th} unit-cell), Γ_B is defined to be the contour at the opening of the cavity, and Γ_O as the top contour in close vicinity of Γ_B such that the region between Γ_B and Γ_O is devoid of field nodes. Also let Ω_{in}^{m} denote the interior region of the m^{th} cavity bounded by the PEC surface of the cavity and Γ_O. Next, the solution domain Ω_{in}^{m} is discretized into triangular elements. Notice that, however, rectangular or other types of elements can be used without affecting the theoretical development presented here. The unknown total field u^t over each element is described by a set of interpolating functions given by

$$u^t = \sum_{i=1}^{N} {u_i}^t \alpha_i(x, y) \tag{5.1}$$

where N is the number of nodes in each element at which the unknown field is defined, and $\alpha_i(x, y)$ is an interpolation function. The finite element formulation is used inside each

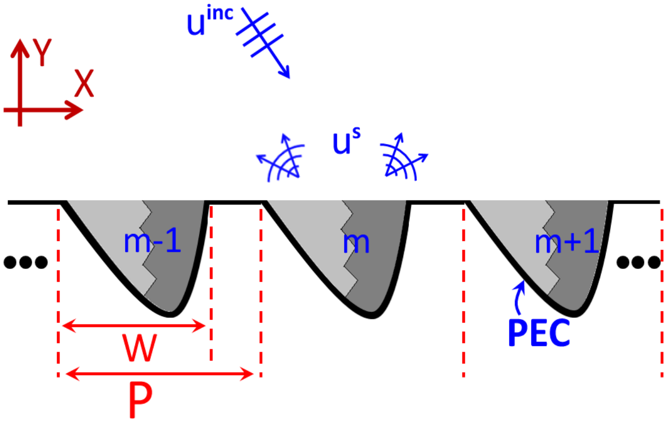

Figure 5.1: Schematic of the scattering problem from an infinite periodic array of cavities with arbitrary shape engraved in a conducting surface.

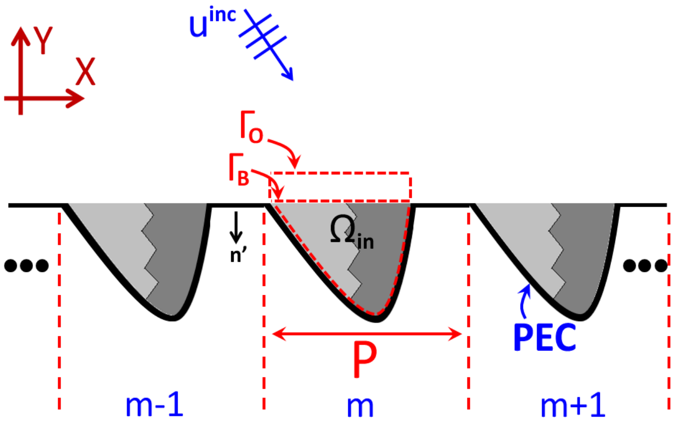

Figure 5.2: Schematic of an unit-cell of an infinite periodic array of cavities engraved in a conducting surface.

element of Ω_{in}^m to obtain the weak form of Helmholtz's equation:

$$\boldsymbol{\nabla}\cdot\left(\frac{1}{p(x,y)}\boldsymbol{\nabla}u^t\right)+{k_0}^2q(x,y)u^t=0 \tag{5.2}$$

where u^t, $p(x,y)$, $q(x,y)$, and k_0 have the same definitions as in section 2.1. The time harmonic factor $\exp(j\omega t)$ is assumed and suppressed throughout. Following the procedure in section 2.1, the Galerkin-weighted residual integral R^e for each element inside m^{th} unit-cell can be expressed in matrix form as

$$R^e=\left[M^e\right]^m\left[u^e\right]^m-\left[F^e\right]^m=0 \tag{5.3}$$

where $[u^e]^m$ represents the unknown field value at each node of the e^{th} element inside m^{th} cavity. The $[F^e]^m$ matrix represents impressed sources at each node; therefore, for the problem of scattering from cavities considered in this chapter, $[F^e]^m$ is zero. The elements of $N\times N$ matrix $[M^e]^m$ are given by

$$\begin{aligned}\left(M_{ij}^e\right)^m=&\int_{\Omega^e}\left(\frac{1}{p(x,y)}\boldsymbol{\nabla}\alpha_i(x,y)\cdot\boldsymbol{\nabla}\alpha_j(x,y)-{k_0}^2q(x,y)\alpha_i(x,y)\alpha_j(x,y)\right)d\Omega\\&+\oint_{\Gamma^e}\frac{\alpha_i(x,y)}{p(x,y)}\boldsymbol{\nabla}\alpha_j(x,y)\cdot d\boldsymbol{\Gamma}.\end{aligned} \tag{5.4}$$

By assembling all local system matrices Eq. (5.3) the global system matrix for the m^{th} cavity can be represented symbolically as

$$\begin{bmatrix}M_{ii} & M_{ib} & 0\\ M_{bi} & M_{bb} & M_{bo}\\ 0 & M_{ob} & M_{oo}\end{bmatrix}^m\begin{bmatrix}u_i\\ u_b\\ u_o\end{bmatrix}^m=\begin{bmatrix}F_i\\ F_b\\ F_o\end{bmatrix}^m \tag{5.5}$$

where u_i, u_b and u_o represent nodal field values inside the cavity, on Γ_B, and on Γ_O, respectively. Extending the formulation to all cavities, $\Omega_{in}^{-\infty} \cdots \Omega_{in}^{\infty}$, we have the following system of matrix equations:

$$
\begin{gathered}
[M]^{-\infty}[u]^{-\infty} = [F]^{-\infty} \\
\vdots \\
[M]^{0}[u]^{0} = [F]^{0} \\
\vdots \\
[M]^{\infty}[u]^{\infty} = [F]^{\infty}
\end{gathered}
\tag{5.6}
$$

where each matrix equation in the system in Eq. (5.6) can be represented symbolically as Eq. (5.5).

The systems of equations in Eq. (5.6) are coupled to each other *only* through the surface integral equation. It is impossible to solve all systems of equations in Eq. (5.6) simultaneously. In the next section, an algorithm that solves the problem of an array of infinite cavities is developed by considering *only* one system of equations corresponding to a single cavity while incorporating the effect of all other cavities. This will be accomplished by making use of the quasi-periodic Green's function in conjunction with the surface integral equation. More specifically, the linear system of equations in Eq. (5.5) represents the relationship between the nodal field values for the m^{th} cavity without any external constraint represented by the infinite array of cavities and the incident plane wave. The imposition of a specific excitation represented by the incident plane wave has to be taken into consideration through a boundary constraint that establishes a relationship between the incident field, the boundary nodes and the interior nodes.

5.2 Surface Integral Equation

The surface integral equation using the half-space Green's function will first be used to express the nodal field values on Γ_O of each cavity in terms of the nodal field values on Γ_B of all cavities (see Fig. 5.3). Next, we develop an algorithm to limit the surface integral equation to the aperture of one cavity by replacing the half-space Green's function by the quasi-periodic Green's function that takes into account the effect of all cavities.

5.2.1 Surface Integral Equation for TM$_z$ Polarization

For TM$_z$ polarization where the electric field vector is parallel to the axis of the cavities, the surface integral equation (see Eqs. (A.6), (2.14)) is expressed as

$$
E_z(\boldsymbol{\rho}) = E_z^{inc}(\boldsymbol{\rho}) + E_z^{ref}(\boldsymbol{\rho}) - \sum_{m=-\infty}^{\infty} \int_{\Gamma_B^m} E_z(\boldsymbol{\rho}') \frac{\partial G^e(\boldsymbol{\rho}, \boldsymbol{\rho}')}{\partial n'} d\Gamma \tag{5.7}
$$

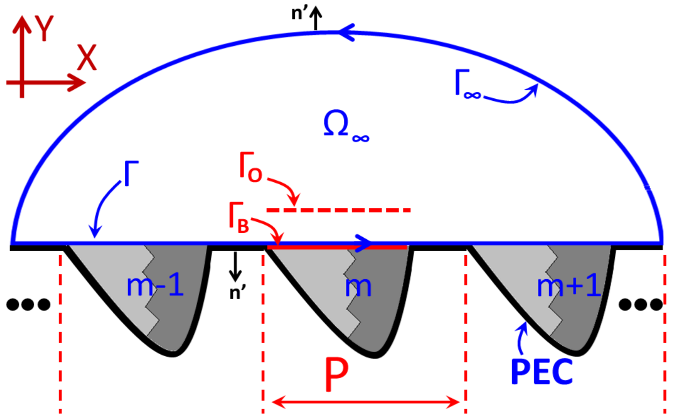

Figure 5.3: Schematic of the surface integral contour in the half-space above the cavities.

where $\boldsymbol{\rho}$ and $\boldsymbol{\rho}'$ represent the position of the nodes on Γ_O and Γ_B , respectively. Note that the integration is performed only at the aperture of the cavities Γ_B^m. $E_z(\boldsymbol{\rho})$ on the left-hand side of the Eq. (5.7) represents the total field value at any point in upper half-space above the cavities. Also $E_z^{inc}(\boldsymbol{\rho})$ and $E_z^{ref}(\boldsymbol{\rho})$ on the right-hand side represent the incident field and the reflected field by the PEC screen, respectively. The last term in Eq. (5.7) represents the scattered field due to aperture of the cavities. In Eq. (5.7), $G^e(\boldsymbol{\rho}, \boldsymbol{\rho}')$ is the Green's function of the first kind satisfying the boundary condition $G^e(\boldsymbol{\rho}, \boldsymbol{\rho}')_{|y=0} = 0$ (i.e., $G^e = 0$ on Γ) and Sommerfeld radiation condition at infinity. $G^e(\boldsymbol{\rho}, \boldsymbol{\rho}')$ is found to be the zeroth-order Hankel function of the second kind:

$$G^e(\boldsymbol{\rho}, \boldsymbol{\rho}') = -\frac{j}{4} H_0^{(2)}(k_0 |\boldsymbol{\rho} - \boldsymbol{\rho}'_{\mathrm{s}}|) + \frac{j}{4} H_0^{(2)}(k_0 |\boldsymbol{\rho} - \boldsymbol{\rho}'_{\mathrm{i}}|) \tag{5.8}$$

where $\boldsymbol{\rho}'_{\mathrm{s}}$, and $\boldsymbol{\rho}'_{\mathrm{i}}$ represent the position of the source current, and its image, respectively. In Eq. (5.7), each node on Γ_O is connected via the surface integral equation to the all nodes on the aperture of all cavities, Γ_B, (see Fig. 5.3). In other words, the cavities are coupled to each other *only* through the surface integral equation.

To calculate the last term in Eq. (5.7), the aperture, Γ_B of each cavity, and Γ_O are discretized into J segments with length of $\Delta x'$. Then $E_z(\boldsymbol{\rho}')$ is expanded over Γ_B in terms of piecewise linear interpolating functions as

$$E_z(\boldsymbol{\rho}') = \sum_{j=1}^{J} E_{zj}(x'_j, y'_j)\psi_j(x'_j) \tag{5.9}$$

where x' and y' are Cartesian components of $\boldsymbol{\rho}'$. Equation (5.7) can be represented in discrete notation as

$${u_{o_i}}^n = T_i^n + \sum_{m=-\infty}^{\infty} \sum_{j=1}^{J} \left(\int \psi_j({x'_j}^m) \, \frac{\partial}{\partial y'} G^e \left({x_i}^n, {y_i}^n, {x'_j}^m, {y'_j}^m \right) dx' \right) {u_{b_j}}^m \tag{5.10}$$

where ${u_{o_i}}^n$ and T_i^n represent $E_z(\boldsymbol{\rho})$, and $(E_z^{inc}(\boldsymbol{\rho}) + E_z^{ref}(\boldsymbol{\rho}))$, respectively, at the i^{th} node on the Γ_O of the n^{th} cavity. Also the ${u_{b_j}}^m$ represents $E_{zj}(\boldsymbol{\rho'})$ at the j^{th} node on the Γ_B of the m^{th} cavity. It is noticeable that in Eq. (5.10), integration is performed on the j^{th} segment of the Γ_B of the m^{th} cavity.

Physically, the cavities are indistinguishable in structure, therefore similar distribution of the field magnitude at the apertures of all cavities is expected. Now, let assume similar discretization of Γ_B of all cavities. This assumption does not pose any limitation on the generality and versatility of this method but helps to simplify the algorithm by using the Floquet theorem. In practice a mesh is created and the formulation is applied on one cavity. By similar discretization of the Γ_B of all cavities and same local numbering of the nodes, the total field value at two nodes with same position with respect to the edge of the cavities (i.e., the j^{th} nodes of the m^{th} and n^{th} cavities) are related as

$$
{u_{b_j}}^m = {u_{b_j}}^n e^{-j(m-n)k_{0\parallel}P} \tag{5.11}
$$

where $k_{0\parallel} = k_0 \sin\theta$ and P is periodicity of the array. Note that the coordinates of such nodes are related as

$$
\begin{aligned}
{x'_j}^m &= {x'_j}^n + (m-n)P \\
{y'_j}^m &= {y'_j}^n.
\end{aligned} \tag{5.12}
$$

Without loss of generality, n is chosen as zero for a cavity located at the origin and the superscript n is suppressed throughout. Inserting Eq. (5.11) and Eq. (5.12) into Eq. (5.10), results in

$$
u_{o_i} = T_i + \sum_{m=-\infty}^{\infty} \sum_{j=1}^{J} \left(\int \psi_j(x'_j + mP) \; \frac{\partial}{\partial y'} G^e\left(x_i, y_i, x'_j + mP, y'_j\right) dx' \right) u_{b_j} e^{-jmk_{0\parallel}P}. \tag{5.13}
$$

Note that since the mesh scheme is assumed to be identical for all cavities, the interpolating function $\psi_j(x'_j + mP)$ is the same as $\psi_j(x'_j)$. Changing the order of the summations and integral, Eq. (5.13) can be rewritten as

$$
u_{o_i} = T_i + \sum_{j=1}^{J} \left(\int \psi_j(x'_j) \; \frac{\partial}{\partial y'} \left(\sum_{m=-\infty}^{\infty} e^{-jmk_{0\parallel}P} G^e(x_i, y_i, x'_j + mP, y'_j) \right) dx' \right) u_{b_j}. \tag{5.14}
$$

The quasi-periodic Green's function of the first kind (which is solution to an infinite periodic array of current sources with an uniform progressive phase shift in proximity of an infinite ground plane) is defined as

$$
G_Q^e(x_i, y_i, x'_j, y'_j) = \sum_{m=-\infty}^{\infty} e^{-jmk_{0\parallel}P} G^e(x_i, y_i, x'_j + mP, y'_j). \tag{5.15}
$$

By replacing the sum containing the half-space Green's function with the quasi-periodic Green's function as in Eq. (5.15), the surface integral equation is limited to the aperture of one cavity only. Equation (5.14) can be represented in matrix form as

$$\left[u_o\right] = \left[T\right] + \left[S\right]\left[u_b\right] \tag{5.16}$$

where the elements of $[S]$ are defined as

$$S_{ij} = \int_{j^{th}\ segment} \psi_j(x'_j)\frac{\partial}{\partial y'} G^e_Q\left(x_i, y_i, x'_j, y'_j\right) dx'. \tag{5.17}$$

Combining Eq. (5.16) and Eq. (5.5) in matrix form results in the modified system matrix for one cavity as

$$\begin{bmatrix} M_{ii} & M_{ib} \\ M_{bi} & M_{bb} + M_{bo}S \end{bmatrix} \begin{bmatrix} u_i \\ u_b \end{bmatrix} = \begin{bmatrix} F_i \\ F_b - M_{bo}T \end{bmatrix}. \tag{5.18}$$

5.2.2 Surface Integral Equation for $\mathrm{TE_z}$ Polarization

For the TE_z polarization where the magnetic field vector is parallel to the axis of the cavities, the surface integral equation (see Eqs. (A.6), (2.28)) is written as

$$H_z(\boldsymbol{\rho}) = H_z^{inc}(\boldsymbol{\rho}) + H_z^{ref}(\boldsymbol{\rho}) + \sum_{m=-\infty}^{\infty} \int_{\Gamma_B^m} G^h(\boldsymbol{\rho}, \boldsymbol{\rho}')\frac{\partial H_z(\boldsymbol{\rho}')}{\partial n'} d\Gamma. \tag{5.19}$$

The integration is performed at the aperture of all cavities Γ_B^m. Similar to the TM_z case, $H_z(\boldsymbol{\rho})$ on the left-hand side of the Eq. (5.19) represents the total field value at any point in the upper half-space above the cavities. Also $H_z^{inc}(\boldsymbol{\rho})$ and $H_z^{ref}(\boldsymbol{\rho})$ on the right-hand side represent the incident field and the reflected field by the PEC screen, respectively. The last term in Eq. (5.19) represents the scattered field due to the aperture of the cavities. In Eq.(5.19), $G^h(\boldsymbol{\rho}, \boldsymbol{\rho}')$ is Green's function of the second kind satisfying the boundary condition $\partial G^h(\boldsymbol{\rho}, \boldsymbol{\rho}')/\partial n'|_{y=0} = 0$ (i.e., $\partial G^h(\boldsymbol{\rho}, \boldsymbol{\rho}')/\partial n' = 0$ on Γ) and the Sommerfeld radiation condition at infinity. Therefore $G^h(\boldsymbol{\rho}, \boldsymbol{\rho}')$ can be represented in terms of the zeroth-order Hankel function of the second kind as

$$G^h(\boldsymbol{\rho}, \boldsymbol{\rho}') = -\frac{j}{4}H_0^{(2)}(k_0|\boldsymbol{\rho} - \boldsymbol{\rho}'_{\mathrm{s}}|) - \frac{j}{4}H_0^{(2)}(k_0|\boldsymbol{\rho} - \boldsymbol{\rho}'_{\mathrm{i}}|). \tag{5.20}$$

To calculate the last term in Eq. (5.19), the partial derivative $\partial H_z(\boldsymbol{\rho}')/\partial n'$ can be conveniently expressed as a first-order finite difference as

$$\frac{\partial H_z(\boldsymbol{\rho}')}{\partial n'} = -\frac{H_z(x = x', y) - H_z(x', y')}{y - y'} \tag{5.21}$$

(notice that the negative sign on the right hand side of Eq. (5.21) is because $\hat{n'} = -\hat{y'}$), then the apertures Γ_B, and Γ_O of each cavity are discretized into J segments with length $\Delta x'$. By expanding both $H_z(x = x', y)$ and $H_z(x', y')$ over the aperture of the cavity in terms of step functions as

$$H_z = \sum_{j=1}^{J} \psi_j(x'_j) H_{zj}, \tag{5.22}$$

Eq. (5.19) can be represented in discrete form as

$$u_{o_i}{}^n = T_i^n - \sum_{m=-\infty}^{\infty} \sum_{j=1}^{J} \left(\int G^h(x_i{}^n, y_i{}^n, x'_j{}^m, y'_j{}^m) \, \frac{\psi_j(x'_j{}^m)}{y_j{}^m - y'_j{}^m} dx' \right) \left(u_{o_j}{}^m - u_{b_j}{}^m \right). \tag{5.23}$$

In Eq. (5.23), $u_{o_i}{}^n$, and T_i^n represent $H_z(\boldsymbol{\rho})$, and $(H_z^{inc}(\boldsymbol{\rho}) + H_z^{ref}(\boldsymbol{\rho}))$, respectively, at the i^{th} node on the Γ_O of the n^{th} cavity. The $u_{o_j}{}^m$ and $u_{b_j}{}^m$ represent nodal field value at the j^{th} node on the Γ_O and Γ_B of the m^{th} cavity, respectively. Notice that in Eq. (5.23), the integration is performed on the j^{th} segment of the Γ_B of the m^{th} cavity.

By considering the fact that the cavities in the infinite array are identical, and assuming similar discretization of the Γ_B and Γ_O of the all cavities, the field values and coordinates of the two nodes with same position in two different cavities can be expressed through Eqs. (5.11) and (5.12). Similar to the TM$_z$ case, without loss of generality, n is chosen as zero for a cavity located at the origin and the superscript n is suppressed throughout. Replacing Eqs. (5.11) and (5.12) into Eq. (5.23), results

$$\begin{aligned} u_{o_i} = T_i - \\ \sum_{m=-\infty}^{\infty} \sum_{j=1}^{J} \left(\int G^h(x_i, y_i, x'_j + mP, y'_j) \, \frac{\psi_j(x'_j + mP)}{y_j - y'_j} dx' \right) (u_{o_j} \, e^{-jmk_{0\parallel}P} - u_{b_j} \, e^{-jmk_{0\parallel}P}). \end{aligned} \tag{5.24}$$

In Eq. (5.24), the interpolating function $\psi_j(x'_j + mP)$ can be replaced with $\psi_j(x'_j)$ since identical mesh scheme is assumed at the aperture of all cavities. By changing the order of summations and integral, Eq. (5.24) can be rewritten as

$$u_{o_i} = T_i - \sum_{j=1}^{J} \left(\int \left(\sum_{m=-\infty}^{\infty} e^{-jmk_{0\parallel}P} G^h(x_i, y_i, x'_j + mP, y'_j) \right) \frac{\psi_j(x'_j)}{y_j - y'_j} dx' \right) (u_{o_j} - u_{b_j}). \tag{5.25}$$

The quasi-periodic Green's function of the second kind (which is solution to an infinite periodic array of current sources with an uniform progressive phase shift in proximity of an infinite ground plane) is defined as

$$G_Q^h(x_i, y_i, x'_j, y'_j) = \sum_{m=-\infty}^{\infty} e^{-jmk_{0\parallel}P} G^h(x_i, y_i, x'_j + mP, y'_j). \tag{5.26}$$

Similar to the TM$_z$ case, by replacing the sum containing the half-space Green's function with the quasi-periodic Green's function, the surface integral equation is limited to the aperture of one cavity. Equation (5.25) can be represented in matrix form as

$$[u_o] = [T] - [S]\left\{[u_o] - [u_b]\right\} \tag{5.27}$$

where the elements of $[S]$ are defined as

$$S_{ij} = \int_{j^{th}\ segment} G_Q^h(x_i, y_i, x'_j, y'_j)\frac{\psi_j(x'_j)}{y_j - y'_j}dx'. \tag{5.28}$$

Equation (5.27) can be rearranged as

$$[u_o] = \left\{[I] + [S]\right\}^{-1}[T] + \left\{[I] + [S]\right\}^{-1}[S]\,[u_b] \tag{5.29}$$

where $[I]$ is unity matrix. Combining Eq. (5.29) and Eq. (5.5) in matrix form results in the modified system matrix for one cavity as

$$\begin{bmatrix} M_{ii} & M_{ib} \\ M_{bi} & M_{bb} + M_{bo}(I+S)^{-1}S \end{bmatrix}\begin{bmatrix} u_i \\ u_b \end{bmatrix} = \begin{bmatrix} F_i \\ F_b - M_{bo}(I+S)^{-1}T \end{bmatrix}. \tag{5.30}$$

5.3 Numerical Results

Once the system of equations, Eq. (5.18) for the TM$_z$ polarization or Eq. (5.30) for the TE$_z$ polarization, is derived, its solution (which is the field values at the aperture of the 0^{th} cavity) can be obtained using commonly used methods for solving linear systems. Using Eq. (5.11), the field values at the aperture of any cavity can be determined. Since structures having infinite periodic cavities are non-physical, the infinite periodicity is typically used to approximate an array with large number of cavities where the interest lies in determining the field distribution at the center of the array. In this section, examples of infinite array of cavities with different dimensions, periodicity, and fillings are provided.

To validate the method presented here, comparison was made to the results calculated by the finite-element method using local boundary conditions and the mode matching technique (MMT). While using the finite-element method for the comparison purpose, the solution region was bounded to a unit-cell and the periodic boundary condition (PBC) was applied at the lateral boundaries of the unit-cell. To truncate the computational domain above the unit-cell, either the second order Bayliss-Grunzburger-Turkel (BGT-II) boundary operator or the perfectly matched layer (PML) are employed. Throughout this section, these solutions are referred as (FEM-BGT-II), and (FEM-PML), respectively. Without loss of generality, the magnitude of the incident electric field is assumed to be unity throughout this work. To calculate the quasi-periodic Green's function in Eq. (5.15) for TM$_z$ polarization or Eq. (5.26) for TE$_z$ polarization, the infinite series is truncated such that containing 401 terms. The partial sum of the quasi-periodic Green's function is then calculated by direct summation. Note that using acceleration techniques such as Ewald's transformation increases the efficiency of the method. To apply FE formulation inside the cavity, the solution domain is discretized using first-order triangle elements with a mesh density of approximately 20 nodes per λ for the TM$_z$ case. Since there is a discontinuity in the electric field at the edges of the cavities in the TE$_z$ case, a mesh density of 100 nodes per λ is used. Throughout this section, the solution obtained using the method presented in this chapter is referred to as "Total Field Surface Integral Equation" (TFSIE).

In the first example, an infinite array of $0.6\lambda \times 0.4\lambda$ (width×depth) rectangular cavities is considered where λ is the wavelength in free space. The periodicity of the array is $P = 1\lambda$. The cavity is filled with material having relative permittivity of $\varepsilon_r = 1.4 - j0.01$. Figure 5.4 shows the total electric field at the aperture of the 0^{th} cavity for a TM$_z$ incident plane wave, for an obliquely incident angle of 30°. The results in Fig. 5.4 show strong agreement between the calculations using TFSIE and those calculated using FEM-BGT-II and FEM-PML. However, it is important to note that the necessary computational domain to achieve the accurate results in FEM-BGT-II and FEM-PML is $4\lambda^2$ and $1.2\lambda^2$, respec-

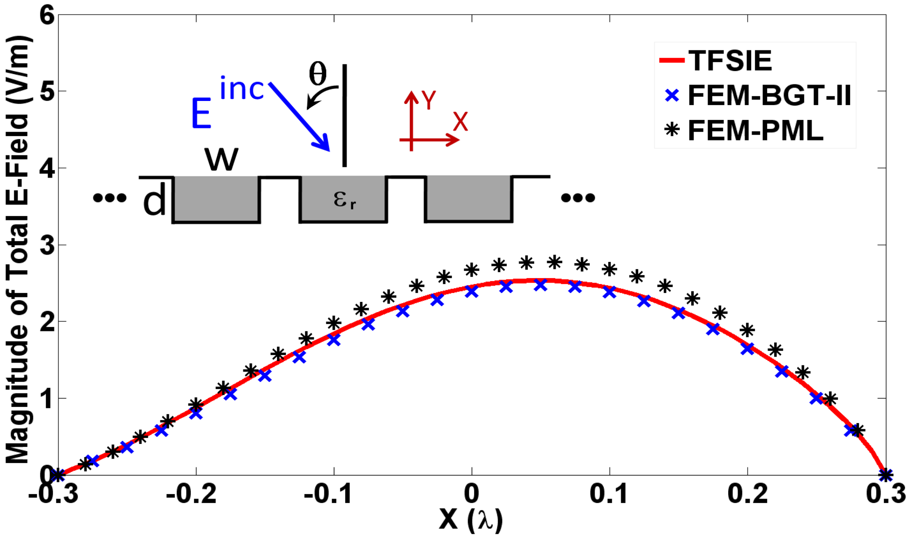

Figure 5.4: Amplitude of total E-field at the aperture of an infinite array of $0.6\lambda \times 0.4\lambda$ dielectric-filled ($\varepsilon_r = 1.4 - j0.01$) rectangular cavities, TM$_z$ case, $\theta = 30°$, calculated using TFSIE, the finite-element method using PBC and the second order BGT (FEM-BGT-II), and the finite-element method using PBC and PML (FEM-PML). The periodicity of the array is 1λ.

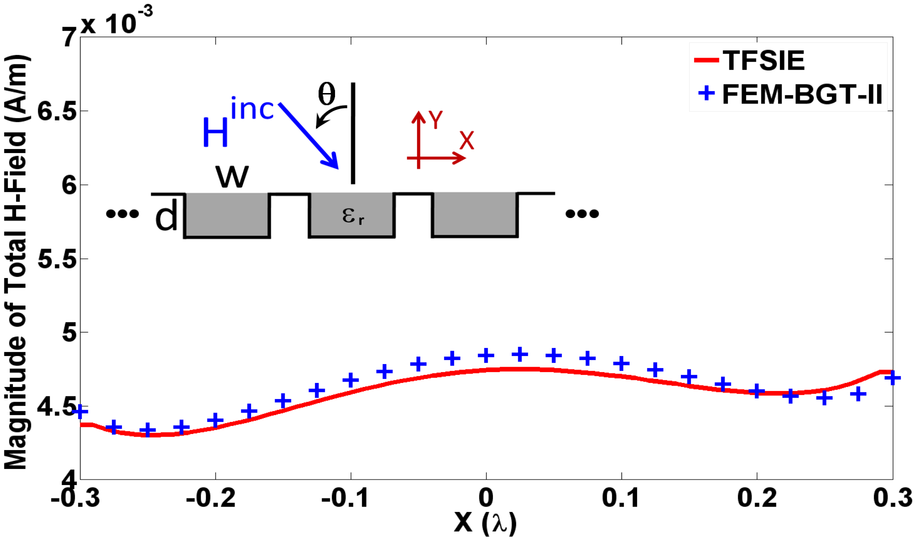

Figure 5.5: Amplitude of total H-field at the aperture of an infinite array of $0.6\lambda \times 0.4\lambda$ dielectric-filled ($\varepsilon_r = 1.4 - j0.01$) rectangular cavities, TE$_z$ case, $\theta = 30°$, calculated using TFSIE, and the finite-element method using PBC and the second order BGT (FEM-BGT-II). The periodicity of the array is 1λ.

tively. On the other hand, the solution region in TFSIE method is confined only to the area of the cavity, which is $0.24\lambda^2$. The large solution region used in the FEM-BGT-II and FEM-PML solutions is needed to minimize the effect of evanescent waves on the absorbing boundary condition or PML at the top boundary. The solution time needed for the methods employing PML and BGT-II were approximately 75 and 220 seconds, respectively, while only 9 seconds were needed to solve the same example using TFSIE. Notice that, however, that all developed algorithms for comparison purpose (i.e., FEM-PML) were not necessarily optimized for maximum efficiency; nevertheless, this solution-time comparison gives a perspective on the difference in execution time between the different methods. Figure 5.5 shows the total magnetic field at the aperture of the 0^{th} cavity in the same array for the case of TE$_z$ incident plane wave. The results in Fig. 5.5 shows strong agreement between the results obtained by this method and those obtained using FEM-BGT-II.

To show the versatility of the proposed method in solving cavities with inhomogeneous fillings, an infinite array of $0.9\lambda \times 0.5\lambda$ rectangular cavities filled by three layer of dielectric materials is considered as shown in the inset of Fig. 5.6. The layers have equal width of 0.3λ. The center layer has a permittivity of $\varepsilon_r = 4$ while the other layers have a permittivity of $\varepsilon_r = 2.1$. The periodicity of the array is $P = 1\lambda$. Figures 5.6 and 5.7 show the total electric and magnetic fields at the aperture of the 0^{th} cavity for an obliquely incident plane wave with incident angle of 10°, for the TM$_z$ and TE$_z$ cases, respectively. The results,

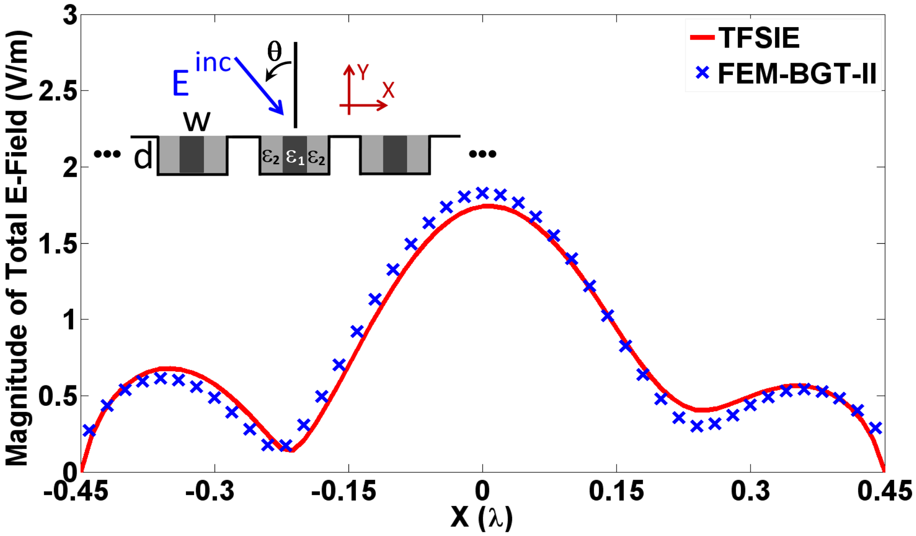

Figure 5.6: Amplitude of total E-field at the aperture of an infinite array of $0.9\lambda \times 0.5\lambda$ rectangular cavities filled with inhomogeneous dielectric material ($\varepsilon_{r_1} = 4$ & $\varepsilon_{r_2} = 2.1$), TM$_z$ case, $\theta = 10°$, calculated using TFSIE, and the finite-element method using PBC and the second order BGT (FEM-BGT-II). The periodicity of the array is 1λ.

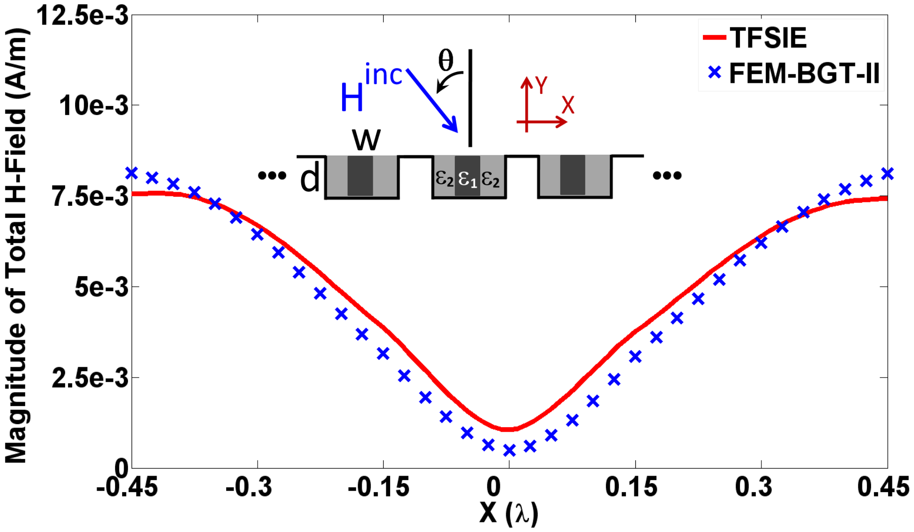

Figure 5.7: Amplitude of total H-field at the aperture of an infinite array of $0.9\lambda \times 0.5\lambda$ rectangular cavities filled with inhomogeneous dielectric material ($\varepsilon_{r_1} = 4$ & $\varepsilon_{r_2} = 2.1$), TE$_z$ case, $\theta = 10°$, calculated using TFSIE, and the finite-element method using PBC and the second order BGT (FEM-BGT-II). The periodicity of the array is 1λ.

show strong agreement between the results obtained using TFSIE and those obtained using FEM-BGT-II. The computational domain needed for the FEM-BGT-II solution is approximately 11 times larger than that used by TFSIE.

Next, an infinite periodic array of bottle-shaped cavities engraved in a PEC surface is considered. This problem was presented in [26]. The schematic of the bottle-shaped cavity is shown in Fig. 5.8. The cavities have minimum and maximum widths of $w_1 = 0.4\lambda$ and $w_2 = 1\lambda$, respectively. Also the total depth of the cavities is $d_1 + d_2 = 0.4\lambda + 0.5\lambda = 0.9\lambda$. The neck and the body of the cavities are filled by dielectric materials with permittivities of $\varepsilon_{r_1} = 2.1$ and $\varepsilon_{r_2} = 4$, respectively. The periodicity of the array is $P = 1.2\lambda$. Figure 5.9 shows the total electric field at the aperture of the 0^{th} cavity for a TM_z incident plane wave incident angle of 45°. The results in Fig. 5.9 show strong agreement between the calculations using TFSIE and those calculated using FEM-BGT-II.

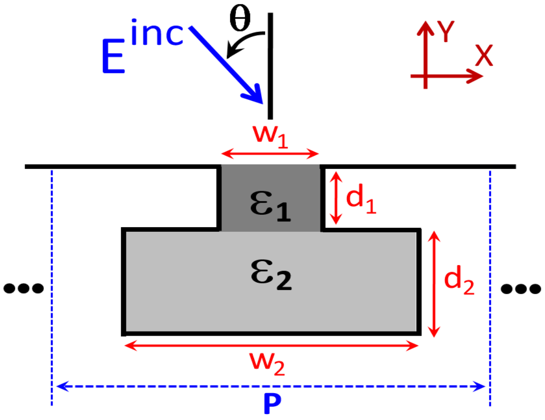

Figure 5.8: Schematic of an unit-cell of an infinite periodic array of bottle-shaped cavities engraved in a conducting surface. Each cavity has total depth of $d_1 + d_2$, and minimum and maximum widths of w_1 and w_2, respectively.

To validate the far-field calculation using the method proposed in this work, an infinite array of air-filled bottle-shaped cavities with the dimensions similar to those in [26] is considered. Figure 5.10 shows the grating efficiency of the zero-order diffraction as a function of the depth of the cavities for TM_z polarized obliquely incident plane wave. The results in Fig. 5.10 show strong agreement between TFSIE calculation and those in [26] that were obtained using modal methods.

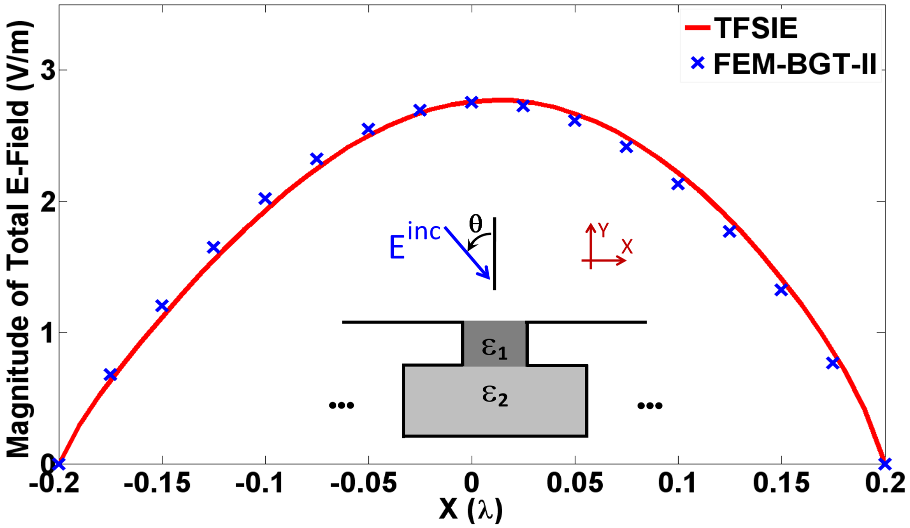

Figure 5.9: Amplitude of total E-field at the aperture of an infinite array of a bottle-shaped cavities with inhomogeneous filling ($\varepsilon_{r_1} = 2.1$ & $\varepsilon_{r_2} = 4$), TM$_z$ case, $\theta = 45°$, calculated using TFSIE, and the finite-element using PBC and the second order BGT (FEM-BGT-II). The periodicity, widths, and depths of the cavities are $P = 1.2\lambda$, ($w_1 = 0.4\lambda$ & $w_2 = 1\lambda$), and ($d_1 = 0.4\lambda$ & $d_2 = 0.5\lambda$), respectively.

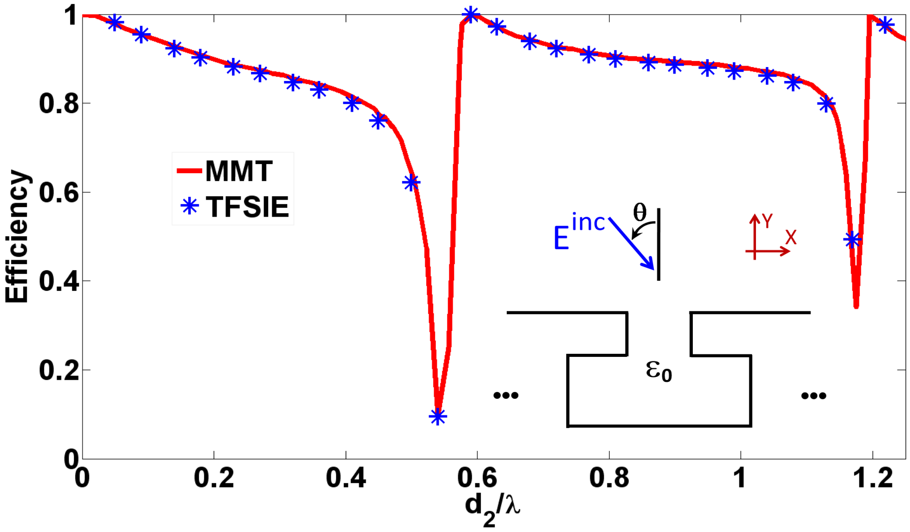

Figure 5.10: Efficiency of the zero-order diffraction as a function of the depth of the cavities in an infinite array of bottle-shaped air-filled cavities, TM$_z$ case, $\theta = 45°$, calculated using TFSIE, and mode matching technique (MMT). The periodicity, widths, and depths of the cavities are $P = 0.92\lambda$, ($w_1 = 0.4\ P$ & $w_2 = 0.9\ P$), and ($d_1 = 1/9\ d_2$), respectively.

Chapter 6

Scattering from Cavities in a Conducting Surface with a Stratified Dielectric Coating

In chapter 2, the two-boundary FE-BIM formulation was presented to solve the problem of scattering from grating surfaces consisting of single or multiple cavities engraved in an infinite PEC screen. The finite element formulation was applied inside the cavities to derive a linear system of equations associated with field unknowns. The surface integral equation employing the free-space Green's function was then applied at the opening of the cavities to truncate the computational domain and to connect the matrix subsystem generated from each cavity. By appropriate modification of Green's function, the surface integral equation was limited to the aperture of the cavities resulting in a highly accurate and efficient solution. In chapter 5, the algorithm presented in chapter 2 was extended to infinite array of uniform cavities by replacing the free-space Green's function with the quasi-periodic Green's function in the surface integral equation formulation.

Extension of the hybrid FE-BIM used in chapter 2 and 5 to solve the scattering problem from grating surfaces covered with a dielectric coating becomes more challenging due to the placement of part of the surface integral contour inside the dielectric coating. When the surface integral equation is enforced on a contour inside the dielectric coating, the free-space Green's function (typically used in previous chapters where no coatings were present) needs to be replaced with the grounded dielectric slab Green's function (GDS-GF). When this replacement takes place, one needs to be aware of the surface and leaky waves that are now generated because of the presence of the coating.

In [52], a closed-form of GDS-GF due to a current source located inside the grounded dielectric slab (interior problem) was formulated in the spectral-domain by directly solving

Helmholtz's equation. In [53], a closed-form spectral-domain vector and scalar potential Green's function for layered media was formulated using the piece-wise homogeneous transmission line Green's function. Mapping the spectral-domain Green's function into the spatial-domain leads to highly oscillatory Sommerfeld type integral including a finite number of surface-wave poles and an infinite number of leaky-wave poles. Such an integral is computationally very expensive to solve. Extensive studies on approximating the spatial domain Green's function for layered media have been reported in the literature. The most efficient approximations are Discrete Complex Image Method (DCIM) [54–57], Rational Function Fitting Method (RFFM) [58, 59], and hybrid DCIM-RFFM [60, 61] which approximate the spectral domain Green's function in terms of simple functions leading to closed-form expression for Green's function in the spatial domain.

In this chapter, a solution to the problem of scattering from an infinite and finite array of two-dimensional cavities engraved in an infinite PEC flat screen *and* covered with a stratified dielectric coating using FE-BIM is presented. Using the two-boundary formulation, the finite element formulation is applied inside the cavities to derive a linear system of equations associated with the field unknowns. The surface integral equation employing GDS-GF is formulated to derive the boundary constraint on the field unknowns at the opening of the cavities. The GDS-GF, which is the solution due to a single unit source placed inside the dielectric slab, is derived in the spectral domain by directly solving Helmholtz's equation as in [52]. The spatial domain GDS-GF is expressed in terms of a Fourier transform type integral that includes a finite number of surface-wave poles and an infinite number of leaky-wave poles. To transform the GDS-GF to a form that can be computed and thus useful for the implementation of the surface integral equation, the quasi-periodic Green's function in the spatial domain due to an infinite periodic array of the unit sources using Floquet theorem first is derived (as described in chapter 5). The quasi-periodic Green's function is then expressed in terms of an infinite series of Fourier type integrals. Next, the quasi-periodic Green's function is transformed into discrete form using the Poisson's sum formula; therefore, calculating the Fourier integrals in the Green's function series is avoided. Finally, the spatial-domain Green's function due to a single unit source is calculated by assuming the unit sources are placed infinitely far apart.

6.1 Scattering from an Infinite Periodic Array of Cavities with a Dielectric Coating

6.1.1 Finite Element Formulation of the Problem

Figure 6.1 depicts a 2-D perfectly conducting screen containing infinite periodic identical cavities coated with a homogeneous dielectric layer illuminated by an obliquely incident

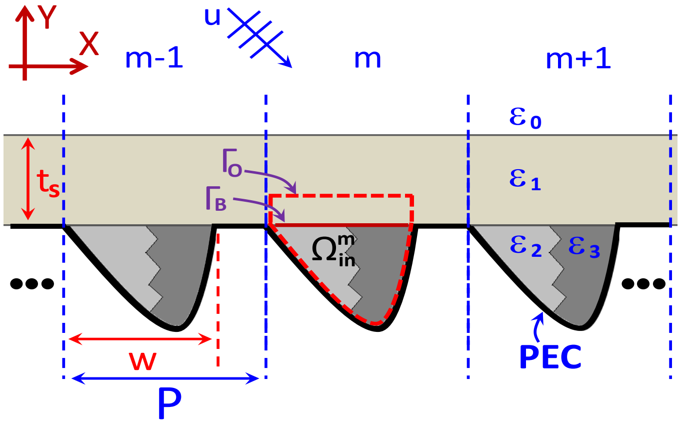

Figure 6.1: Schematic of the scattering problem from a conducting screen containing an infinite periodic array of identical cavities coated with a dielectric layer. The distance between the Γ_O contour and aperture opening is exaggerated for clarity.

plane wave. The periodicity, width of the aperture of the cavities, and the thickness of the dielectric coating are denoted by P,w, and t_s, respectively. The infinite periodic array of cavities is divided into unit-cells. The width of each unit-cell equals to the periodicity of the array P. The unit-cells are indexed by m where $m = -\infty \cdots, -1, 0, 1, \cdots \infty$. Three successive unit-cells as part of an infinite array of cavities are shown in Fig. 6.1.

For a cavity in each unit-cell (i.e., the m^{th} unit-cell), Γ_B is defined to be the contour at the opening of the cavity, and Γ_O as the top contour in close vicinity of Γ_B and inside the dielectric coating such that the region between Γ_B and Γ_O is devoid of field nodes and inhomogeneities (see Fig. 6.1). Also let Ω_{in}^m denote the interior region of the m^{th} cavity bounded by the PEC surface of the cavity and Γ_O. The finite element formulation is applied inside Ω_{in}^m to obtain the weak form of Helmholtz's equation:

$$\boldsymbol{\nabla} \cdot \left(\frac{1}{p(x,y)} \boldsymbol{\nabla} u^t \right) + q(x,y) {k_0}^2 u^t = 0 \tag{6.1}$$

where u^t is the total field. The time harmonic factor $\exp(j\omega t)$ is assumed and suppressed throughout. The functions $p(x,y)$ and $q(x,y)$ are defined as $\mu_r(x,y)$ and $\varepsilon_r(x,y)$, respectively, for the TM$_z$ polarization, or $\varepsilon_r(x,y)$and $\mu_r(x,y)$, respectively, for the TE$_z$ polarization, and k_0 is the propagation constant of the wave in free space.

Using the finite element formulation inside the solution domain Ω_{in}^m as in section 5.1, the finite element system matrix can be represented symbolically as

$$\begin{bmatrix} M_{ii} & M_{ib} & 0 \\ M_{bi} & M_{bb} & M_{bo} \\ 0 & M_{ob} & M_{oo} \end{bmatrix}^m \begin{bmatrix} u_i \\ u_b \\ u_o \end{bmatrix}^m = \begin{bmatrix} F_i \\ F_b \\ F_o \end{bmatrix}^m \tag{6.2}$$

where u_i, u_b and u_o represent nodal field values inside the m^{th} cavity, on Γ_B, and on Γ_O of the m^{th} cavity, respectively. The $[F]^m$ matrix represents the impressed sources at each node; therefore, for the problem of scattering from cavities considered in this work, $[F]^m$ is zero. The imposition of a specific excitation represented by the incident plane wave has to be taken into consideration through a boundary constraint that establishes a relationship between the incident field, the boundary nodes and the interior nodes in Eq. (6.2).

6.1.2 Surface Integral Equation

Figure 6.2 represents the schematic of the half-space Ω_∞ above an infinite array of cavities engraved in the PEC screen including the dielectric slab. The region Ω_∞ is enclosed by the surface integral contour $\Gamma + \Gamma_\infty$. In Ω_∞, the field vector $u(\boldsymbol{\rho})$ has only a z-component and is expressed by the surface integral equation

$$\begin{aligned} u_z(\boldsymbol{\rho}) = &- \int_{\Omega_\infty} g_z(\boldsymbol{\rho}') G^{e,h}(\boldsymbol{\rho}, \boldsymbol{\rho}') d\Omega \\ &- \oint_{\Gamma+\Gamma_\infty} \left(u_z(\boldsymbol{\rho}') \frac{\partial G^{e,h}(\boldsymbol{\rho}, \boldsymbol{\rho}')}{\partial n'} - G^{e,h}(\boldsymbol{\rho}, \boldsymbol{\rho}') \frac{\partial u_z(\boldsymbol{\rho}')}{\partial n'} \right) d\Gamma. \end{aligned} \tag{6.3}$$

In Eq. (6.3), $u_z(\boldsymbol{\rho})$ and $g_z(\boldsymbol{\rho})$ represent the electric field $E_z(\boldsymbol{\rho})$ and the electric current $J_z(\boldsymbol{\rho})$, respectively, for the TM$_z$ polarization, or the magnetic field $H_z(\boldsymbol{\rho})$ and the magnetic current $M_z(\boldsymbol{\rho})$, respectively, for the TE$_z$ polarization. Also, $G^{e,h}(\boldsymbol{\rho}, \boldsymbol{\rho}')$ is introduced as the grounded dielectric slab Green's function which is the solution to a current filament located at $\boldsymbol{\rho}'$. The superscripts "e" and "h" represent Green's function obtained as the solution to an electric current source for the TM$_z$ polarization, and a magnetic current source for the TE$_z$ polarization, respectively.

In Eq. (6.3), $u_z(\boldsymbol{\rho})$ on the left-hand side, represents the total field value at any point inside the dielectric layer. Also the first term on the right-hand side represents the excitation due to the current source $g_z(\boldsymbol{\rho}')$. In the scattering problem, this term is interpreted as the incident plane-wave and its multiple reflections by the PEC screen and the air-dielectric interface in absence of the cavities. Since both $u_z(\boldsymbol{\rho}')$ and $G^{e,h}(\boldsymbol{\rho}, \boldsymbol{\rho}')$ satisfy the Sommerfeld radiation condition at infinity (in the next section it will be shown that the fields satisfy Sommerfeld radiation condition on the part of the Γ_∞ boundary located inside the dielectric layer as well as free-space), the integration along Γ_∞ in the second term of right-hand side of Eq. (6.3) vanishes (see Eq. (A.7)).

For the TM$_z$ polarization where the electric field vector is parallel to the axis of the cavities, $G^e(\boldsymbol{\rho}, \boldsymbol{\rho}')$ satisfies Dirichlet boundary condition $G^e(\boldsymbol{\rho}, \boldsymbol{\rho}')_{|y'=0} = 0$ (i.e., $G^e(\boldsymbol{\rho}, \boldsymbol{\rho}') = 0$ on Γ). Additionally, $u_z(\boldsymbol{\rho}')$ is zero on the PEC segments of the Γ. Consequently, Eq. (6.3)

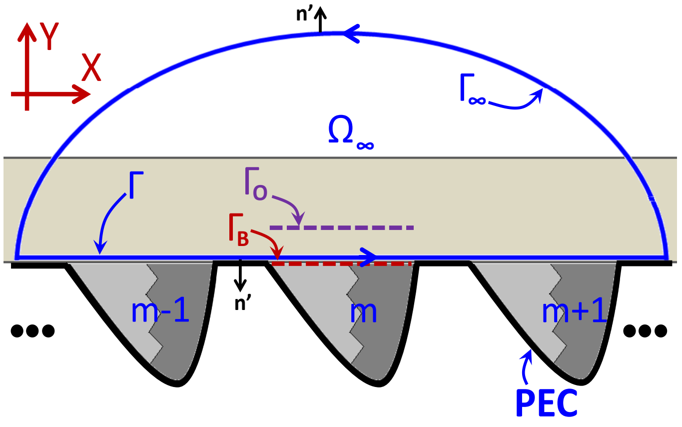

Figure 6.2: Schematic of the surface integral contour in the half-space above the cavities.

is simplified as

$$u_z(\boldsymbol{\rho}) = u_z^{excit}(\boldsymbol{\rho}) - \sum_{m=-\infty}^{\infty} \int_{\Gamma_B^m} u_z(\boldsymbol{\rho}') \frac{\partial G^e(\boldsymbol{\rho}, \boldsymbol{\rho}')}{\partial n'} d\Gamma \tag{6.4}$$

where integration is performed at the aperture of all cavities Γ_B^m. For the TE$_z$ polarization where the magnetic field vector is parallel to the axis of the cavities, $G^h(\boldsymbol{\rho}, \boldsymbol{\rho}')$ satisfies Neumann boundary condition $\partial G^h(\boldsymbol{\rho}, \boldsymbol{\rho}')/\partial n'_{|y'=0} = 0$ (i.e., $\partial G^h(\boldsymbol{\rho}, \boldsymbol{\rho}')/\partial y' = 0$ on Γ). In addition, $\partial u_z(\boldsymbol{\rho}')/\partial n'$ is zero on the PEC segments of the Γ. Consequently, Eq. (6.3) is simplified as

$$u_z(\boldsymbol{\rho}) = u_z^{excit}(\boldsymbol{\rho}) + \sum_{m=-\infty}^{\infty} \int_{\Gamma_B^m} G^h(\boldsymbol{\rho}, \boldsymbol{\rho}') \frac{\partial u_z(\boldsymbol{\rho}')}{\partial n'} d\Gamma. \tag{6.5}$$

The second term on the right-hand side of Eqs. (6.4), (6.5) represents the scattered field due to the apertures of the cavities.

Physically, the cavities are indistinguishable in structure, therefore a similar distribution of the field magnitude at the apertures of all cavities is expected. Using the Floquet theorem, the total field values at the aperture of the cavities $u_z(\boldsymbol{\rho}')$ are related as

$$u_z(\boldsymbol{\rho}' + mP\hat{x}) = u_z(\boldsymbol{\rho}') e^{-jmk_{x_0}P} \tag{6.6}$$

where $k_{x_0} = k_0 \sin\theta$. Consequently, the integration over all apertures in Eq. (6.4), and Eq. (6.5) can be limited to aperture of *only* one cavity (see sections 5.2.1 and 5.2.2)

$$u_z(\boldsymbol{\rho}) = u_z^{excit}(\boldsymbol{\rho}) - \int_{\Gamma_B} u_z(\boldsymbol{\rho}') \frac{\partial G_Q^e(\boldsymbol{\rho}, \boldsymbol{\rho}')}{\partial n'} d\Gamma \tag{6.7}$$

for the TM$_z$ polarization, and

$$u_z(\boldsymbol{\rho}) = u_z^{excit}(\boldsymbol{\rho}) + \int_{\Gamma_B} G_Q^h(\boldsymbol{\rho}, \boldsymbol{\rho}') \frac{\partial u_z(\boldsymbol{\rho}')}{\partial n'} d\Gamma \tag{6.8}$$

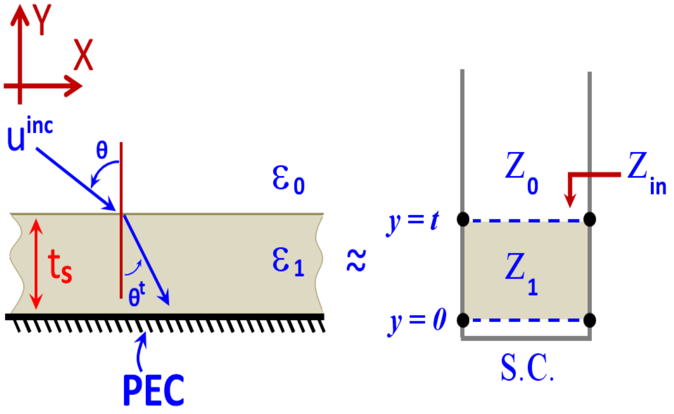

Figure 6.3: Schematic of the grounded dielectric slab and the equivalent transmission line model.

for the TE$_z$ polarization, respectively. In Eq. (6.7)-(6.8), $G_Q^{e,h}(\boldsymbol{\rho},\boldsymbol{\rho}')$ is defined as quasi-periodic GDS-GF and expressed as

$$G_Q^{e,h}(\boldsymbol{\rho},\boldsymbol{\rho}') = \sum_{m=-\infty}^{\infty} e^{-jmk_{x0}P} G^{e,h}(\boldsymbol{\rho},\boldsymbol{\rho}'+mP\hat{x}). \tag{6.9}$$

In the next section an algorithm will be presented to calculate the quasi-periodic GDS-GF in spatial domain.

To calculate the u_z^{excit} in Eq. (6.7), and Eq. (6.8), the grounded dielectric slab is modeled as a shorted transmission line with characteristic impedance of Z_1 cascaded with an infinitely long transmission line with characteristic impedance of Z_0 (see Fig. 6.3). Therefore, the field at any point inside the dielectric slab in absence of the cavities can be written as

$$u_z^{excit}(\boldsymbol{\rho}) = E_z^{inc}(x,t_s)e^{-jk_{y0}t_s}\left(\frac{2Z_{in}}{Z_{in}+Z_0}\right)\frac{\sin(k_{y_1}y)}{\sin(k_{y_1}t_s)} \tag{6.10}$$

for the TM$_z$ polarization, and

$$u_z^{excit}(\boldsymbol{\rho}) = H_z^{inc}(x,t_s)e^{-jk_{y0}t_s}\left(\frac{\cos\theta}{\cos\theta^t}\frac{2Z_0}{Z_{in}+Z_0}\right)\frac{\cos(k_{y_1}y)}{\cos(k_{y_1}t_s)} \tag{6.11}$$

for the TE$_z$ polarization, respectively. In Eqs. (6.10)-(6.11), Z_{in} is defined as the input impedance of the transmission line measured at the air-dielectric interface $y = t_s$.

By discretizing the aperture of the cavity Γ_B, Eqs. (6.7)-(6.8) are represented in matrix form as

$$[u_o] = [T] + [S]\,[u_b] \tag{6.12}$$

for the TM$_z$ polarization, and

$$\left[u_o\right] = \left\{\left[I\right] + \left[S\right]\right\}^{-1}\left[T\right] + \left\{\left[I\right] + \left[S\right]\right\}^{-1}\left[S\right]\left[u_b\right] \tag{6.13}$$

for the TE$_z$ polarization, respectively, where $[I]$ in Eq. (6.13) represents unity matrix. Combining Eq. (6.12) or Eq. (6.13) with Eq. (6.2) in matrix form results in the modified system matrix as

$$\begin{bmatrix} M_{ii} & M_{ib} \\ M_{bi} & M_{bb} + M_{bo}S \end{bmatrix} \begin{bmatrix} u_i \\ u_b \end{bmatrix} = \begin{bmatrix} F_i \\ F_b - M_{bo}T \end{bmatrix} \tag{6.14}$$

for the TM$_z$ polarization, or

$$\begin{bmatrix} M_{ii} & M_{ib} \\ M_{bi} & M_{bb} + M_{bo}(I+S)^{-1}S \end{bmatrix} \begin{bmatrix} u_i \\ u_b \end{bmatrix} = \begin{bmatrix} F_i \\ F_b - M_{bo}(I+S)^{-1}T \end{bmatrix}. \tag{6.15}$$

for the TE$_z$ polarization, respectively. The solution of the modified system matrices in Eqs. (6.14)-(6.15) can be obtained using commonly used methods for solving linear systems.

6.2 Green's Function for the Grounded Dielectric Slab (Interior Problem)

Figure 6.4(a) depicts the schematic of a current source located inside a 2-D infinite grounded dielectric slab. The permittivity and thickness of the dielectric slab are denoted by ε_1, and t_s respectively. By directly solving Helmholtz's equation as in [52], the GDS-GF in spatial domain is expressed in terms of Fourier transform integral as

$$G^{e,h}(x, y; x', y') = \frac{1}{2\pi}\int_{-\infty}^{\infty} e^{-jk_x|x-x'|}\tilde{G}^{e,h}(y, y', k_x)dk_x \tag{6.16}$$

where $G^{e,h}(x, y; x', y')$ and $\tilde{G}^{e,h}(y, y', k_x)$ are GDS-GF in spatial, and spectral domain, respectively. In Eq. (6.16), $\tilde{G}^{e}(y, y', k_x)$ is defined as

$$\tilde{G}^{e}(y, y', k_x) = \begin{cases} \frac{jk_{y_0}\sin(k_{y_1}(t_s-y)) + k_{y_1}\cos(k_{y_1}(t_s-y))}{k_{y_1}\left(jk_{y_0}\sin(k_{y_1}t_s) + k_{y_1}\cos(k_{y_1}t_s)\right)}\sin(k_{y_1}y'), & y' \leq y < t_s; \\ \\ \frac{e^{-jk_{y_0}(y-t_s)}}{\left(jk_{y_0}\sin(k_{y_1}t_s) + k_{y_1}\cos(k_{y_1}t_s)\right)}\sin(k_{y_1}y'), & y' < t_s \leq y \end{cases} \tag{6.17}$$

for the TM$_z$ polarization, and $\tilde{G}^{h}(y, y', k_x)$ is defined as

$$\tilde{G}^{h}(y, y', k_x) = \begin{cases} \frac{jk_{y_0}\sin(k_{y_1}(t_s-y)) + k_{y_1}\cos(k_{y_1}(t_s-y))}{k_{y_1}\left(jk_{y_0}\cos(k_{y_1}t_s) - k_{y_1}\sin(k_{y_1}t_s)\right)}\cos(k_{y_1}y'), & y' \leq y < t_s; \\ \\ \frac{e^{-jk_{y_0}(y-t_s)}}{\left(jk_{y_0}\cos(k_{y_1}t_s) - k_{y_1}\sin(k_{y_1}t_s)\right)}\cos(k_{y_1}y'), & y' < t_s \leq y \end{cases} \tag{6.18}$$

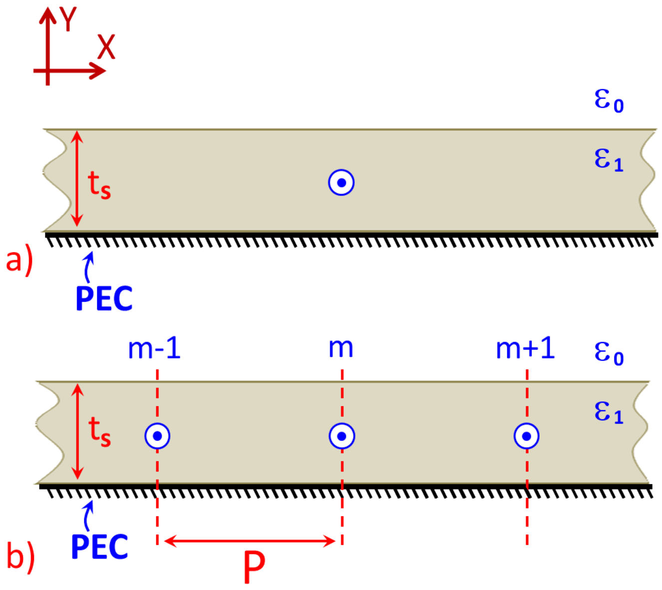

Figure 6.4: Schematic of (a) a single unit source (b) an infinite periodic array of unit sources with an uniform progressive phase shift, located inside a grounded dielectric slab.

for the TE$_z$ polarization, respectively. In Eqs. (6.16)-(6.18), k_x, $k_{y_0} = (k_0^2 - k_x^2)^{1/2}$ and $k_{y_1} = (k_1^2 - k_x^2)^{1/2}$ represent the Cartesian components of the propagation vector in the air and dielectric. Note that the x-component of the propagation vector k_x is continuous across the air-dielectric interface. The position of the source point and field point are denoted by (x', y'), and (x, y), respectively.

In Eq. (6.16), $G^e(x, y; x', y')$ and $G^h(x, y; x', y')$ satisfy Dirichlet boundary condition (i.e., $G^e{}_{|y'=0} = 0$), and Neumann boundary condition (i.e., $\partial G^h/\partial y'{}_{|y'=0} = 0$) on the PEC screen, respectively. In addition, $G^e(x, y; x', y')$ and $G^h(x, y; x', y')$ satisfy the Sommerfeld radiation condition at infinity as follows.

Inside the dielectric slab ($y < t_s$), waves are superposition of the plane waves having a continuous spectrum of wave-numbers k_x traveling along the x-axis while $\tilde{G}^{e,h}(y, y', k_x)$ represents an infinite number of standing-waves along the y-axis. The Sommerfeld radiation condition for each mode is then written as

$$\lim_{|x|\to\infty}\left(\frac{1}{2\pi}\int_{-\infty}^{\infty}(\frac{\partial}{\partial x} \pm jk_x)e^{-jk_x|x-x'|}\tilde{G}^{e,h}(y, y', k_x)dk_x\right) = 0. \tag{6.19}$$

Outside of the dielectric slab ($t_s < y$) waves are superposition of the plane waves having a continuous spectrum of wave-numbers k_x but a total wave-number of k_0 traveling radially, while $\tilde{G}^{e,h}(y, y', k_x)$ represents an infinite number of propagating-waves along the y-axis.

The Sommerfeld radiation condition for each mode is then written as

$$\lim_{\rho\to\infty}\left(\frac{1}{2\pi}\int_{-\infty}^{\infty}(\frac{\partial}{\partial\rho}+jk_0)e^{-jk_x|x-x'|}\tilde{G}^{e,h}(y,y',k_x)dk_x\right)=0 \tag{6.20}$$

where ρ represents the position of the field point in cylindrical coordinates.

6.2.1 Quasi-Periodic GDS-GF to an Array of Periodic Unit Sources

To derive the quasi-periodic grounded dielectric slab Green's function used in Eqs. (6.7)-(6.8) in closed form, let assume an infinite periodic array of current sources located inside the grounded dielectric slab. Figure 6.4(b) shows the schematic of three successive current sources as part of infinite array of current sources located inside a 2-D infinite grounded dielectric slab. The periodicity of the current sources is denoted by P. In Fig. 6.4(b), the current sources are indexed by m. Also, assume a phase shift of $\exp(-jk_{x_0}P)$ between successive current sources in the periodic array. By assigning a phase of zero to the current source located at origin (i.e., $m=0$), the phase of m^{th} current source is then written as $\exp(-jmk_{x_0}P)$. The quasi-periodic GDS-GF due to an infinite periodic array of current sources is defined (see Eqs. (5.15) and (5.26))

$$G_Q^{e,h}(x,y;x',y')=\sum_{m=-\infty}^{\infty}e^{-jmk_{x_0}P}\left(\frac{1}{2\pi}\int_{-\infty}^{\infty}e^{-jk_x|x-(x'+mP)|}\tilde{G}^{e,h}(y,y',k_x)dk_x\right). \tag{6.21}$$

Using Poisson's sum formula and the relationship derived in [62], the quasi-periodic Green's function in Eq. (6.21) is simplified to the discrete form as

$$G_Q^{e,h}(x,y;x',y')=\frac{1}{P}\sum_{m=-\infty}^{\infty}e^{-jk_{x_m}|x-x'|}\tilde{G}^{e,h}(y,y',k_{x_m}) \tag{6.22}$$

where k_{x_m} has discrete values of

$$k_{x_m}=k_{x_0}+\frac{2m\pi}{P}. \tag{6.23}$$

It is necessary to truncate the series in Eq. (6.22) to implement the surface integral equation numerically. To study the effect of the series truncation on the accuracy of the method, the following partial sums are defined for the TM$_z$ and TE$_z$ cases, respectively as

$$S_N^e=\frac{1}{P}\sum_{m=-N}^{N}e^{-jk_{x_m}|x-x'|}\frac{\partial}{\partial y'}\tilde{G}^e(y,y',k_{x_m}), \tag{6.24}$$

and

$$S_N^h = \frac{1}{P} \sum_{m=-N}^{N} e^{-jk_{x_m}|x-x'|} \tilde{G}^h(y, y', k_{x_m}). \tag{6.25}$$

In Eq. (6.24), for the TM$_z$ polarization, $\partial\tilde{G}^e/\partial y'$ is considered rather than $\tilde{G}^e$ since the former appears in the surface integral formulation. The effect of truncation on the convergence of the partial sum of the series is shown in following versus different factors such as lateral distance between the source point and the field point ($|x - x'|$), thickness of the dielectric slab (t_s), and the loss tangent of the dielectric coating ($\varepsilon''/\varepsilon'$).

Figure 6.5 shows the normalized magnitude of the S_N^e for the TM$_z$ case and S_N^h for the TE$_z$ case versus N for three various separation values between the source point and the field point ($|x - x'|$). It is observed that the larger lateral distance between the source point and the field point results in faster convergence of the series, and S_N^h converges faster than S_N^e. In Fig. 6.6, normalized magnitude of S_N^e and S_N^h versus N for three various slab thicknesses (t_s) are shown. It is observed that the series converges faster for the larger values of t_s. Physically, by increasing the slab's thickness, the distance between source and its images increases and therefore, the level of contribution to the field distribution around the source is limited to the source itself and few image sources. Mathematically, the series terms with large harmonic numbers decay fast. The normalized magnitude of the S_N^e and S_N^h versus N for various dielectric loss tangent values ($\varepsilon''/\varepsilon'$) is shown in Fig. 6.7.

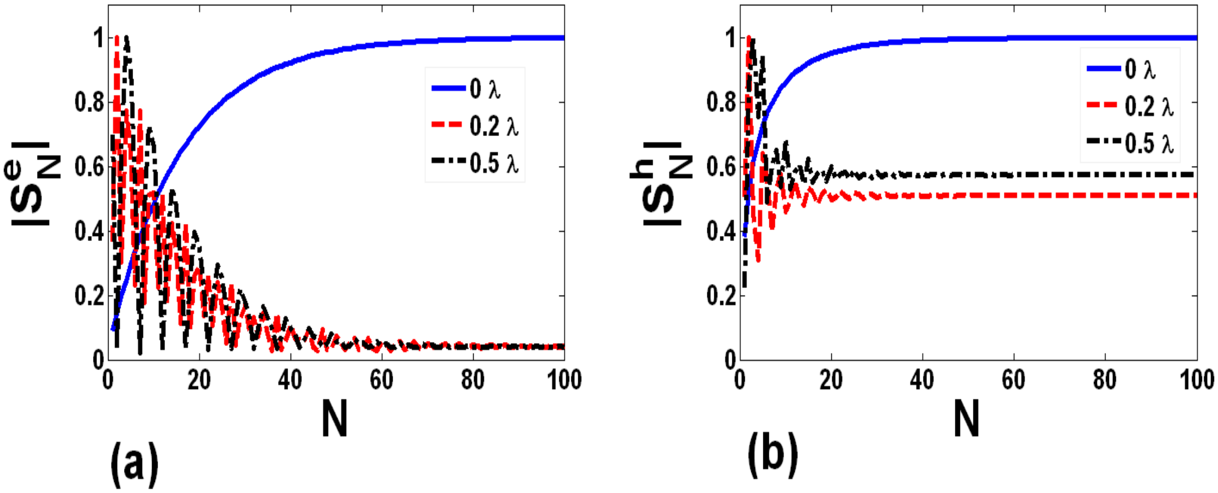

Figure 6.5: Normalized magnitude of the partial sum of the series (a) for the TM$_z$ case (Eq. (6.24)), and (b) for the TE$_z$ case (Eq. (6.25)) versus lateral distance of the source point and the field point ($|x - x'|$). $t_s = 0.25\lambda$, $\varepsilon''/\varepsilon' = 0.5$, $k_{x_0} = k_0/2$, $y = 0.01\lambda$, and $y' = 0$.

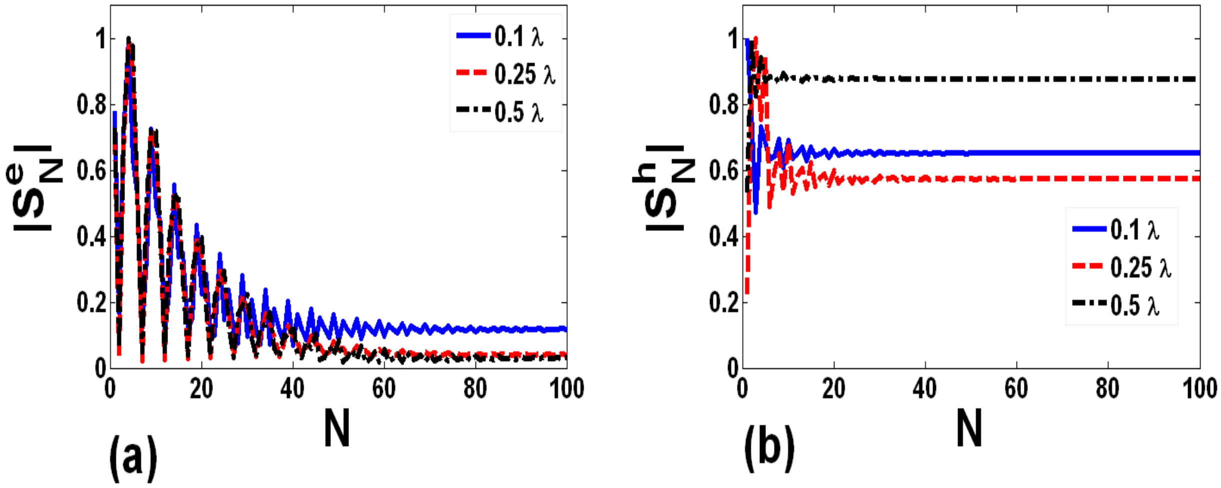

Figure 6.6: Normalized magnitude of the partial sum of the series (a) for the TM$_z$ case (Eq. (6.24)), and (b) for the TE$_z$ case (Eq. (6.25)) versus thickness of the dielectric coating (t_s). $|x - x'| = 0.6\lambda$, $\varepsilon''/\varepsilon' = 0.5$, $k_{x_0} = k_0/2$, $y = 0.01\lambda$, and $y' = 0$.

It is observed that by increasing the loss of the dielectric coating, the series in S_N^e and S_N^h converge faster.

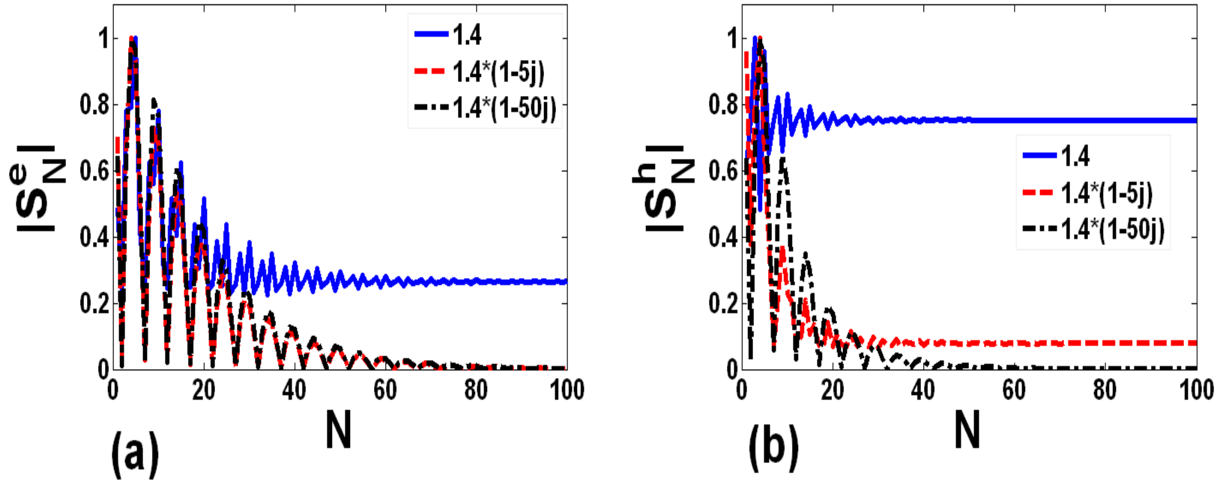

Figure 6.7: Normalized magnitude of the partial sum of the series (a) for the TM$_z$ case (Eq. (6.24)), and (b) for the TE$_z$ case (Eq. (6.25)) versus loss tangent of the dielectric coating ($\varepsilon''/\varepsilon'$). $|x - x'| = 0.6\lambda$, $t_s = 0.25\lambda$, $k_{x_0} = k_0/2$, $y = 0.01\lambda$, and $y' = 0$.

The convergence studies conducted above show that the accuracy of the algorithm presented here for calculating the quasi-periodic GDS-GF is guaranteed by choosing proper N. It is important to emphasize that the convergence behavior of the quasi-periodic GDS-GF is only dependent on the geometrical and material properties of the coating. Notice that using some mathematical techniques such as extraction of images may accelerate the convergence of the series.

6.2.2 GDS-GF due to a Single Unit Source

The grounded dielectric slab Green's function due to a single unit source is defined using the concept of quasi-periodic GDS-GF. When infinite current sources exist, many sources contribute through guided waves in the dielectric layer to the field distribution in the close proximity of a single current source. The level of contribution by other sources strongly depends on the distance between sources. If the current sources are placed infinitely far apart, the field contribution within the close proximity of a single current source will be due to that source itself. In the formulation presented here, the distance between the current sources appears as the periodicity P (see Fig. 6.4 and Eqs. (6.22)-(6.23)). Therefore, the GDS-GF as a solution to a single current source $G_S^{e,h}(x, y; x', y')$ can be expressed as

$$G_S^{e,h}(x, y; x', y') = \lim_{P\to\infty} \left(\frac{1}{P} \sum_{m=-\infty}^{\infty} e^{-jk_{x_m}|x-x'|} \tilde{G}^{e,h}(y, y', k_{x_m}) \right). \tag{6.26}$$

In Eq. (6.26), the subscript "S" is used to show the difference between the discrete form of $G_S^{e,h}$ and its original form $G^{e,h}$ in Eq. (6.16).

It is important to note that Eq. (6.26) is valid for thin substrates or thick lossy substrates. From a mathematical point of view, in the case of lossless dielectric slab, the surface-waves excited in the dielectric slab have poles on the real axis. By increasing the period P, the sample points in the summation of Eq. (6.26) corresponding to different values of the summation index m will move closer to each other and one of them is always very close to the surface-wave pole. Therefore, the series in Eq. (6.26) will not converge. However, for thin substrates where the residue of the pole is small enough, the series will converge.

Figures 6.8 and 6.9 show the magnitude of S_N^e for the TM$_z$ case and S_N^h for the TE$_z$ case versus N for various periodicity values of an infinite array of current sources inside the lossless, and lossy thin dielectric coating, respectively. To isolate the current sources completely, one may assign very large value to the periodicity of the array in Eq. (6.26). The major drawback of assigning a large value to the periodicity of the array is slow convergence of S_N^e and S_N^h in Eq. (6.24), and Eq. (6.25), respectively. The convergence study suggests that extending the periodicity to several wavelengths (i.e.; $P \approx 10 - 20\lambda$) guarantees isolation of the current sources in addition to the fast convergence of the series.

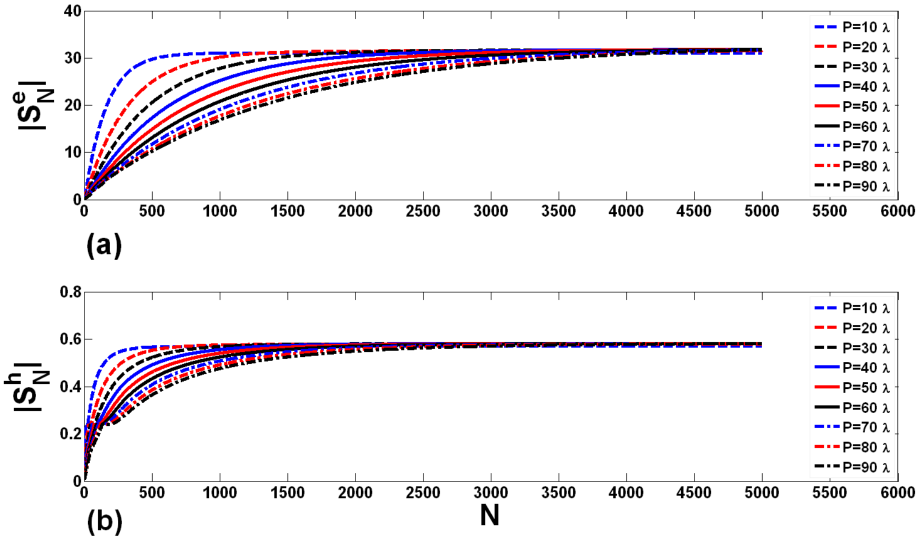

Figure 6.8: Magnitude of the partial sum of the series (a) for the TM$_z$ case (Eq. (6.24)), and (b) for the TE$_z$ case (Eq. (6.25)) versus periodicity of an infinite array (P) inside a thin lossless dielectric coating. $|x - x'| = 0$, $t_s = 0.25\lambda$, $k_x = k_0/2$, $y = 0.01\lambda$, and $y' = 0$.

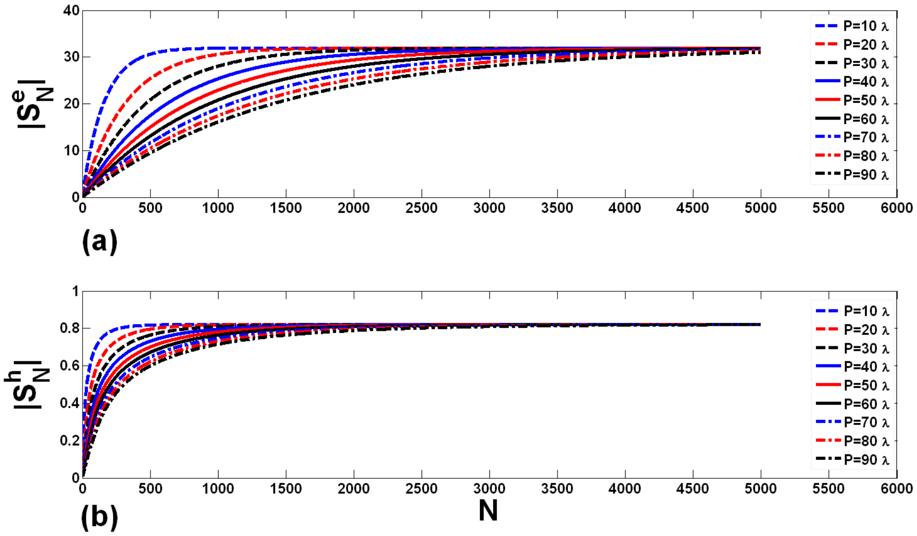

Figure 6.9: Magnitude of the partial sum of the series (a) for the TM$_z$ case (Eq. (6.24)), and (b) for the TE$_z$ case (Eq. (6.25)) versus periodicity of an infinite array (P) inside a thin lossy dielectric coating with $\varepsilon''/\varepsilon' = 0.5$. $|x - x'| = 0$, $t_s = 0.25\lambda$, $k_x = k_0/2$, $y = 0.01\lambda$, and $y' = 0$.

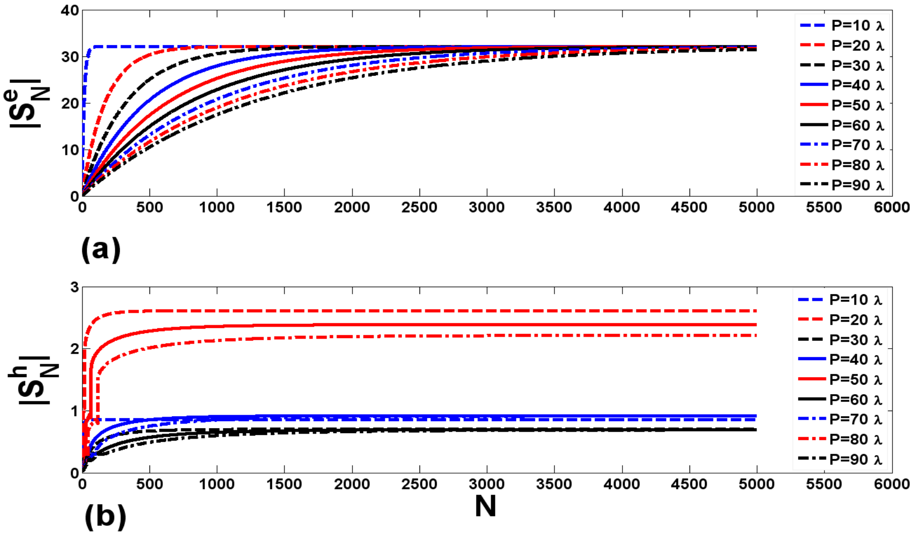

Figure 6.10: Magnitude of the partial sum of the series (a) for the TM$_z$ case (Eq. (6.24)), and (b) for the TE$_z$ case (Eq. (6.25)) versus periodicity of an infinite array (P) inside a thick lossless dielectric coating. $|x - x'| = 0$, $t_s = 1\lambda$, $k_x = k_0/2$, $y = 0.01\lambda$, and $y' = 0$.

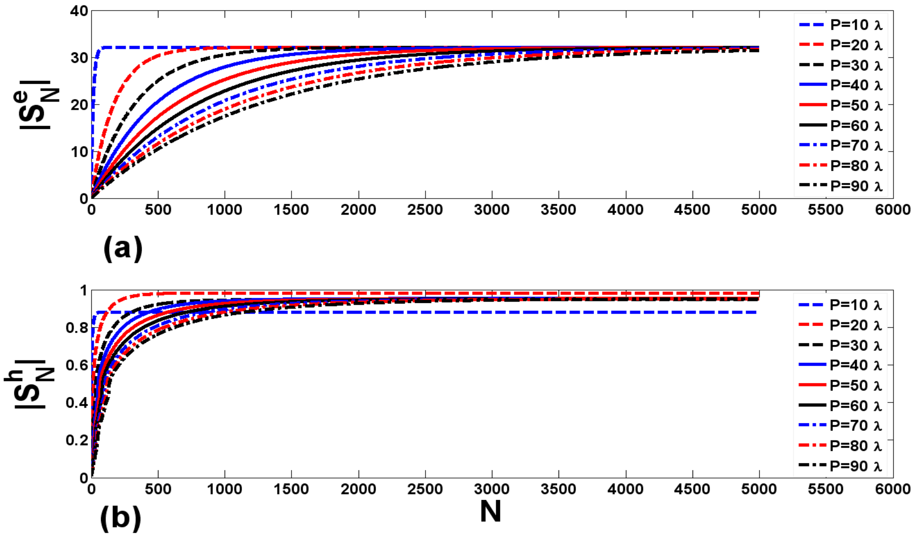

Figure 6.11: Magnitude of the partial sum of the series (a) for the TM$_z$ case (Eq. (6.24)), and (b) for the TE$_z$ case (Eq. (6.25)) versus periodicity of an infinite array (P) inside a thick lossy dielectric coating with $\varepsilon''/\varepsilon' = 0.5$. $|x - x'| = 0$, $t_s = 1\lambda$, $k_x = k_0/2$, $y = 0.01\lambda$, and $y' = 0$.

Figures 6.10 shows the magnitude of S_N^e for the TM$_z$ case and S_N^h for the TE$_z$ case versus N for various periodicity values of an infinite array of current sources inside the lossless thick dielectric coating. As it is mentioned above, the series for the TE$_z$ case does not converge even for a large number of terms. By adding a loss to the dielectric, the surface waves excited in the structure decay fast and therefore the series in Eq. (6.26) converges. Figure 6.11 shows the magnitude of the S_N^e for the TM$_z$ case and S_N^h for the TE$_z$ case versus N for various periodicity values of an infinite array of current sources inside the lossy thick dielectric coating.

6.3 Scattering from Finite Array of Non-Uniform Cavities with a Dielectric Coating

Figure 6.12 depicts the schematic of a 2-D perfectly conducting screen containing two cavities with different shapes and fillings covered with homogeneous dielectric layer illuminated by an obliquely incident plane wave. Similar to the method in section 2.4, the solution domains Ω_1 and Ω_2 are defined for the cavities. Using the finite element formulation inside the solution regions Ω_1 and Ω_2 to obtain the weak form of Helmholtz's equation results in a finite element system matrix for each cavity as

$$\begin{aligned}[M_1][u_1] &= [F_1] \\ [M_2][u_2] &= [F_2]\end{aligned} \tag{6.27}$$

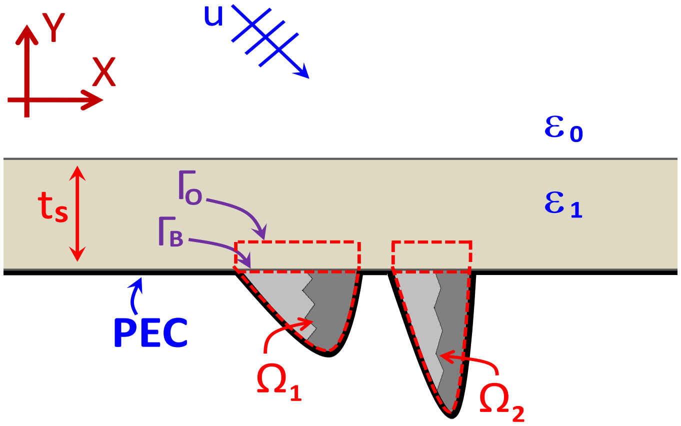

Figure 6.12: Schematic of the scattering problem from a conducting screen containing two non-uniform cavities coated with a dielectric layer.

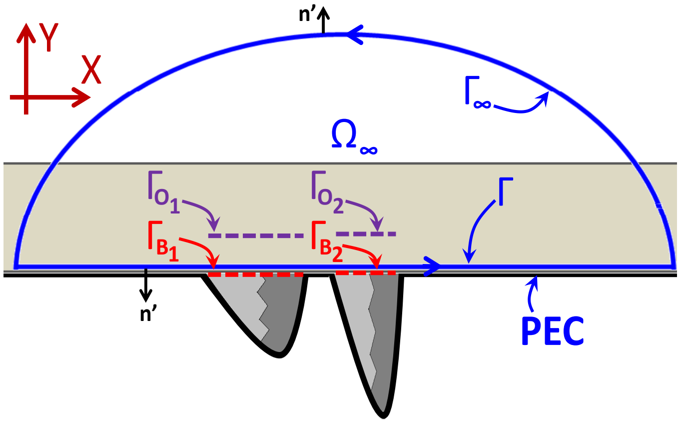

Figure 6.13: Schematic of the surface integral contour in the half-space above two cavities with different shapes and fillings.

where each system of equations can be represented symbolically as Eq. (6.2). Assembling the two systems of equations using a global numbering of nodes results

$$\begin{bmatrix} [M_1] & 0 \\ 0 & [M_2] \end{bmatrix} \begin{bmatrix} [u_1] \\ [u_2] \end{bmatrix} = \begin{bmatrix} [F_1] \\ [F_2] \end{bmatrix}. \tag{6.28}$$

Then, the surface integral equation (Eq. (6.3)) employing GDS-GF, $G_S^{e,h}(\boldsymbol{\rho}, \boldsymbol{\rho}')$, is applied at the aperture of two cavities to truncate the solution domain. Figure 6.13 represents the surface integral contour in half-space above the ground plane. Imposing proper boundary condition on $G_S^{e,h}(\boldsymbol{\rho}, \boldsymbol{\rho}')$ at infinity and on the ground plane results in

$$u_z(\boldsymbol{\rho}) = u_z^{excit}(\boldsymbol{\rho}) - \int_{\Gamma_{B_1}+\Gamma_{B_2}} u_z(\boldsymbol{\rho}') \frac{\partial G_S^e(\boldsymbol{\rho}, \boldsymbol{\rho}')}{\partial n'} d\Gamma \tag{6.29}$$

for the TM$_z$ polarization, and

$$u_z(\boldsymbol{\rho}) = u_z^{excit}(\boldsymbol{\rho}) + \int_{\Gamma_{B_1}+\Gamma_{B_2}} G_S^h(\boldsymbol{\rho}, \boldsymbol{\rho}') \frac{\partial u_z(\boldsymbol{\rho}')}{\partial n'} d\Gamma \tag{6.30}$$

for the TE$_z$ polarization, respectively. In Eqs (6.29)-(6.30), $G_S^{e,h}(\boldsymbol{\rho}, \boldsymbol{\rho}')$ is the grounded dielectric slab Green's function which is a solution to a single current source defined by Eq. (6.26). In Eq. (6.29) and Eq. (6.30), the integration is performed over the apertures of both cavities and this results in the addition of off-diagonal sub-matrices to the matrix in Eq. (6.28). The resultant system matrix becomes

$$\begin{bmatrix} [M_1'] & [C_{12}] \\ [C_{21}] & [M_2'] \end{bmatrix} \begin{bmatrix} [u_1'] \\ [u_2'] \end{bmatrix} = \begin{bmatrix} [F_1'] \\ [F_2'] \end{bmatrix} \tag{6.31}$$

where $[C_{12}]$ and $[C_{21}]$ are matrices representing the coupling between the two cavities (see section 2.4). The modified system matrix in Eq. (6.31) represents the finite element system matrix encountering the coupling between two cavities through the grounded dielectric slab Green's function. Generalizing the algorithm to N non-uniform cavities results in the following matrix system:

$$\begin{bmatrix} [M'_{(1)}] & [C_{(12)}] & \cdots & [C_{(1N)}] \\ [C_{(21)}] & [M'_{(2)}] & \cdots & [C_{(2N)}] \\ \vdots & & \ddots & \vdots \\ [C_{(N1)}] & [C_{(N2)}] & \cdots & [M'_{(N)}] \end{bmatrix} \begin{bmatrix} [u'_{(1)}] \\ [u'_{(2)}] \\ \vdots \\ [u'_{(N)}] \end{bmatrix} = \begin{bmatrix} [F'_{(1)}] \\ [F'_{(2)}] \\ \vdots \\ [F'_{(N)}] \end{bmatrix} . \tag{6.32}$$

Notice that the finite element system matrix in Eq. (6.31) or Eq. (6.32) can be represented symbolically as Eq. (6.14) for the TM$_z$ polarization or Eq. (6.15) for the TE$_z$ polarization.

6.4 Numerical Results

Once the system of equations, Eq. (6.14) for the TM$_z$ polarization or Eq. (6.15) for the TE$_z$ polarization, is derived, its solution (which gives the field values at the apertures of the cavities) can be obtained using commonly used methods for solving linear systems. In this section, examples of an infinite array of identical cavities with different dimensions, periodicity, and fillings, are provided to validate the algorithm developed in section 6.1. Next, examples of finite cavities with different geometries and fillings are provided as formulated in section 6.3.

To validate the method presented here, comparison is made to the results obtained by commercial two-dimensional finite-element simulator COMSOL [43]. Throughout this section, these solutions are referred as COMSOL. To obtain the results using COMSOL for the case of infinite array of cavities, the periodic boundary condition is applied on the lateral boundaries of the unit-cell. Also, the absorbing boundary condition is applied on the top truncation boundary. For the case of finite array of cavities, the absorbing boundary condition is applied on the lateral truncation boundaries as well as the top boundary. Without loss of generality, the magnitude of the incident electric field is assumed to be unity throughout this section. To implement the algorithm developed in this chapter, the nodal based finite element formulation is used. The solution domain is discretized using first-order triangle elements with a mesh density of approximately 20 nodes per λ for the TM$_z$ case. Since there is a discontinuity in the electric field at the edges of the cavities in the TE$_z$ case, a mesh density of 100 nodes per λ is used. Throughout this section, the solution obtained using the method presented in this paper is referred to as "Total Field Surface Integral Equation-Spatial Domain Green's Function" (TFSIE-SDGF).

6.4.1 Infinite Array of Identical Cavities

In the first example, an infinite periodic array of bottle-shaped cavities engraved in a PEC surface covered with a dielectric coating is considered. The schematic of the bottle-shaped cavity is shown in the inset of Fig. 6.14. The cavities have minimum and maximum widths of $w_1 = 0.4\lambda$ and $w_2 = 1\lambda$, respectively. The total depth of the cavities is $d_1 + d_2 = 0.4\lambda + 0.5\lambda = 0.9\lambda$. The cavities are coated with a dielectric layer having a thickness of $t_s = 0.25\lambda$, and a permittivity of $\varepsilon_{r_1} = 1.4(1 - 0.5j)$. Also the neck and the body of the cavities are filled by dielectric materials with permittivities of $\varepsilon_{r_2} = 2.1$ and $\varepsilon_{r_3} = 4$, respectively. The periodicity of the array is $P = 1.2\lambda$. Figure 6.14 shows the total electric field at the aperture of the $m = 0$ cavity for a TM$_z$ incident plane wave with an incident angle of 45°. The results in Fig. 6.14 show strong agreement between the calculations using the method presented here and those calculated using COMSOL.

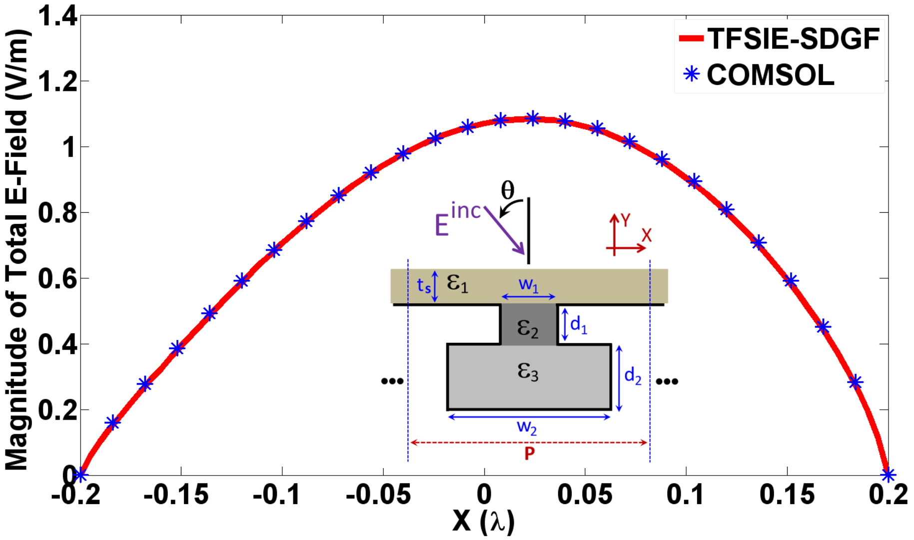

Figure 6.14: Amplitude of the total E-field at the aperture of an infinite array of bottle-shaped cavities with dielectric coating and inhomogeneous filling, TM$_z$ case, $\theta = 45°$. $\varepsilon_{r_1} = 1.4(1-0.5j)$, $\varepsilon_{r_2} = 2.1$, $\varepsilon_{r_3} = 4$, $w_1 = 0.4\lambda$, $w_2 = 1\lambda$, $d_1 = 0.4\lambda$, $d_2 = 0.5\lambda$, $P = 1.2\lambda$, and $t_s = 0.25\lambda$.

As a second example, an infinite array of $0.6\lambda \times 0.4\lambda$ rectangular cavities covered with a dielectric coating is considered. The thickness and the permittivity of the dielectric layer are $t_s = 0.25\lambda$, and $\varepsilon_{r_1} = 1.4(1 - 0.5j)$, respectively. Also, the cavities are filled by two layers of dielectric materials with permittivities of $\varepsilon_{r_2} = 4$, and $\varepsilon_{r_3} = 2.1$, as shown in the inset of Fig. 6.15. The layers have equal width of 0.3λ. The periodicity of the array is $P = 1\lambda$. Figure 6.15 shows the total magnetic field at the aperture of the $m = 0$ cavity for an obliquely incident plane wave with an incident angle of 30°, for the TE$_z$ case. The

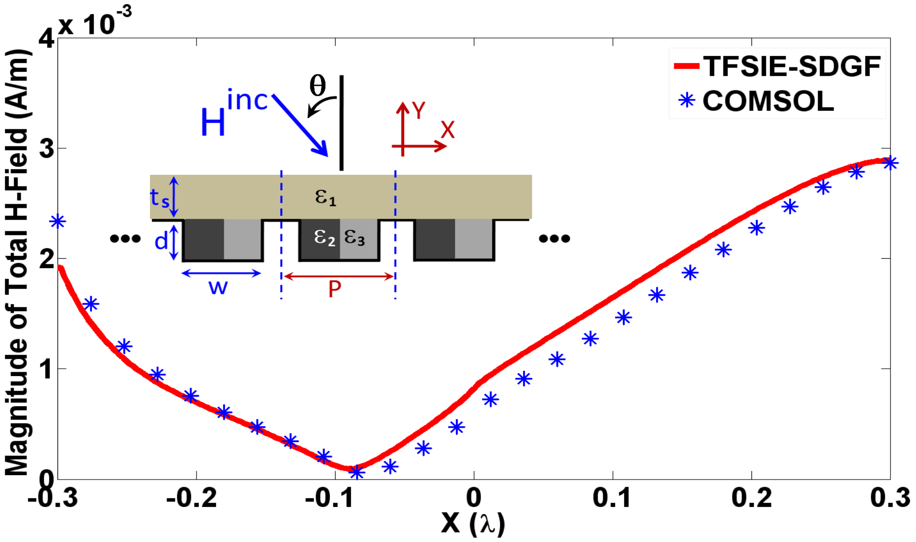

Figure 6.15: Amplitude of the total H-field at the aperture of an infinite array of rectangular cavities with dielectric coating and inhomogeneous filling, TE$_z$ case, $\theta = 30°$. $w = 0.6\lambda$, $d = 0.4\lambda$, $\varepsilon_{r_1} = 1.4(1 - 0.5j)$, $\varepsilon_{r_2} = 4$, $\varepsilon_{r_3} = 2.1$, $P = 1\lambda$, and $t_s = 0.25\lambda$.

results show close agreement between the results obtained using our method and those obtained using COMSOL.

To calculate the results using TFSIE-SDGF, the S_N^e in Eq. (6.24) for the first example, and S_N^h in Eq. (6.25) for the second example are truncated at $N = 100$. Also, it is important to note that while using COMSOL, it is needed to minimize the effect of evanescent waves on the absorbing boundary condition at the top boundary. Therefore, to achieve accurate results we located the top boundary 1λ away from the air-dielectric interface, which results in an increase of the solution region. Notice that the solution region in the method presented here is limited to the area of a cavity.

6.4.2 Finite Array of Non-Uniform Cavities

To validate the algorithm presented in section 6.2.2, two rectangular cavities with different dimensions and fillings are considered (see inset of Fig. 6.16). The cavities are coated with a dielectric layer having a thickness of $t_s = 0.25\lambda$, and a permittivity of $\varepsilon_{r_1} = 1.4(1-0.5j)$. The cavities have dimensions of $(w_1 \times d_1 = 0.6\lambda \times 0.4\lambda)$, and $(w_2 \times d_2 = 0.4\lambda \times 0.8\lambda)$, respectively and are separated by the distance of $D = 0.05\lambda$. Also, the cavities are filled with lossy dielectric materials of $\varepsilon_{r_2} = 4(1 - 0.5j)$, and $\varepsilon_{r_3} = 2.1(1 - 0.5j)$. Figures 6.16 and 6.17 show the total electric and magnetic field at the apertures of the cavities for an obliquely incident plane wave with an incident angle of 15° for the TM$_z$ case and the

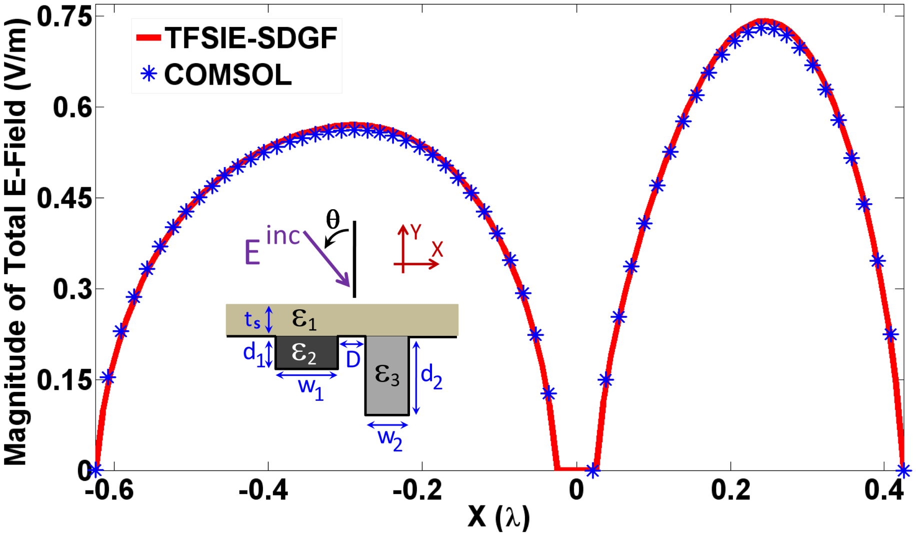

Figure 6.16: Amplitude of the total E-field at the aperture of two rectangular cavities with different dimensions and fillings, covered with a dielectric coating, TM_z case, $\theta = 15°$. $w_1 \times d_1 = 0.6\lambda \times 0.4\lambda$, $w_2 \times d_2 = 0.4\lambda \times 0.8\lambda$, separated by $D = 0.05\lambda$, $\varepsilon_{r_1} = 1.4(1 - 0.5\jmath)$, $\varepsilon_{r_2} = 4(1 - 0.5\jmath)$, $\varepsilon_{r_3} = 2.1(1 - 0.5\jmath)$, and $t_s = 0.25\lambda$.

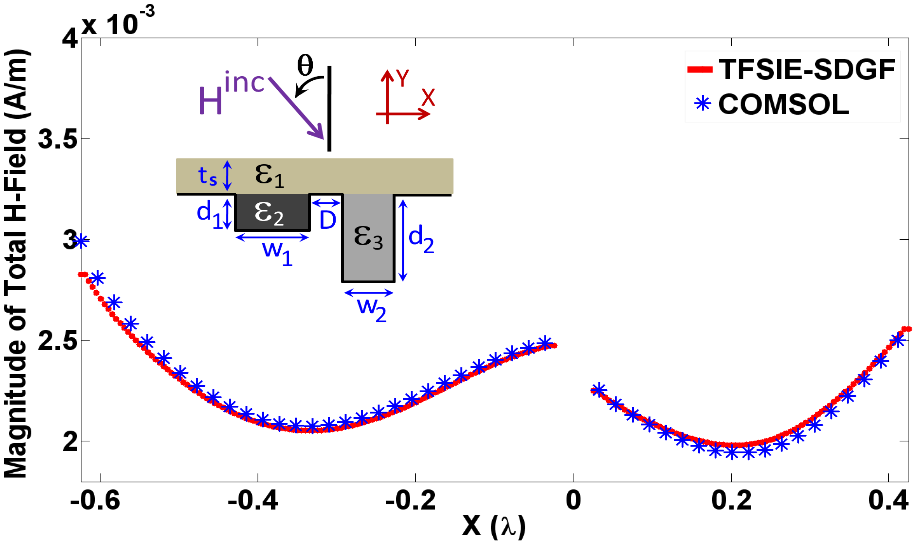

Figure 6.17: Amplitude of the total H-field at the aperture of two rectangular cavities with different dimensions and fillings, covered with a dielectric coating, TE_z case, $\theta = 15°$. $w_1 \times d_1 = 0.6\lambda \times 0.4\lambda$, $w_2 \times d_2 = 0.4\lambda \times 0.8\lambda$, separated by $D = 0.05\lambda$, $\varepsilon_{r_1} = 1.4(1 - 0.5\jmath)$, $\varepsilon_{r_2} = 4(1 - 0.5\jmath)$, $\varepsilon_{r_3} = 2.1(1 - 0.5\jmath)$, and $t_s = 0.25\lambda$.

TE$_z$ case, respectively. Strong agreement between the results calculated using the method presented here and those obtained using COMSOL is observed.

To calculate the results using TFSIE-SDGF, P is chosen as 13λ in Eq. (6.26). In addition, S_N^e in Eq. (6.24) for the TM$_z$ case, and S_N^h in Eq. (6.25) for the TE$_z$ case are truncated at $N = 3500$, respectively. To obtain results using COMSOL the infinite PEC wall with dielectric coating is truncated with a rectangular absorbing boundary. Therefore, the necessary computational domain to achieve the converged results is $15.93\lambda^2$ for the TM$_z$ case, and $30.93\lambda^2$ for the TE$_z$ case, respectively. On the other hand, the solution region in the method presented here is confined only to the area of the cavities, which is $0.56\lambda^2$ for both polarizations.

Figure 6.18 shows the calculated normalized far-field (with normalization factor of $1/(\sqrt{2\pi\rho})$), TM$_z$ case, for the two non-uniform cavities considered in the previous example (see inset of Fig. 6.16). Using the equivalence principle and introducing an equivalent electric current at the aperture of the cavities and the ground plane, the electric field in the far region can be represented as

$$\boldsymbol{E}(\boldsymbol{\rho}) = \frac{1}{j\omega\varepsilon}\left(\boldsymbol{\nabla}\times\boldsymbol{\nabla}\times\left(\int_\Gamma \boldsymbol{J}(\boldsymbol{\rho}')G(\boldsymbol{\rho},\boldsymbol{\rho}')d\Gamma'\right) - \boldsymbol{J}(\boldsymbol{\rho})\right) \tag{6.33}$$

where Γ is a contour on the infinite ground plane (see Fig.6.13). In Eq. (6.33), $\boldsymbol{J}(\boldsymbol{\rho}') = \hat{n}\times\boldsymbol{H}(\boldsymbol{\rho}')$ and $G(\boldsymbol{\rho},\boldsymbol{\rho}')$ are the induced electric current on the ground plane and the Green's function obtained as the solution to a source located inside the half-space dielectric, respectively. The Green's function is given as

$$G(\boldsymbol{\rho},\boldsymbol{\rho}') = \lim_{P\to\infty}\left(\frac{1}{P}\sum_{m=-\infty}^{\infty} e^{-jk_{x_m}|x-x'|}\frac{e^{-jk_{y_0}y}e^{-jk_{y_1}y'}}{j(k_{y_1}+k_{y_0})e^{(-j(k_{y_1}-k_{y_0})t_s)}}\right), y' < t_s < y. \tag{6.34}$$

For the TM$_z$ case where the electric field has only a z-component, the surface current $J(\boldsymbol{\rho}')$ can be written as

$$\boldsymbol{J}(\boldsymbol{\rho}') = \hat{z}\frac{1}{j\omega\mu}\frac{\partial E_z(\boldsymbol{\rho}')}{\partial n'}. \tag{6.35}$$

Therefore, Eq. (6.33) can be written as

$$\boldsymbol{E}(\boldsymbol{\rho}) = \hat{z}\int_\Gamma \frac{\partial E_z(\boldsymbol{\rho}')}{\partial n'}G(\boldsymbol{\rho},\boldsymbol{\rho}')d\Gamma'. \tag{6.36}$$

The surface current induced on the infinite ground plane is due to the incident field and the scattered field due to the aperture of the cavities. The effect of the incident field appears as a specular reflection of the ground plane in the far region. In calculating the integral in Eq. (6.36), the infinite ground plane is approximated by finite ground plane truncated at $x = \pm 5\lambda_0$. Close agreement is observed between the far-field calculations in Fig. 6.18 using TFSIE-SDGF and those obtained using COMSOL.

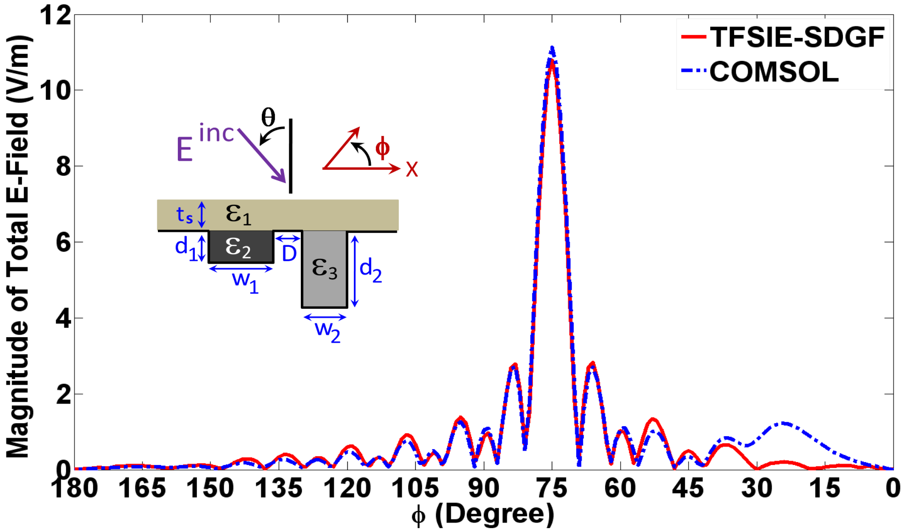

Figure 6.18: Amplitude of total E-field in the far region for two rectangular cavities with different dimensions and fillings covered with a dielectric coating, TM_z case, $\theta = 15°$. $w_1 \times d_1 = 0.6\lambda \times 0.4\lambda$, $w_2 \times d_2 = 0.4\lambda \times 0.8\lambda$, separated by $D = 0.05\lambda$, $\varepsilon_{r_1} = 1.4(1 - 0.5j)$, $\varepsilon_{r_2} = 4(1 - 0.5j)$, $\varepsilon_{r_3} = 2.1(1 - 0.5j)$, and $t_s = 0.25\lambda$.

Chapter 7

Scattering from Holes in a Conducting Surface with a Stratified Dielectric Coating

In this chapter, the method introduced in chapter 6 is extended to solve the problem of scattering from multiple holes engraved in an infinite PEC flat screen covered with a stratified dielectric coating. Using the two-boundary formulation, the unbounded region in the computational domain is divided into bounded frames containing each hole plus a thin layer above the apertures of the hole as depicted in Fig. 7.1. The finite-element formulation is used to obtain the solution of Helmholtz's equation inside the local frames. The surface integral equation employing a grounded dielectric slab Green's function (GDS-GF) is applied at each opening of the holes as a global boundary condition to determine the behavior of nodes on the local frame boundary in terms of the interior nodes.

7.1 Finite-Element Formulation of the Problem

Figure 7.1 depicts a 2-D hole having an arbitrary shape in a perfectly conductor surface covered with a homogeneous dielectric layer on both sides and illuminated by an obliquely incident plane wave. In Fig. 7.1, u^{inc}, u^{s}, and u^{trans} denote the incident field, scattered field by the aperture of the hole, and the transmitted field through the hole, respectively. Next, the problem is divided into three regions. In Fig. 7.1, region I and II denote the upper and lower half-spaces of the PEC slab including the dielectric layers, and region III represents the region inside the hole, respectively. In the region I, the thickness and permittivity of the dielectric layer are shown as t_s^I and ε_1. Also, in the region II, the thickness and permittivity of the dielectric layer are shown as t_s^{II} and ε_2. The thickness of the PEC slab

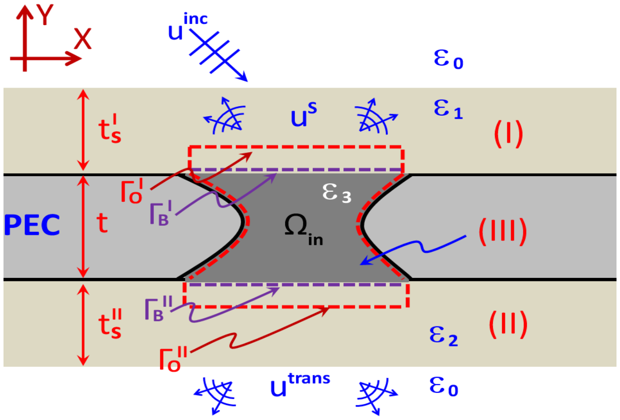

Figure 7.1: Schematic of the scattering problem from a conducting screen containing an arbitrary shape hole coated with dielectric layers.

and permittivity of the hole's filling in the region III are denoted as t and ε_3, respectively. Let Γ_B^I and Γ_B^{II} represent the contour at the interface of the hole openings with region I and II, respectively. Also let Γ_O^I and Γ_O^{II} as the exterior contour inside the dielectric layers and in close vicinity of Γ_B^I and Γ_B^{II}, respectively. Let Ω_{in} denotes the interior region of the hole, region III, including the layer between Γ_B and Γ_O in the region I and II. The finite element formulation is applied inside Ω_{in} to obtain the weak form of Helmholtz's equation,

$$\nabla \cdot \left(\frac{1}{p(x,y)} \nabla u^t \right) + q(x,y) {k_0}^2 u^t = 0 \tag{7.1}$$

where u^t is the total field. The time harmonic factor $\exp(j\omega t)$ is assumed and suppressed throughout. The functions $p(x,y)$ and $q(x,y)$ are defined as $\mu_r(x,y)$ and $\varepsilon_r(x,y)$, respectively, for the TM$_z$ polarization, or $\varepsilon_r(x,y)$and $\mu_r(x,y)$, respectively, for the TE$_z$ polarization, and k_0 is the wave-number of the wave in free space. Using the finite element formulation inside the solution domain Ω_{in} as in section 4.1, the finite element system matrix can be represented symbolically as

$$\begin{bmatrix} M_{ii} & M_{ib^I} & M_{ib^{II}} & 0 & 0 \\ M_{b^I i} & M_{b^I b^I} & 0 & M_{b^I o^I} & 0 \\ M_{b^{II} i} & 0 & M_{b^{II} b^{II}} & 0 & M_{b^{II} o^{II}} \\ 0 & M_{o^I b^I} & 0 & M_{o^I o^I} & 0 \\ 0 & 0 & M_{o^{II} b^{II}} & 0 & M_{o^{II} o^{II}} \end{bmatrix} \begin{bmatrix} u_i \\ u_{b^I} \\ u_{b^{II}} \\ u_{o^I} \\ u_{o^{II}} \end{bmatrix} = \begin{bmatrix} F_i \\ F_{b^I} \\ F_{b^{II}} \\ F_{o^I} \\ F_{o^{II}} \end{bmatrix} \tag{7.2}$$

where u_i, u_{b^I}, $u_{b^{II}}$, u_{o^I}, and $u_{o^{II}}$ represent nodal field values inside the hole, on Γ_B^I, Γ_B^{II}, Γ_O^I and on Γ_O^{II}, respectively. The $[F]$ matrix represents impressed sources at each node; therefore, $[F]$ is zero in this problem.

The linear system of equations in Eq. (7.2) represents the relationship between the nodal field values without any external constraint. In the next section, the surface integral equation will be developed as a boundary constraint to modify the system matrix equation of Eq. (7.2).

7.2 Surface Integral Equation

In this section, the surface integral equation using the grounded dielectric slab Green's function will be derived and used to express the nodal field values on Γ_O in terms of the nodal field values on Γ_B in region I and II, respectively. Figure 7.2 represents the schematic of the surface integral contour in the upper half-space Ω^I_∞ and the lower half-space Ω^{II}_∞ including the dielectric slabs. The upper half-space Ω^I_∞ and the lower half-space Ω^{II}_∞ are enclosed with the surface integral contour $\Gamma^I + \Gamma^I_\infty$, and $\Gamma^{II} + \Gamma^{II}_\infty$, respectively. In Ω^I_∞ and Ω^{II}_∞,the field vector $u(\boldsymbol{\rho})$ has only a z-component.

7.2.1 Upper Half-Space (Region I)

In the region I, the field vector $u(\boldsymbol{\rho})$ is expressed by the surface integral equation as

$$\begin{aligned} u_z(\boldsymbol{\rho}) = &- \int_{\Omega^I_\infty} g_z(\boldsymbol{\rho}') G^{e,h}_I(\boldsymbol{\rho}, \boldsymbol{\rho}') d\Omega \\ &- \oint_{\Gamma^I + \Gamma^I_\infty} \left(u_z(\boldsymbol{\rho}') \frac{\partial G^{e,h}_I(\boldsymbol{\rho}, \boldsymbol{\rho}')}{\partial n'} - G^{e,h}_I(\boldsymbol{\rho}, \boldsymbol{\rho}') \frac{\partial u_z(\boldsymbol{\rho}')}{\partial n'} \right) d\Gamma. \end{aligned} \tag{7.3}$$

In Eq. (7.3), $u_z(\boldsymbol{\rho})$ and $g_z(\boldsymbol{\rho})$ represent the electric field $E_z(\boldsymbol{\rho})$ and the electric current $J_z(\boldsymbol{\rho})$, respectively, for the TM$_z$ polarization, or the magnetic field $H_z(\boldsymbol{\rho})$ and the magnetic current $M_z(\boldsymbol{\rho})$, respectively, for the TE$_z$ polarization. Also, $G^{e,h}_I(\boldsymbol{\rho}, \boldsymbol{\rho}')$ is introduced as the grounded dielectric slab Green's function which is the solution to a current filament located at $\boldsymbol{\rho}'$ inside the dielectric layer in upper half-space. In Eq. (7.3), $G^{e,h}_I(\boldsymbol{\rho}, \boldsymbol{\rho}')$ is defined as (see section 6.2)

$$G^{e,h}_I(\boldsymbol{\rho}, \boldsymbol{\rho}') = \lim_{P \to \infty} \left(\frac{1}{P} \sum_{m=-\infty}^{\infty} e^{-jk_{x_m}|x-x'|} \tilde{G}^{e,h}_I(y, y', k_{x_m}) \right) \tag{7.4}$$

where $\tilde{G}^e_I(y, y', k_{x_m})$ is defined as

$$\tilde{G}^e_I(y, y', k_{x_m}) = \begin{cases} \frac{jk_{y_0} \sin(k_{y_1}(t^I_s - y)) + k_{y_1} \cos(k_{y_1}(t^I_s - y))}{k_{y_1}\left(jk_{y_0} \sin(k_{y_1} t^I_s) + k_{y_1} \cos(k_{y_1} t^I_s)\right)} \sin(k_{y_1} y'), & y' \leq y < t^I_s; \\ \\ \frac{e^{-jk_{y_0}(y - t^I_s)}}{\left(jk_{y_0} \sin(k_{y_1} t^I_s) + k_{y_1} \cos(k_{y_1} t^I_s)\right)} \sin(k_{y_1} y'), & y' < t^I_s \leq y \end{cases} \tag{7.5}$$

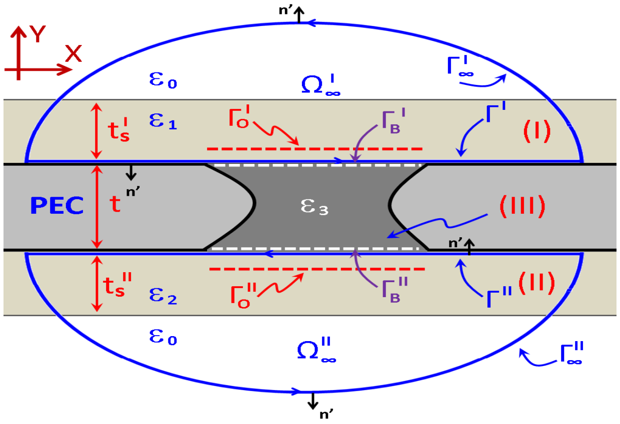

Figure 7.2: Schematic of the surface integral contour in the upper half-space and the lower half-space.

for the TM$_z$ polarization, and

$$\tilde{G}_I^h(y,y',k_{x_m}) = \begin{cases} \frac{jk_{y_0}\sin(k_{y_1}(t_s^I-y))+k_{y_1}\cos(k_{y_1}(t_s^I-y))}{k_{y_1}\left(jk_{y_0}\cos(k_{y_1}t_s^I)-k_{y_1}\sin(k_{y_1}t_s^I)\right)}\cos(k_{y_1}y'), & y' \le y < t_s^I; \\ \\ \frac{e^{-jk_{y_0}(y-t_s^I)}}{\left(jk_{y_0}\cos(k_{y_1}t_s^I)-k_{y_1}\sin(k_{y_1}t_s^I)\right)}\cos(k_{y_1}y'), & y' < t_s^I \le y \end{cases} \tag{7.6}$$

for the TE$_z$ polarization, respectively. In Eqs. (7.4)-(7.6), (x,y) and (x',y') are Cartesian components of the $\boldsymbol{\rho}$, and $\boldsymbol{\rho}'$, respectively. Also, $k_{y_0} = (k_0^2 - k_{x_m}^2)^{1/2}$ and $k_{y_1} = (k_1^2 - k_{x_m}^2)^{1/2}$ represent the Cartesian components of the propagation vector in the air and dielectric where k_{x_m} is defined by

$$k_{x_m} = k_{x_0} + \frac{2m\pi}{P}. \tag{7.7}$$

Note that the x-component of the propagation vector k_{x_m} is continuous across the air-dielectric interface. In Eq. (7.3), $u_z(\boldsymbol{\rho})$ on the left-hand side represents the total field value at any point inside the dielectric layer. Also, the first term on the right-hand side represents the excitation due to the current source $g_z(\boldsymbol{\rho}')$ in the upper half-space. In the scattering problem, this term is interpreted as the incident plane-wave and its multiple reflections by the PEC screen and the air-dielectric interface in the absence of the holes. Since both $u_z(\boldsymbol{\rho}')$ and $G_I^{e,h}(\boldsymbol{\rho},\boldsymbol{\rho}')$ satisfy the Sommerfeld radiation condition at infinity as discussed in section 6.2, the integration along Γ_∞^I in the second term of right-hand side of Eq. (7.3) vanishes (see Eq. (A.7)).

For the TM$_z$ polarization where the electric field vector is parallel to the axis of the holes, $G_I^e(\boldsymbol{\rho},\boldsymbol{\rho}')$ satisfies the Dirichlet boundary condition $G_I^e(\boldsymbol{\rho},\boldsymbol{\rho}')_{|y'=0} = 0$ (i.e.,

$G_I^e(\boldsymbol{\rho}, \boldsymbol{\rho}') = 0$ on Γ^I). Additionally, $u_z(\boldsymbol{\rho}')$ is zero on the PEC segments of the Γ^I. Consequently, Eq. (7.3) is simplified to

$$u_z(\boldsymbol{\rho}) = u_z^{excit}(\boldsymbol{\rho}) - \int_{\Gamma_B^I} u_z(\boldsymbol{\rho}') \frac{\partial G_I^e(\boldsymbol{\rho}, \boldsymbol{\rho}')}{\partial n'} d\Gamma \tag{7.8}$$

where the integration is performed at the aperture of all holes Γ_B^I. For the TE$_z$ polarization where the magnetic field vector is parallel to the axis of the holes, $G_I^h(\boldsymbol{\rho}, \boldsymbol{\rho}')$ satisfies the Neumann boundary condition $\partial G_I^h(\boldsymbol{\rho}, \boldsymbol{\rho}')/\partial n'_{|y'=0} = 0$ (i.e., $\partial G_I^h(\boldsymbol{\rho}, \boldsymbol{\rho}')/\partial y' = 0$ on Γ^I). In addition, $\partial u_z(\boldsymbol{\rho}')/\partial n'$ is zero on the PEC segments of the Γ^I. Consequently, Eq. (7.3) is simplified to

$$u_z(\boldsymbol{\rho}) = u_z^{excit}(\boldsymbol{\rho}) + \int_{\Gamma_B^I} G_I^h(\boldsymbol{\rho}, \boldsymbol{\rho}') \frac{\partial u_z(\boldsymbol{\rho}')}{\partial n'} d\Gamma. \tag{7.9}$$

The second term on the right-hand side of Eqs. (7.8)-(7.9) represents the scattered field due to the aperture of the holes. u_z^{excit} in Eq. (7.8) and Eq. (7.9) is defined by Eq. (6.10), and Eq. (6.11), respectively where t_s is replaced with t_s^I. By discretizing the aperture of the hole Γ_B^I (see sections 4.2.1 and 4.3.1), Eqs. (7.8) and (7.9) can be represented in matrix form as

$$\left[u_{o^I}\right] = \left[T^I\right] + \left[S^I\right]\left[u_{b^I}\right] \tag{7.10}$$

for the TM$_z$ polarization, and

$$\left[u_{o^I}\right] = \left\{\left[I\right] + \left[S^I\right]\right\}^{-1}\left[T^I\right] + \left\{\left[I\right] + \left[S^I\right]\right\}^{-1}\left[S^I\right]\left[u_{b^I}\right] \tag{7.11}$$

for the TE$_z$ polarization, respectively, where $[I]$ in Eq. (7.11) represents the unity matrix.

7.2.2 Lower Half-Space (Region II)

In region II, the field vector $u(\boldsymbol{\rho})$ is expressed by the surface integral equation as

$$u_z(\boldsymbol{\rho}) = -\oint_{\Gamma^{II} + \Gamma_\infty^{II}} \left(u_z(\boldsymbol{\rho}') \frac{\partial G_{II}^{e,h}(\boldsymbol{\rho}, \boldsymbol{\rho}')}{\partial n'} - G_{II}^{e,h}(\boldsymbol{\rho}, \boldsymbol{\rho}') \frac{\partial u_z(\boldsymbol{\rho}')}{\partial n'} \right) d\Gamma \tag{7.12}$$

where $u_z(\boldsymbol{\rho})$ has the same definition as in Eq. (7.3). Also, $G_{II}^{e,h}(\boldsymbol{\rho}, \boldsymbol{\rho}')$ is introduced as the grounded dielectric slab Green's function which is the solution to a current filament located at $\boldsymbol{\rho}'$ inside the dielectric layer in the lower half-space. In Eq. (7.12), $G_{II}^{e,h}(\boldsymbol{\rho}, \boldsymbol{\rho}')$ is defined as

$$G_{II}^{e,h}(\boldsymbol{\rho}, \boldsymbol{\rho}') = \lim_{P \to \infty} \left(\frac{1}{P} \sum_{m=-\infty}^{\infty} e^{-jk_{x_m}|x-x'|} \tilde{G}_{II}^{e,h}(y, y', k_{x_m}) \right) \tag{7.13}$$

where $\tilde{G}^e_{II}(y, y', k_{x_m})$ is defined as

$$\tilde{G}^e_{II}(y, y', k_{x_m}) =$$
$$\begin{cases} \frac{jk_{y_0}\sin(k_{y_2}(y+t+t_s^{II}))+k_{y_2}\cos(k_{y_2}(y+t+t_s^{II}))}{k_{y_2}\left(jk_{y_0}\sin(k_{y_2}t_s^{II})+k_{y_2}\cos(k_{y_2}t_s^{II})\right)}\sin(k_{y_2}(y'+t)), & -(t+t_s^{II}) < y \leq y'; \\ \\ \frac{e^{jk_{y_0}(y+t+t_s^{II})}}{\left(jk_{y_0}\sin(k_{y_2}t_s^{II})+k_{y_2}\cos(k_{y_2}t_s^{II})\right)}\sin(k_{y_2}(y'+t)), & y \leq -(t+t_s^{II}) < y' \end{cases} \tag{7.14}$$

for the TM$_z$ polarization, and

$$\tilde{G}^h_{II}(y, y', k_{x_m}) =$$
$$\begin{cases} \frac{jk_{y_0}\sin(k_{y_2}(y+t+t_s^{II}))+k_{y_2}\cos(k_{y_1}(y+t+t_s^{II}))}{k_{y_2}\left(jk_{y_0}\cos(k_{y_2}t_s^{II})-k_{y_2}\sin(k_{y_2}t_s^{II})\right)}\cos(k_{y_2}(y'+t)), & -(t+t_s^{II}) < y \leq y'; \\ \\ \frac{e^{jk_{y_0}(y+t+t_s^{II})}}{\left(jk_{y_0}\cos(k_{y_2}t_s^{II})-k_{y_2}\sin(k_{y_2}t_s^{II})\right)}\cos(k_{y_2}(y'+t)), & y \leq -(t+t_s^{II}) < y' \end{cases} \tag{7.15}$$

for the TE$_z$ polarization, respectively. In Eq. (7.13)-(7.15), $k_{y_0} = (k_0^2 - k_{x_m}^2)^{1/2}$ and $k_{y_2} = (k_2^2 - k_{x_m}^2)^{1/2}$ represent the Cartesian components of the propagation vector in the air and dielectric where k_{x_m} is defined by Eq. (7.7). In Eq. (7.12), $u_z(\boldsymbol{\rho})$ on the left-hand side represents the total field value at any point inside the dielectric layer. Since both $u_z(\boldsymbol{\rho}')$ and $G^{e,h}_{II}(\boldsymbol{\rho}, \boldsymbol{\rho}')$ satisfy the Sommerfeld radiation condition at infinity as discussed in section 6.2, the integration along Γ^{II}_∞ on the right-hand side of Eq. (7.12) vanishes (see Eq. (A.7)).

For the TM$_z$ polarization where the electric field vector is parallel to the axis of the holes, $G^e_{II}(\boldsymbol{\rho}, \boldsymbol{\rho}')$ satisfies the Dirichlet boundary condition $G^e_{II}(\boldsymbol{\rho}, \boldsymbol{\rho}')_{|y'=-t} = 0$ (i.e., $G^e_{II}(\boldsymbol{\rho}, \boldsymbol{\rho}') = 0$ on Γ^{II}). Additionally, $u_z(\boldsymbol{\rho}')$ is zero on the PEC segments of the Γ^{II}. Consequently, Eq. (7.12) is simplified to

$$u_z(\boldsymbol{\rho}) = -\int_{\Gamma_B^{II}} u_z(\boldsymbol{\rho}') \frac{\partial G^e_{II}(\boldsymbol{\rho}, \boldsymbol{\rho}')}{\partial n'} d\Gamma \tag{7.16}$$

where the integration is performed at the aperture of all holes Γ_B^{II}. For the TE$_z$ polarization where the magnetic field vector is parallel to the axis of the holes, $G^h_{II}(\boldsymbol{\rho}, \boldsymbol{\rho}')$ satisfies the Neumann boundary condition $\partial G^h_{II}(\boldsymbol{\rho}, \boldsymbol{\rho}')/\partial n'_{|y'=-t} = 0$ (i.e., $\partial G^h_{II}(\boldsymbol{\rho}, \boldsymbol{\rho}')/\partial y' = 0$ on Γ^{II}). In addition, $\partial u_z(\boldsymbol{\rho}')/\partial n'$ is zero on the PEC segments of the Γ^{II}. Consequently, Eq. (7.12) is simplified to

$$u_z(\boldsymbol{\rho}) = +\int_{\Gamma_B^{II}} G^h_{II}(\boldsymbol{\rho}, \boldsymbol{\rho}') \frac{\partial u_z(\boldsymbol{\rho}')}{\partial n'} d\Gamma. \tag{7.17}$$

The term on the right-hand side of Eqs. (7.16)-(7.17) represents the transmitted field through the aperture of the holes. By discretizing the aperture of the hole Γ_B^{II} (see sections 4.2.2 and 4.3.2), Eqs. (7.16) and (7.17) are represented in matrix form as

$$\left[u_{o^{II}}\right] = -\left[S^{II}\right]\left[u_{b^{II}}\right] \tag{7.18}$$

for the TM$_z$ polarization, and

$$\left[u_{o^{II}}\right] = -\left\{\left[I\right] - \left[S^{II}\right]\right\}^{-1}\left[S^{II}\right]\left[u_{b^{II}}\right] \tag{7.19}$$

for the TE$_z$ polarization, respectively, where $[I]$ in Eq. (7.19) represents the unity matrix. Combining Eq. (7.10) and Eq. (7.18) for TM$_z$ case or Eq. (7.11) and Eq. (7.19) for the TE$_z$ case with Eq. (7.2) in matrix form results in the modified system matrix as

$$\begin{bmatrix} M_{ii} & M_{ib^I} & M_{ib^{II}} \\ M_{b^I i} & M_{b^I b^I} + M_{b^I o^I} S^I & 0 \\ M_{b^{II} i} & 0 & M_{b^{II} b^{II}} - M_{b^{II} o^{II}} S^{II} \end{bmatrix} \begin{bmatrix} u_i \\ u_{b^I} \\ u_{b^{II}} \end{bmatrix} = \begin{bmatrix} F_i \\ F_{b^I} - M_{b^I o^I} T^I \\ F_{b^{II}} \end{bmatrix} \tag{7.20}$$

for the TM$_z$ case, or

$$\begin{bmatrix} M_{ii} & M_{ib^I} & M_{ib^{II}} \\ M_{b^I i} & M_{b^I b^I} + M_{b^I o^I}(I + S^I)^{-1} S^I & 0 \\ M_{b^{II} i} & 0 & -M_{b^{II} o^{II}}(I - S^{II})^{-1} S^{II} \end{bmatrix} \begin{bmatrix} u_i \\ u_{b^I} \\ u_{b^{II}} \end{bmatrix} = \begin{bmatrix} F_i \\ F_{b^I} - M_{b^I o^I}(I + S^I)^{-1} T^I \\ F_{b^{II}} \end{bmatrix} \tag{7.21}$$

for the TE$_z$ case, respectively. The solution of the modified system matrices in Eqs. (7.20)-(7.21) can be obtained using commonly used methods for solving linear systems.

7.3 Numerical Results

Once the system of equations, Eq. (7.20) for the TM$_z$ polarization or Eq. (7.21) for the TE$_z$ polarization, is derived, its solution, which gives the field values at the aperture of the holes, can be obtained using commonly used methods for solving linear systems. Notice that extending the algorithm to multiple holes is straightforward (see section 4.4). In this section, the example of the grating surface consisting of holes with side gratings is provided.

Figure 7.3 shows the schematic of a single hole with three identical rectangular side cavities engraved in an infinite PEC slab and coated with dielectric layers with thicknesses and permittivities of t_s^I and ε_1, respectively, above the PEC slab, and t_s^{II} and ε_2, respectively, below the PEC slab. The size of the hole and identical side cavities is $w \times t$ and

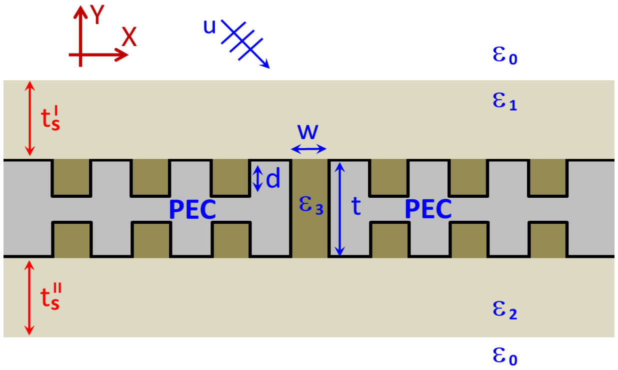

Figure 7.3: Schematic of a single hole with three identical rectangular side cavities engraved in an infinite PEC slab and coated with dielectric layers.

$w \times d$, respectively. The hole and side cavities are filled with a dielectric material having permittivity of ε_3. Also the hole and cavities are separated by w.

To validate the method presented here, comparison is made to the results obtained by COMSOL, commercial two-dimensional finite-element simulator [43]. Throughout this section, the solutions obtained using COMSOL are referred as COMSOL. To obtain the results using COMSOL the absorbing boundary condition is applied on the truncation boundaries as it is shown in Fig. 4.4. Without loss of generality, the magnitude of the incident electric field is assumed to be unity throughout this section. To implement the algorithm developed in this chapter, the nodal-based finite element formulation is used. The solution domain is discretized using first-order triangle elements with a mesh density of approximately 20 nodes per λ for the TM$_z$ case. Since there is a discontinuity in the electric field at the edges of the hole and side cavities in the TE$_z$ case, the mesh density of 100 nodes per λ is used. Throughout this section, the solution obtained using the method presented in this chapter is referred to as "Total Field Surface Integral Equation-Spatial Domain Green's Function" (TFSIE-SDGF).

Figures 7.4 and 7.5 show the total electric field for the TM$_z$ polarization and total magnetic field for the TE$_z$ polarization incident wave, respectively, at the apertures of the hole and side cavities for oblique incident plane waves. For the TM$_z$ polarization, close agreement between TFSIE-SDGF and COMSOL is observed. However in the case of COMSOL, the required computational domain is approximately $500\lambda^2$ while the TFSIE-SDGF solution domain is confined to the hole and cavities area of $2.2\lambda^2$. For the TE$_z$ polarization and in the region I, close agreement between TFSIE-SDGF and COMSOL is observed. In the region II, a deviation between the results calculated using TFSIE-SDGF and those obtained by COMSOL for the side cavities is observed. This deviation is due to the non-physical reflections from the lateral truncation boundaries that are used in COMSOL.

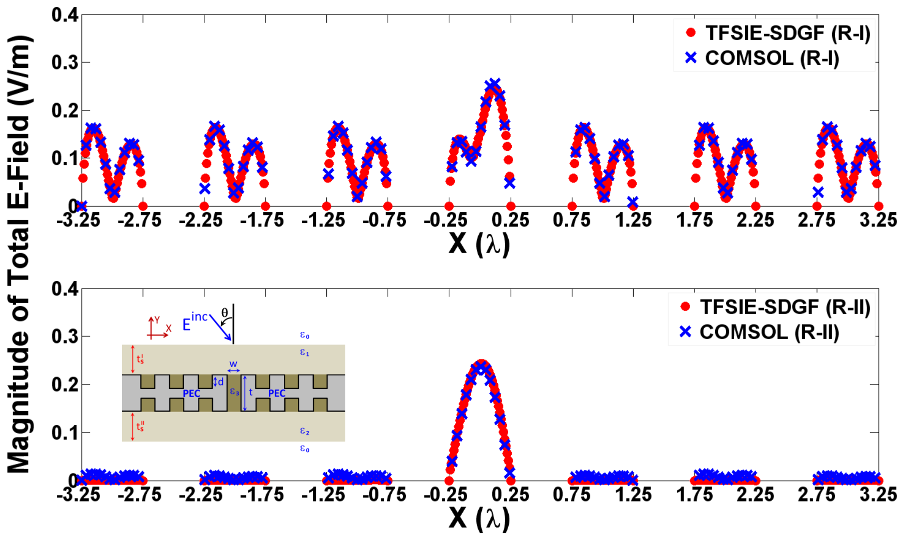

Figure 7.4: Amplitude of the total E-field at the openings into the region I (R-I) and the region II (R-II) for a single hole with three identical side cavities, TM$_z$ case, $\theta = 20°$. $w = 0.5\lambda$, $t = 0.8\lambda$, $d = 0.3\lambda$, $t_s^I = t_s^{II} = 0.3\lambda$, $\varepsilon_{r_1} = \varepsilon_{r_2} = 2.1(1 - 1j)$, $\varepsilon_{r_3} = 4$.

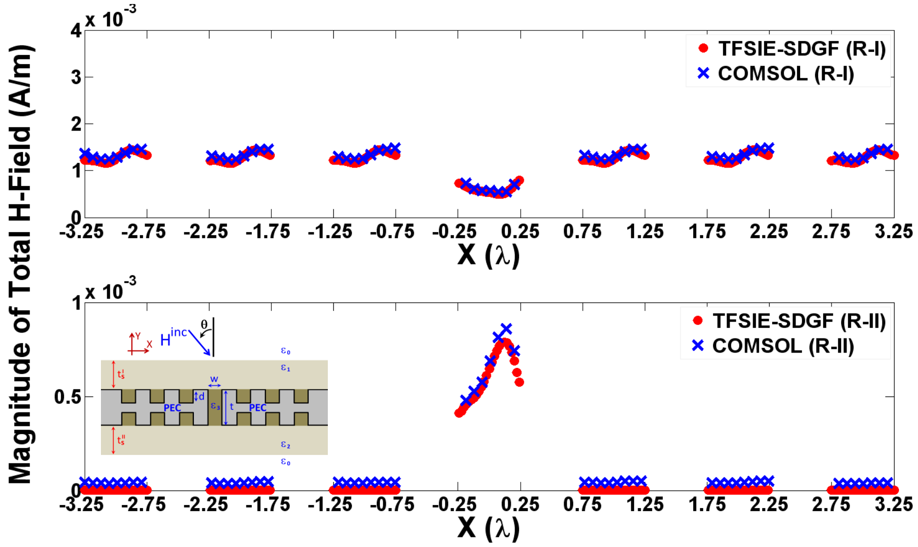

Figure 7.5: Amplitude of the total H-field at the openings into the region I (R-I) and the region II (R-II) for a single hole with three identical side cavities, TE$_z$ case, $\theta = 20°$. $w = 0.5\lambda$, $t = 0.8\lambda$, $d = 0.3\lambda$, $t_s^I = t_s^{II} = 0.3\lambda$, $\varepsilon_{r_1} = \varepsilon_{r_2} = 4(1 - 1j)$, $\varepsilon_{r_3} = 10$.

Chapter 8

Conclusion and Future Work

8.1 Contributions

In this thesis, a novel computational algorithm based on hybrid finite element - boundary integral method for scattering problem from two-dimensional gratings is developed. In the algorithm presented in this work, the solution region is divided into an interior region containing the finite number of cavities or holes engraved in the conducting screen and the region exterior to them. The finite element formulation is applied inside the interior regions to derive a linear system of equations associated with field unknowns. Using two-boundary formulation, the surface integral equation employing the free-space Green's function is then applied *only* at the openings of the cavities or holes as a boundary constraint to connect the field unknowns at the boundaries to the interior field unknowns.

The hybrid FE-BIM algorithm is extended to grating surfaces containing infinite number of cavities or holes by deriving the quasi-periodic Green's function. The infinite array of cavities or holes is divided into unit-cells. The finite element formulation is then applied inside the cavities or holes in the unit-cell. The surface integral equation as a global boundary condition employing the quasi-periodic Green's function is used to truncate the solution region to the cavities or holes to *only* one unit-cell, resulting in a highly efficient solution procedure. In this formulation, no singularities in the quasi-periodic Green's function arise while applying the surface integral as a boundary constraint.

Finally, the algorithm is extended to solve the problem of scattering from finite or infinite array of two-dimensional cavities or holes engraved in a metallic screen and covered with stratified dielectric coating. Similar to the metallic grating surfaces, the finite element formulation is applied *only* inside the cavities or holes. The surface integral equation employing the grounded dielectric slab Green's function GDS-GF in spatial domain is formulated to derive the boundary constraint on the field unknowns at the opening of the cavities or holes. The spatial domain GDS-GF is expressed in terms of a Fourier transform type integral that includes finite number of surface wave poles and infinite number of leaky wave poles. To transform the GDS-GF to a form that can be computed and thus useful for the implementation of the surface integral equation, the quasi-periodic Green's function in spatial domain which is the solution to an infinite periodic array of the unit sources is first derived using Floquet theorem. The quasi-periodic Green's function is then expressed in terms of an infinite series of Fourier type integrals. Next, the quasi-periodic Green's function is transformed into discrete form using Poisson's sum formula; therefore, eliminating the need to calculate Fourier integrals in the Green's function series. Finally, the spatial domain Green's function which is the solution to a single unit source is calculated by assuming the unit sources placed infinitely apart.

The method presented in this thesis is applicable to the scattering problem from cavities or holes with arbitrary shapes, sizes, and fillings. Also the algorithm presented here is applicable to the scattering problems from grating surfaces covered with materials having arbitrary permittivity and permeability having strong relevance to plasmonics problems. Furthermore, no singularities in the Green's function arise while applying the surface integral as a boundary constraint. The formulation is based on the total field and is applicable to both TM and TE polarizations. The run-time and solution efficiency of the technique developed in this thesis are two major attractive features making it well suited for optimization problems involving gratings and holes.

In summary, the following contributions were achieved in this thesis:

1. **Developed** a new FEM-based method to solve the problem of scattering from a single cavity with arbitrary shape and filling engraved in an infinite perfect electric conducting (PEC) screen for TM and TE polarization. The method is based on the total field formulation and using the surface integral equation and the free-space Green's function as a boundary constraint. This work was published in [63].

2. **Extended** the method developed in 1 to the problem of scattering from multiple cavities with arbitrary shape and spacing. **Described** the coupling between the cavities mathematically using the surface integral equation and the Green's function, and **analyzed** the physical mechanism of the coupling between the cavities. This work was reported in [63].

3. **Extended** the method developed in 1 to the problem of scattering from single and multiple holes with arbitrary shape and spacing engraved in a perfectly conducting slab by applying the surface integral equation and the Green's function as a boundary constraint at both openings of the holes. This work was published in [64].

4. **Extended** the method developed in 1 to the problem of scattering from infinite array of cavities with arbitrary shape, filling, and spacing engraved in the perfectly

conducting slab by applying the surface integral equation and the quasi-periodic Green's function as a boundary constraint. This work was published in [65].

5. **Extended** the method developed in 1 to the problem of scattering from finite and infinite array of cavities with arbitrary shape, filling, and spacing engraved in a perfectly conducting slab covered with stratified dielectric coating by using the surface integral equation and the grounded dielectric slab Green's function as a boundary constraint. This work was published in [66].
6. **Developed** an algorithm to express the spatial domain grounded dielectric slab Green's function in series form. **Analyzed** the convergence behavior of the grounded dielectric slab Green's function series versus different parameters such as lateral distance between the source point and the field point, the thickness of the dielectric slab, and the loss tangent of the dielectric coating. This work was reported in [66].
7. **Extended** the method developed in 6 and 3 to the problem of scattering from a grating structure containing array of holes with side cavities with arbitrary shape, filling, and spacing engraved in a perfectly conducting slab covered with stratified dielectric coating.
8. **Presented and validated** several numerical examples for single and multiple cavities and holes with different shapes and fillings with or without dielectric coating.

9. **Compared** the efficiency of the new boundary integral method introduced in this work with absorbing boundary condition and perfectly matched layer used by generic full wave field solvers for modeling the scattering problem from grating surfaces. **Analyzed** the versatility of the present method in modeling of the scattering from grating surfaces due to the grazing incidents. This work was published in [67].

8.2 Future Directions

Following are some possible direction for the further research work:

1. **Extending** the algorithm presented in this thesis to the problem of scattering from three dimensional (3-D) gratings. The extension the method to the 3-D structure provides highly accurate and efficient solution to optimization problems associated with electromagnetic band-gap structures and frequency selective surfaces.

2. **Investigating** the scattering problem from grating structures covered with the nobel metals such as silver or gold in order to study engineering application of extraordinary transmission of light and plasmonic resonances. The interesting feature of such noble metals is that over the optical frequency regime, the metals exhibit negative permittivity. Possible modification in the Green's function due to the negative permittivity of the coating may be needed. Also convergence of the Green's function series for a coating with negative permittivity potentially is challenging.

3. **Generalizing** the algorithm to the class of eigenvalue problems associated with photonics applications such as dispersion studies in photonic crystals.

APPENDICES

Appendix A

Boundary Integral Formulation

In this section, the boundary integral formulation for two-dimensional interior problem will be derived. Figure A.1 depicts a region Ω including current filament g. Region Ω is enclosed by a boundary Γ. In Fig. A.1, u_z and g represent electric field, and electric current, respectively for the TM$_z$ polarization, or magnetic field, and magnetic current,respectively for the TE$_z$ polarization. The field vector u_z is governed by Helmholtz's equation:

$$\nabla^2 u_z(\boldsymbol{\rho}) + {k_0}^2 u_z(\boldsymbol{\rho}) = j\omega p(\boldsymbol{\rho}) g_z(\boldsymbol{\rho}), \qquad \boldsymbol{\rho} \in \Omega. \tag{A.1}$$

where $p(\boldsymbol{\rho})$ is defined as $\mu_r(\boldsymbol{\rho})$ for the TM$_z$ polarization, or $\varepsilon_r(\boldsymbol{\rho})$ for the TE$_z$ polarization, respectively. By introducing the Green's function $G(\boldsymbol{\rho}, \boldsymbol{\rho}')$ which is the field observed at $\boldsymbol{\rho}$ due to a current filament located at $\boldsymbol{\rho}'$, satisfying the boundary condition in Ω, and governed by Helmholtz's equation

$$\nabla^2 G(\boldsymbol{\rho}, \boldsymbol{\rho}') + {k_0}^2 G(\boldsymbol{\rho}, \boldsymbol{\rho}') = -\delta(\boldsymbol{\rho} - \boldsymbol{\rho}') \qquad \boldsymbol{\rho}, \boldsymbol{\rho}' \in \Omega. \tag{A.2}$$

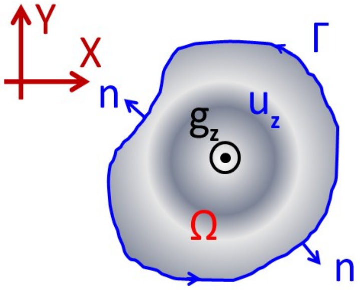

Figure A.1: Schematic of surface integral contour around an arbitrary closed volume.

Multiplying both sides of Eq. (A.1) by $G(\boldsymbol{\rho}, \boldsymbol{\rho}')$ and integrating over Ω yields

$$\int_{\Omega} G(\boldsymbol{\rho}, \boldsymbol{\rho}') \left(\nabla^2 u_z(\boldsymbol{\rho}) + {k_0}^2 u_z(\boldsymbol{\rho})\right) d\Omega = j\omega \int_{\Omega} p(\boldsymbol{\rho}) g_z(\boldsymbol{\rho}) G(\boldsymbol{\rho}, \boldsymbol{\rho}') d\Omega. \tag{A.3}$$

invoking the Green's second identity

$$\int_{\Omega} \left(u_z \nabla^2 G - G \nabla^2 u_z\right) d\Omega = \oint_{\Gamma} \left(u_z \frac{\partial G}{\partial n} - G \frac{\partial u_z}{\partial n}\right) d\Gamma \tag{A.4}$$

where Γ is the contour enclosing Ω, Eq. (A.3) can be written as

$$\int_{\Omega} u_z(\boldsymbol{\rho}) \left(\nabla^2 G + {k_0}^2 G\right) d\Omega = j\omega \int_{\Omega} p(\boldsymbol{\rho}) g_z(\boldsymbol{\rho}) G d\Omega + \oint_{\Gamma} \left(u_z \frac{\partial G}{\partial n} - G \frac{\partial u_z}{\partial n}\right) d\Gamma. \tag{A.5}$$

Substituting Eq. (A.2) in Eq. (A.5), and interchanging primed and unprimed coordinates

$$u_z(\boldsymbol{\rho}) = -j\omega \int_{\Omega} p(\boldsymbol{\rho}') g_z(\boldsymbol{\rho}') G(\boldsymbol{\rho}, \boldsymbol{\rho}') d\Omega - \oint_{\Gamma} \left(u_z(\boldsymbol{\rho}') \frac{\partial}{\partial n'} G(\boldsymbol{\rho}, \boldsymbol{\rho}') - G(\boldsymbol{\rho}, \boldsymbol{\rho}') \frac{\partial}{\partial n'} u_z(\boldsymbol{\rho}')\right) d\Gamma. \tag{A.6}$$

Equation (A.6), represents the boundary integral formulation for the two-dimensional region including sources.

For cylindrical waves satisfying Sommerfeld radiation condition [42], the second term of Eq. (A.6) vanishes as the boundaries are placed at infinity (i.e., $\Gamma \to \infty$)

$$\lim_{\Gamma \to \infty} \oint_{\Gamma} \left(u_z \frac{\partial G}{\partial n'} - G \frac{\partial u_z}{\partial n'}\right) d\Gamma = \lim_{\Gamma \to \infty} \oint_{\Gamma} \left(u_z(-jkG) - G(-jku_z)\right) d\Gamma = 0. \tag{A.7}$$

Therefore Eq. (A.6) can be simplified for the far region as

$$u_z(\boldsymbol{\rho}) = -j\omega \int_{\Omega} p(\boldsymbol{\rho}') g_z(\boldsymbol{\rho}') G(\boldsymbol{\rho}, \boldsymbol{\rho}') d\Omega. \tag{A.8}$$

Bibliography

[1] H. Raether. *Surface Plasmons on Smooth and Rough Surfaces and on Gratings.* Springer, NewYork NY, 1998. 1

[2] T. W. Ebbesen H. J. Lezec H. F. Ghaemi T. Thio and P. A. Wolff. Extraordinary optical transmission through sub-wavelength hole arrays. *Nature*, 391:667–669, February 1998. 1

[3] H. J. Lezec A. Degiron E. Devaux R. A. Linke L. Martin-Moreno F. J. Garcia-Vidal and T. W. Ebbesen. Beaming light from a subwavelength aperture. *Science*, 297:820–823, August 2002. 1

[4] A. Krishnan T. Thio T. J. Kim H. J. Lezec T. W. ebbesen P. A. Wolff J. Pendry L. Martin-Moreno and F. J. Garcia-Vidal. Evanescently coupled resonance in surface plasmon enhanced transmission. *Optics Communication*, 200:1–7, December 2001. 1

[5] S. Kawata. Near-field microscope probes utilizing surface plasmon polaritons. *Appl. Phys.*, 81:15–27, 2001. 1

[6] F. Wei and Z. Liu. Plasmonic structured illumination microscopy. *Nano Letters*, 10:2531–2536, July 2010. 1

[7] H. Hu C. Ma and Z. Liu. Plasmonic dark field microscopy. *Appl. Phys.*, 96:113107–1–3, March 2010. 1

[8] A. Sentenac K. Belkebir H. Giovannini and P. C. Chaumet. Subdiffraction resolution in total internal reflection fluorescence microscopy with a grating substrate. *Optics Letters*, 33:255–257, February 2008. 1

[9] X. Luo and T. Ishihara. Surface plasmon resonant interference nanolithography technique. *Appl. Phys. Letter*, 84:4780–4782, June 2004. 1

[10] X. Luo and T. Ishihara. Subwavelength photolithography based on surface-plasmon polariton resonance. *Optics Express*, 12:3055–3065, July 2004. 1

[11] Y. Ngu M. Peckerar M. Dagenais J. Barry and B. Dutt. Lithography plasmonics and subwavelength aperture exposure technology. *J. Vac. Sci. Tech. B*, 25:2471–2475, November 2007. 1

[12] Y. Xiong Zh. Liu and X. Zhang. Projecting deep-subwavelength patterns from diffraction-limited masks using metal-dielectric multilayers. *Appl. Phys.*, 93:111116–1–3, September 2008. 1

[13] Y. Yoon H. Lee S. Lee S. H. Kim J. Park and K. Lee. Color filter incorporating a subwavelength patterned grating in poly silicon. *Optics Express*, 16:2374–2380, February 2008. 1

[14] K. R. Catchpole and S. Pillai. Surface plasmon for enhanced silicon light-emitting diods and solar cells. *Journal of Luminescence*, 121:315–318, September 2006. 1

[15] A. K. Pradhan R. B. Konda H. Mustafa R. Mundle O. Bamiduro U. N. Roy Y. Cui and A. Burger. Surface plasmon resonance in cdse semiconductor coated with gold nanoparticles. *Optics Express*, 16:6202–6208, April 2008. 1

[16] S. Pillai K. R. Catchpole T. Trupke and M. A. Green. Surface plasmon enhanced silicon solar cells. *Journal of Applied Physics*, 101:093105–1–8, May 2007. 1

[17] R. F. Harrington and J. R. Mautz. A generalized network formulation for aperture problems. *IEEE Trans. Antenna Propag.*, 24:870–873, November 1976. 2, 4

[18] D. T. Auckland and R. F. Harrington. Electromagnetic transmission through a filled slit in a conducting plane of finite thickness TE case. *IEEE Trans. Microwave Theory Tech.*, 26:499–505, July 1978. 2, 4

[19] K. Barkeshli and J. L. Volakis. TE scattering by a two-dimensional groove in a ground plane using higher order boundary conditions. *IEEE Trans. Antenna Propag.*, 38:1421–1428, September 1990. 2, 4

[20] K. Barkeshli and J. L. Volakis. Scattering from narrow rectangular filled grooves. *IEEE Trans. Antenna Propag.*, 39:804–810, June 1991. 2, 4

[21] Y. Shifman and Y. Leviatan. Scattering by a groove in a conducting plane a PO-MoM hybrid formulation and wavelet analysis. *IEEE Trans. Antenna Propag.*, 49:1807–1811, December 2001. 2

[22] Y.-L Kok. Boundary-value solution to electromagnetic scattering by a rectangular groove in a ground plane. *J. Opt. Soc. Am. A*, 9:302–311, February 1992. 2, 4

[23] T. J. Park H. J. Eom and K. Yoshitomi. An analytic solution for transverse-magnetic scattering from a rectangular channel in a conducting plane. *J. Opt. Soc. Am. A*, 73:3571–3573, April 1993. 2, 4

[24] T. J. Park H. J. Eom and K. Yoshitomi. An analysis of transverse electric scattering from a rectangular channel in a conducting plane. *Radio Science*, 28:663–673, September 1993. 2, 4

[25] T. J. Park H. J. Eom and K. Yoshitomi. Analysis of TM scattering from finite rectangular grooves in a conducting plane. *J. Opt. Soc. Am. A*, 10:905–911, May 1993. 2, 4, 27, 29

[26] R. A. Depine and D. C. Skigin. Scattering from metallic surfaces having a finite number of rectangular grooves. *J. Opt. Soc. Am. A*, 11:2844–2850, November 1994. 2, 4, 6, 67

[27] S. H. Kang H. J. Eom and T. J. Park. TM-scattering from a slit in a thick conducting screen: Revisited. *IEEE Trans. Microwave Theory Tech.*, 41:895–899, June 1993. 2, 4

[28] T. J. Park S. H. Kang and H. J. Eom. TE scattering from a slit in a thick conducting screen: Revisited. *IEEE Trans. Antenna Propag.*, 42:112–114, August 1994. 2, 4

[29] H. J. Eom. *Electromagnetic Wave Theory for Boundary-Value Problems.* Springer, NewYork NY, 2004. 2, 4

[30] M. A. Basha S. K. Chaudhuri S. Safavi-Naeini and H. J. Eom. Rigorous formulation for electromagnetic plane-wave scattering from a general-shaped groove in a perfectly conducting plane. *J. Opt. Soc. Am. A*, 24:1647–1655, June 2007. 2, 4, 5, 18, 19

[31] M. A. Basha S. K. Chaudhuri and S. Safavi-Naeini. Electromagnetic scattering from multiple arbitrary shape grooves: A generalized formulation. *Microwave Symposium*, 24:1935–1938, June 2007. 2, 5, 18, 22

[32] B. H. McDonald and A. Wexler. Finite-element solution of unbounded field problems. *IEEE Trans. Microwave Theory Tech.*, 20:841–847, December 1972. 3, 5, 8, 26

[33] O. M. Ramahi and R. Mittra. Finite element solution for a class of unbounded geometries. *IEEE Trans. Antenna Propag.*, 39:244–250, February 1991. 3, 4, 5, 8

[34] J. M. Jin and J. L. Volakis. TM scattering by an inhomogeneously filled aperture in a thick conducting plane. *Microwaves Antennas and Propagation IEE Proceedings H*, 137:153–159, June 1990. 3, 5

[35] J. M. Jin and J. L. Volakis. TE scattering by an inhomogeneously filled thick conducting plane. *IEEE Trans. Antenna Propag.*, 38:1280–1286, August 1990. 3, 5

[36] J. M. Jin. *The Finite Element Method in Electromagnetics.* Jon Wiley & Sons Inc., NewYork NY, 1993. 5, 12, 13, 14, 15

[37] S. D. Gedney and R. Mittra. Analysis of the electromagnetic scattering by thick gratings using a combined FEM/MM solution. *IEEE Trans. Antenna Propag.*, 39:1605–1614, November 1991. 5

[38] T. Delort and D. Maystre. Finite-element method for gratings. *J. Opt. Soc. Am. A*, 10:2592–2601, December 1993. 5

[39] G. Pelosi A. Freni and R. Coccioli. Hybrid technique for analyzing scattering from periodic structures. *in IEE Proceedings-H of Microwaves Antennas and Propagation*, 140:65–70, April 1993. 5

[40] Y. A. Baranchugov P. M. Zatsepin and S. A. Komarov. Electromagnetic wave scattering from an infinity array of rectangular cavities in an impedance screen. *in proceedings of IEEE Region 8 International Conference on Computational Technologies in Electrical and Electronics Engineering*, pages 347–349, July 2008. 6

[41] Y. H. Cho. Transverse magnetic plane-wave scattering equations for infinite and semi-infinite rectangular grooves in a conducting plane. *IET Microw. Antennas Propag.*, 2:704–710, March 2008. 6

[42] L. B. Felson and N. Marcuvitz. *Radiation and Scattering of Waves.* IEEE Press, New Jersey NJ, 1973. 11, 106

[43] COMSOL Version 3.5. COMSOL MULTIPHYSICS. *http://www.comsol.com.* 18, 46, 85, 98

[44] B. Engquist and A. Majda. Absorbing boundary condition for numerical simulation of waves. *Mathematics for Computation*, 31:629–651, 1977. 26

[45] A. Bayliss M. Gunzburger and E. Turkel. Boundary condition for the numerical solution of elliptic equations in exteior regions. *SIAM Appl. Math.*, 42:430–450, April 1982. 26

[46] O. Ramahi A. Khebir and R. Mittra. Numerically derived absorbing boundary condition for the solution of open region scattering problems. *IEEE Trans. Antenna Propag.*, 39:350–353, March 1991. 26

[47] O. M. Ramahi. The concurrent complementary operators method for FDTD mesh truncation. *IEEE Trans. Antenna Propag.*, 46:1475–1482, October 1998. 28

[48] J-P Berenger. Numerical reflection from FDTD-PMLs: A comparison of the split PML with the unsplit and CFSPMLs. *IEEE Trans. Antenna Propag.*, 50:258–265, March 2002. 28

[49] Ansoft HFSS Version 10.1. Ansoft Corporation. *http://www.ansoft.com.* 28

[50] I. Bardi and Z. Cendes. New directions in HFSS for designing microwave devices. *Microwave Journal.*, 41:22–, August 1998. 29

[51] R. Mittra O. Ramahi A. Khebir R. Gordon and A. Kouki. A review of absorbing boundary condition for two and three-dimensional electromagnetic scattering problem. *IEEE Trans. Magnetics*, 25:3034–3039, July 1989. 53

[52] A. Parsa and R. Paknys. Interior Green's function solution for a thick and finite dielectric slab. *IEEE Trans. Antenna Propag.*, 55:3504–3514, December 2007. 69, 70, 75

[53] K. A. Michalski and D. Zheng. Electromagnetic scattering and radiation by surfaces of arbitrary shape in layerd media, part i:, theory. *IEEE Trans. Antenna Propag.*, 38:335–344, March 1990. 70

[54] M. I. Aksun. A robust approach for the derivation of closed-form Green's functions. *IEEE Trans. Microwave Theory Tech.*, 44:651–658, May 1996. 70

[55] G. Dural and M. I. Aksun. Closed form Green's function for general sources and stratified media. *IEEE Trans. Microwave Theory Tech.*, 43:1545–1552, July 1995. 70

[56] M. I. Aksun F. Caliskan and L. Gurel. An efficient method for electromagnetic characterization of 2-D geometries in stratified media. *IEEE Trans. Microwave Theory Tech.*, 50:1264–1274, May 2002. 70

[57] M. I. Aksun and G. Dural. Clarification of issues on the closed-form Green's functions in stratified media. *IEEE Trans. Antenna Propag.*, 53:3644–3653, November 2005. 70

[58] R. R. Biox F. Mesa and F. Medina. Application of total least squares to the derivation of closed-form Green's functions for planar layered media. *IEEE Trans. Microwave Theory Tech.*, 55:268–280, February 2007. 70

[59] F. Mesa R. R. Biox and F. Medina. Closed-form expressions of multilayered planar Green's functions that account for the continuous spectrum in the far field. *IEEE Trans. Microwave Theory Tech.*, 56:1601–1614, July 2008. 70

[60] A. Alparslan M. I. Aksun and K. A. Michalski. Closed-form Green's functions in planar layered media for all ranges and materials. *IEEE Trans. Microwave Theory Tech.*, 58:602–613, March 2010. 70

[61] R. R. Biox A. L. Fructos and F. Medina. Closed-form uniform asymptotic expansions of Green's functions in layered media. *IEEE Trans. Microwave Theory Tech.*, 58:2934–2945, September 2010. 70

[62] D. M. Pozar and D. H. Schaubert. Scan blindness in infinite phased arrays of printed dipoles. *IEEE Trans. Antenna Propag.*, 32:602–610, June 1984. 77

[63] B. Alavikia and O. M. Ramahi. Finite-element solution of the problem of scattering from cavities in metallic screens using the surface integral equation as a boundary constraint. *J. Opt. Soc. Am. A*, 26:1915–1925, September 2009. 101

[64] B. Alavikia and O. M. Ramahi. Electromagnetic scattering from multiple subwavelength apertures in metallic screens using the surface integral equation method. *J. Opt. Soc. Am. A*, 27:815–826, April 2010. 101

[65] B. Alavikia and O. M. Ramahi. An efficient method using finite-elements and the surface integral equation to solve the problem of scattering from infinite periodic conducting grating. *Radio Science*, 46:RS1001–1–10, 2011. 102

[66] B. Alavikia and O. M. Ramahi. Hybrid finite element - boundary integral algorithm to solve the problem of scattering from finite and infinite array of cavities with stratified dielectric coating. *J. Opt. Soc. Am. A*, 28:1022–1031, June 2011. 102

[67] B. Alavikia and O. M. Ramahi. Fundamental limitations on the use of open-region boundary conditions and matched layers to solve the problem of gratings in metallic screens. *ACES Journal*, 25:652–658, August 2010. 102